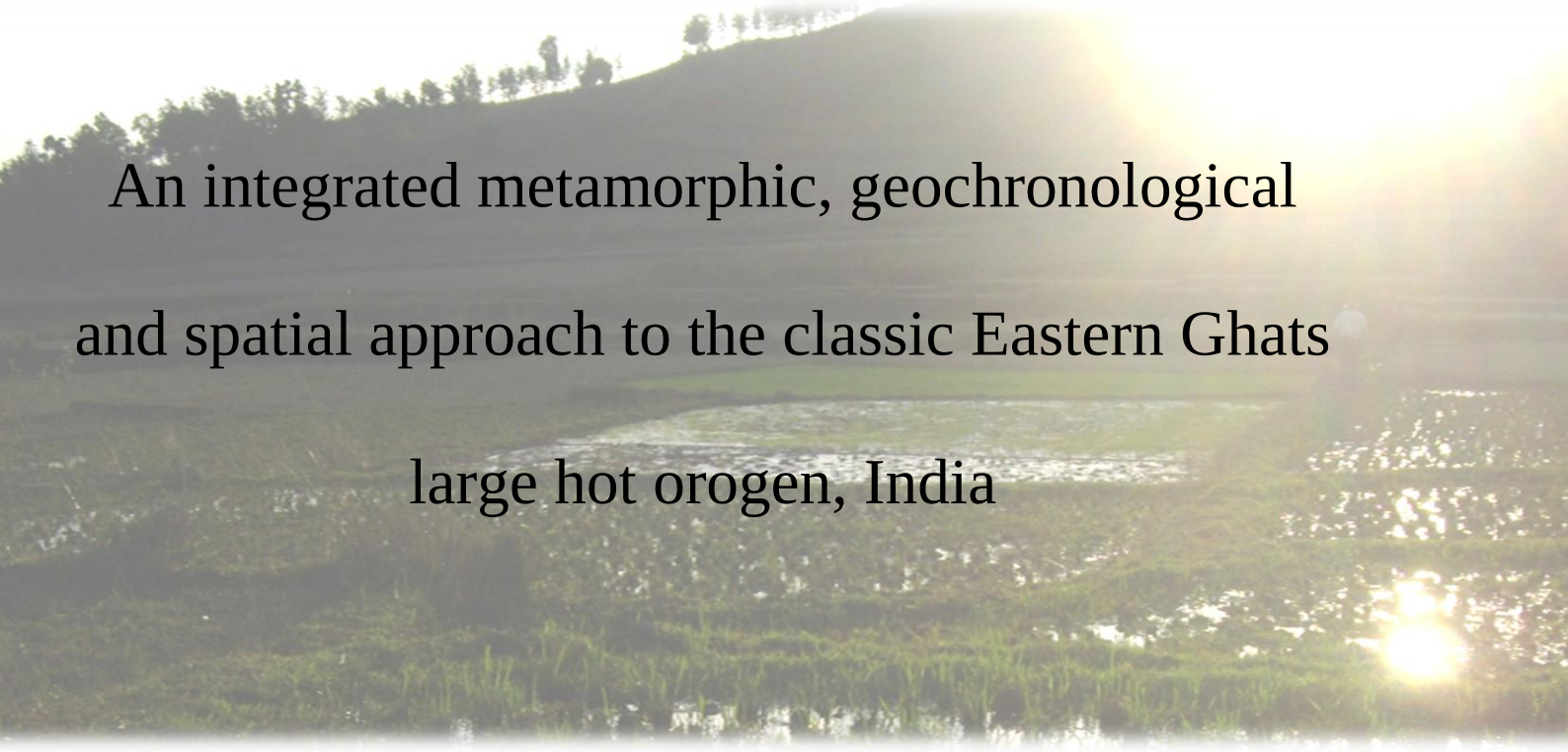

An integrated metamorphic, geochronological and spatial approach to the classic Eastern Ghats large hot orogen, India

Sarah K. Marshall

Continental Evolution Research Group
Department of Geology and Geophysics
School of Earth and Environmental Sciences
University of Adelaide, South Australia
sarah.k.marshall@student.adelaide.edu.au

TABLE OF CONTENTS

Abstract 2
Introduction 3
Geological Framework and scope for study 4
Field observations and structure 8
Sampling and metamorphic petrology 9
Methodologies 14
Whole rock and elemental chemistry 14
Quantified metamorphic analysis 15
LA-ICPMS and SHRIMP U-Th-Pb Geochronology 15
Sample Preparation 16
SHRIMP operating procedures and data reduction 16
LA-ICPMS operating procedures and data reduction 16
Garnet cooling rate estimates 17
Results 18
Mineral Chemistry 18
Garnet 18
Orthopyroxene 19
Sapphirine 19
Cordierite 19
Alkali feldspar 19
Biotite/Phlogopite 20
Spinel 20
Magnetite 21
Corundum 21
Ilmenite 21
Sillimanite 21
Phase diagram analysis 21
GEOCHRONOLOGY 24
Conventional Thermobarometry and diffusion-based modelling cooling rates 28
Discussion 29
Interpretation of geochronology 29
Interpretation of P-T evolution 34
Duration of thermal event 37
Potential causative mechanisms leading to the development of a large hot orogen 40
Conclusions 42
Acknowledgements 43
reference list 43
Figure Captions 47
Tables 54
Figures 73

ABSTRACT

The Eastern Ghats granulite terrain experienced one ultrahigh-temperature (UHT) metamorphic event, slow cooling, and a Pan African thermal overprint. The style of metamorphism preserved in the Eastern Ghats depends on its location across the belt, rock type and structural setting. *P-T* pseudosections have been combined with *in situ* U-Pb monazite geochronology to produce *P-T-t* paths from various localities across the high-grade metamorphic belt to clarify the existence of one metamorphic event at *ca.* 975 – 930 Ma The metamorphic episode is characterised by ultrahigh-temperature metamorphism with peak temperatures of 880 – 1050 °C and peak pressures of 8 – 12 kbar followed by either near-isothermal decompression or isobaric cooling, depending on the sample location across the belt.

In situ SHRIMP and LA-ICPMS U-Th-Pb monazite gechronology is used to constrain the contrasting metamorphic evolutions. Detailed analysis of both monazite compositional mapping and textural location of monazite grains within samples reveal that there is a spatial trend in ages to partner the variation in *P-T* paths. At *ca.* 975 Ma, metamorphism is found to be older in the east where samples are confined within a steep, upright fabric that contains structural evidence for two deformational events. In the west of the belt, the foliation is flat, and leucosomes confined sharply between compositional foliations, as in the east. Metamorphism in the west occurred at *ca.* 930 Ma.

To provide inferences about the duration of metamorphis coupled-phase diffusional modelling is applied to various samples across the belt. Results reveal that the Eastern Ghats experienced very slow cooling, with rates of 0.8 – 5 °C/My over potentially as long as 300 million years. The prolonged, extreme thermal conditions experienced by mid- to lower- crustal granulites in the Eastern Ghats leads to a comparison of this metamorphic terrane with the concept of a large hot orogen. The source of heat and tectonic settings of ultrahigh temperature metamorphism still remain contentious; however robust *P-T-t* paths such as those produced in this study are considered a primary component to understand UHT metamorphism and large hot orogens using thermo-mechanical models.

INTRODUCTION

Large, hot, Precambrian orogens are high-temperature metamorphic belts that have experienced long-duration deformation. High temperatures are maintained for extended (commonly > 80 Myr) periods coeval with repeated magmatism (Chardon *et al.* 2009). Tectonic processes that contribute to large hot orogen development are difficult to assess from structural data due incipient viscosity of the orogenic crust (Fritz *et al.* 2009), as large hot orogens are defined by lateral gravity-controlled crustal flow (Beaumont *et al.* 2006). Instead, thermo-mechanical models provide the analytical tools to better define the development and exhumation of large hot orogens (e.g. Batt & Braun 1999; Jamieson *et al.* 2004; Beaumont *et al.* 2006). To interpret thermo-mechanical models, the use of accurate *P-T-t* paths is paramount (Jamieson *et al.* 2004). In particular, accurate quantitative *P-T* and *P-T-t* paths for ultrahigh-temperature terranes is of great importance as many numerical models of collisional orogenesis are currently unable to account for thermally extreme metamorphism (Harley 2008). Ultrahigh-temperature (UHT) metamorphism is defined at temperatures in excess of *ca.* 900°C, potentially as high as 1150°C (Harley 2008), with its upper limit constrained by the liquidus for crustal rocks (Brown 2007). Many key challenges exist in understanding ultrahigh-temperature metamorphism. Current areas requiring more research include the tectonic setting(s) of UHT metamorphism, the time-scales over which UHT metamorphism occurs and the P-T paths followed by UHT terranes (Kelsey 2008).

The Eastern Ghats, India is an areally extensive Meso- to Neoproterozoic granulite facies terrain that has experienced ultrahigh-temperature metamorphism with temperatures as high as 1100 °C and pressures as high as 12 kbar. It has been the subject of numerous studies investigating the thermal and physical conditions of metamorphism (e.g. Sengupta *et al.* 1990; Dasgupta *et al.* 1991; Bhowmik *et al.* 1995; Sen *et al.* 1995; Gupta *et al.* 2000; Bhattacharya & Gupta 2001; Bhattacharya & Kar 2002; Dobmeier & Raith 2003), however there is a lack of consistency between metamorphic studies (Fig. 3). A spread of ages from ~ 1.5 Ga – 520 Ma (Fig. 4) is used as evidence for a polymetamorphic evolution in the Eastern Ghats, consisting of discrete metamorphic episodes (Mukhopadhyay & Basak 2009). The tectonic significance of

Eastern Ghats metamorphism still remains elusive and whether metamorphism occurred as a single, long duration event or multiple events is disputed.

Current understanding of the terrain relies on metamorphic and geochronological studies that are detached from one another. In order to more completely understand the Eastern Ghats terrain and the mechanisms responsible for ultrahigh-temperature metamorphism it is critical to investigate the integrated pressure-temperature-time evolution of individual rocks from numerous localities across the belt. Without integrated time-space information, misleading interpretations could be made regarding the geodynamics of the Eastern Ghats. The primary aim of this study is to build on existing metamorphic and geochronological studies by investigating the age-constrained thermal and physical conditions of metamorphism from numerous localities through the Eastern Ghats. Specifically, *in situ* U-Pb monazite geochronology will be integrated with calculated metamorphic phase equilibria and diffusion-based cooling information. Secondarily the outcomes of this study enhance the understanding of the Eastern Ghats metamorphic evolution for the purpose of providing constraints for further studies utilising thermo-tectonic models, which can shed light on continental-scale orogenesis (Harley 2008).

GEOLOGICAL FRAMEWORK AND SCOPE FOR STUDY

The Eastern Ghats Belt is a Meso- to Neo-proterozoic granulite terrane comprising granulite-facies meta sedimentary rocks as well as felsic and mafic intrusives (Dobmeier & Raith 2003) (Figs. 1 and 2). The ~ 900 km-long mobile belt is oriented northeast-southwest along the eastern coast of India. It is ~ 300 km wide in the north and narrower (~ 100 km wide) further south. The Eastern Ghats Belt is bound to the north by the Singhbhum Craton and to the west by the Bastar Craton, the Dharwar Craton and the Nellore-Khammam Schist Belt. To the east, the EGB disappears into the Indian Ocean.

The Eastern Ghats Belt is divided up into a number of lithotectonic provinces with apparent evolutionary histories distinguishable from one another. Dobmeier and Raith (2003) divided the Eastern Ghats Belt according to lithology, structure and metamorphic grade into the Eastern Ghats Province, the Rengali Province, the Jeypore Province and the Krishna Province. This project focuses solely on the metamorphic

and geochronological evolution of the Eastern Ghats Province rather than all lithotectonic domains. The Eastern Ghats Province (Fig. 2) is the region north of the Gondavari Rift and south of the Mahanadi Rift. It is bound in the west by the Sileru shear zone and is in the vicinity of Visakhapatnam, of Andhra Pradesh, India.

Dominant rock types of the Eastern Ghats Province in decreasing order of approximate abundance include khondalites (garnet-sillimanite-quartz-perthite-plagioclase gneiss), charnockites (hypersthene-bearing quartzofeldspathic granulites), granitic rocks, anorthosites, leptynites (garnet-quartz-perthite gneiss), high-Mg-Al granulites, calc-silicate rocks and mafic granulites. Geochemical studies show that these rocks have sedimentary protoliths (Sen & Bhattacharya 1997) and sedimentation has been reported to have persisted until *ca.* 1.35 Ga and some detrital Archean ages suggest a surrounding Archean Craton may have supplied the sediments (Shaw *et al.* 1997; Jarick 1999). A mixed signature has been reported by Sr isotope data for anorthosites and associated rocks (Sarkar *et al.* 1981) and Sr, Nd and Pb isotope data on khondalites and porphyritic granites (Krause, 1998). This suggests that the orogenic belt contains material of Archean age that was reworked and mixed with more juvenile material during the Proterozoic orogenic cycles (Mezger & Cosca 1999).

Metamorphism in the Eastern Ghats has been the subject of many disparate studies investigating pressure temperature histories at specific locations, which has resulted in a convoluted spread of *P-t* evolutions that are not age constrained (see Figs. 3 and 4). In general, it is accepted that the Eastern Ghats experienced a polycyclic metamorphic history, involving at least two discrete metamorphic events (Dobmeier & Raith 2003). The earliest phase of metamorphism in the Eastern Ghats is most commonly referred to as M_1. This records conditions of ~ 1000 °C and 8 – 10 kbar. *P-T* conditions for the M_1 event have been established by conventional thermobarometry e.g. in metasediments (LAL *et al.* 1987; Kamineni & Rao 1988; Sengupta *et al.* 1990; Sengupta *et al.* 1991; Dasgupta *et al.* 1994; Dasgupta *et al.* 1995; Bose *et al.* 2000; Bhattacharya & Kar 2002), in calc-silicates (Dasgupta *et al.* 1992; Dasgupta 1993; Bhowmik *et al.* 1995; Sengupta *et al.* 1997), and mafic granulites (Dasgupta *et al.* 1991). M_1 metamorphism is considered to occur at *ca*. 1099 ± 56 Ma based on Pb-Pb whole rock – feldspar isochron age of sapphirine-bearing granulites in the Eastern

Ghats Province, as well as 1139 ± 24 from a zircon U-Pb geochronology (both Jarick, 1999). Crowe (2003) relates the SHRIMP zircon $^{207}Pb/^{206}Pb$ age of 1109 ± 9 Ma in a partial melt product to this event.

There are discrepancies in *P-T* path evolutions between different M_1 metamorphic studies. Variations include anticlockwise evolution under fluid absent conditions to peak conditions of 8 – 10 kbar and *ca.* 1000 °C (Sengupta *et al.* 1991; Dasgupta *et al.* 1995) and peak conditions of 12 kbar, 1100 °C followed by 2 kbar of decompression (Dasgupta *et al.* 1991; Dasgupta 1993; Shaw & Arima 1996). Mohan *et al.* (1997) suggests UHT conditions of 8.4 kbar and > 900 °C with decompression by 3 kbar while simultaneously cooling by 150 °C – 200 °C. Contrasting with these calculations, Das *et al.* (2006) argue for 5 kbar and 800 °C prograde metamorphism followed by a peak of *ca.* 4.5 kbar and 900 °C, which they have attributed to asthenospheric upwelling beneath a thinned crust. This was followed by thermal relaxation and cooling at a higher pressure (8 kbar, 700 °C) producing symplectite intergrowths of enstatite + sillimanite. The most recent and widely accepted *P-T* path for the entire Eastern Ghats domain is an anticlockwise *P-T* path characterised by isobaric cooling to 750 °C – 850 °C at pressures of 7 – 10 kbar (Dasgupta & Sengupta 2003).

M_2 metamorphism is considered the dominant fabric defining event (D_2) in the Eastern Ghats (Mukhopadhyay & Basak 2009). This was a granulite-facies reworking of UHT assemblages and reached *ca.* 6 – 8.5 kbar, 800 – 850 °C (Sengupta *et al.* 1990; Dasgupta *et al.* 1992; Sengupta *et al.* 1999; Rickers *et al.* 2001; Dasgupta & Sengupta 2003; Dobmeier & Raith 2003; Simmat & Raith 2008). The metamorphism was followed by a steep decompression and cooling to final conditions of 4 – 5 kbar and 650 – 700 °C (Mukhopadhyay & Bhattachrya 1997).

The D_2 deformational event and M_2 metamorphism is variously constrained by age estimates of 952 – 946 Ma (Jarick 1999), 973 – 954 Ma (Paul *et al.* 1990; Mezger & Cosca 1999). Simmat and Raith (2008) currently provide the most comprehensive dataset of *in situ* monazite geochronology from the Eastern Ghats using microprobe analysis of U, Th and Pb compositions. Their data suggests a metamorphic episode from 950 – 1050 Ma, however it is not related to a particular style of *P-T* path.

Subsequent to M_1 metamorphism there is inferred to be a hiatus before the commencement of M_2 metamorphism, which is punctuated by felsic magmatism (Dobmeier & Raith 2003). This has been dated to be between 985 and 955 Ma (Grew & Manton 1986; Paul *et al.* 1990; Crowe *et al.* 2003). Such ages, however, overlap with M_2 metamorphism estimates, which span *ca* 60 Myr. Earlier emplacement events are also recorded at 1.45 Ga (Shaw *et al.* 1997) and 1.5 Ga (Sarkar and Paul 1998). Limited *in situ* geochronology results in a lack or correlation between metamorphic episodes and geochronology (e.g. Dobmeier and Raith, 2007). Structural interpretation instead has been used to link events (e.g. Bhattacharya *et al.* 1994; Chetty & Murthy 1994; Bhattacharya 1997; Bhattacharya & Gupta 2001; Bhattacharya *et al.* 2001; Bhattacharya & Kar 2002).

Geochronological studies reveal metamorphic ages as young as 800 Ma (Crowe, 2003), 792 ± 2 Ma (Krause *et al.* 2001) and 701 ± 12 Ma (Nanda *et al.* 2008). These ages have been linked to M_2 metamorphism but it is uncertain whether they are related to slow cooling or prolonged high-temperature metamorphism, which may result in late closure of accessory phases such as monazite or zircon grains. Age data of *ca* 550 – 600 Ma has been linked to a third (M_3) metamorphic event (Crowe 2003), which is linked to Pan-African tectonics associated with the collision of East and West Gondwana (Rai *et al.* 2009). This event reached amphibolites facies but affects discrete regions of the terrane; considered to be localised in shear zones (Mukhopadhyay & Bhattachrya 1997). The event was accompanied by hydration and carbonation and has *P-T* conditions estimated at 4 – 5 kbar and *ca.* 600 °C (Mukhopadhyay & Bhattachrya 1997).

The concept of polymetamorphism in the Eastern Ghats belt has been challenged by Bhattacharya and Gupta (2001) and Bhattacharya (1997) who argue that the entire structural sequence in the Eastern Ghats represents a single-cycle or continuum that is related to crustal shortening associated with collision. Their argument is for compressive deformation initiated in a thermally perturbed and partially molten crust. Continued deformation enabled the crust to become refractory and anhydrous, eventually leading to mechanical strengthening of the crust. Gravity data shows that the modern day Eastern Ghats crust represents an over-thickened crustal segment (Subrahmanyam & Verma 1986), which Bhattacharya (1997) argues is due to collision. Other tectonic scenarios that model the Eastern Ghats belt's evolution include

UHT metamorphism resulting from magmatic underplating (Dasgupta *et al.* 1993), anorthositic magmatism (Mukherjee 1989) and horizontal thrusting followed by strike slip tectonics (Chetty & Murthy 1994).

FIELD OBSERVATIONS AND STRUCTURE

The Eastern Ghats Province is defined by a pervasive, upright northeast-trending foliation affecting khondalites and migmatites within the belt. Structural data has previously been used to conclude three major episodes of deformation D_1, D_2 and D_3 affecting khondalites and migmatites (Bhattacharya 1997). D_1 is associated with isoclinals folding (F_1), the development of granulite facies compositional banding (S_1), and also the production of leucosomes. D_2 is defined by the production of another gneissic foliation, S_2, also inferred to have formed during granulite facies metamorphic conditions (Bhattacharya 1997). S_2 transposes $S_1$and the regional tectonic trend of the Eastern Ghats is considered to be defined by a composite S_1/S_2 fabric (Mukhopadhyay & Basak 2009). D_3 deformation is only documented in one area of the Eastern Ghats Province, which is characterised by a tight to open folding event denoted as F_3 (Bhattacharya *et al.* 1994).

In this study, two distinct structural fabrics could be identified. The first structural setting occurred in the east of the study area and the second in the west. In the east, khondalites and migmatites are defined by an upright foliation trending NE-SW with fabric-parallel leucosomes (Fig. 5a). Garnet porphyroblasts occur both in leucosomes and restite layers (5b). Leucosomes vary in style from undeformed to highly-deformed. This area contains folds from approximately 10 cm to 3 metres in size (Fig. 5c.). North of Araku, a second structural setting was identified and a very shallow foliation with a dip of 2 – 10 ° and trending NE-SW parallel to the upright foliation dominated outcrop. In these rocks, leucosomes lay both sub-parallel to mineral compositional banding and also cross-cut melanosomes (Fig. 5d). No folding of leucosomes was observed in this area.

Garnet-orthopyroxene- and K-feldspar megacryst-bearing granitoids and orthogneiss (known as charnockites) dominate parts of the Eastern Ghats terrane as dome-like outcrops. These range from unfoliated or dominated by a weak lineation (L-tectonites) to strongly foliated. In places, they contain rafts

of metasediment from *approx.* 1m – 10m in size (5e). Metasedimentary rafts are commonly folded and contain garnet-sillimanite metasediments that have a gneissic foliation (Fig. 5f).

SAMPLING AND METAMORPHIC PETROLOGY

Samples were chosen that target *P-T* sensitive bulk compositions and differing structural and spatial locations across the orogen. Four samples from different structural settings were chosen for phase diagram analysis. Two of these samples are highly Mg-Al granulites with recognised ultrahigh-temperature mineral assemblages, one is a metasedimentary rock without diagnostic UHT mineral assemblages (Kelsey 2008), the other a recrystallised granite. Three samples containing garnet and biotite were chosen for diffusion-based cooling rate estimations from varying spatial locations.

Sample EG10-063: Migmatitic Khondalite, Vishakapatnam 17 49.505N 83 21.320E

Peak assemblage: garnet + sillimanite + melt + quartz + ilmenite

Post-peak assemblage: garnet + sillimanite + quartz + ilmenite + K-feldspar

This sample contains porphyroblastic, poikioblastic garnet grains comprising part of the peak assemblage. Garnet grains are 0.2 – 0.8 cm in diameter and are euhedral with embayed rims. Inclusions within garnet grains comprise of euhedral quartz and K-feldspar (see Fig. 6a). The foliation is defined by prismatic sillimanite (50 – 200 μm in size), which trend around porphyroblastic garnet grains but are also often in contact with garnet grains (see Fig. 6b). Bladed ilmenite crystals (~ 60 μm) occur in contact with sillimanite or garnet grains. Very fine-grained feldspar intergrowths mantle garnets and often extend as pressure shadow tails beyond the garnets. Medium to coarse grained quartz and K-feldspar comprise the matrix of this sample and display limited to no development of crystal growth parallel to foliation.

Sample EG10-AK3: Al-Mg-rich Metapelite, Anakapalle 17 44.444 N 83 1.207 E

Peak assemblage: orthopyroxene + garnet + ternary feldspar + plagioclase + sillimanite + rutile

Post-peak assemblage: sapphirine + orthopyroxene + K-feldspar + plagioclase + sillimanite + cordierite + biotite + rutile

This rock is dominantly comprised of coarse grained orthopyroxene and garnet grains. Coarse grained orthopyroxene grains are separated from sapphirine-orthopyroxene-cordierite intergrowths by a 50 μm moat of cordierite and k-feldspar. Coarse orthopyroxene grains are 0.5 – 1.0 cm in diameter and consist of irregular shaped grain boundaries and a mantling of fibrous orthopyroxene at the rims within cordierite-k-feldspar grains (Fig. 6c – 6e). Coarse-grained orthopyroxene grains contain microfractures and inclusions of ~ 80 – 100 μm subhedral biotite grains. Coarse-grained biotite grains also occur in contact with orthopyroxene rims and, in places, contain prismatic sillimanite crystals (Fig. 6f). Biotite grains outside of orthopyroxene define a foliation at a different angle to the foliation defined by sapphirine inclusions inside orthopyroxene grains .Vivid blue, needle-like to stumpy sapphirine grains that exist as inclusions in orthopyroxene define a pinch-swell fabric with tapered edges (see Fig. 6d). These sapphirine grains also occur in the matrix in contact with prismatic sillimanite crystals (Fig 6f), or with orthopyroxene, garnet, cordierite and K-feldspar grains (Fig, 6e). Sapphirine grains are also present as inclusions within biotite grains.

Coarse ~ 500 μm anhedral garnet grains contain inclusions of fine ~ 3 μm needle-like sapphirine and euhedral rutile grains and occur in contact with orthopyroxene-sapphirine intergrowths (Fig. 6d) or separated from orthopyroxene by K-feldspar and cordierite rims. Rutile occurs as inclusions within garnet (Fig. 6d) and orthopyroxene grains as well as within the cordierite + K-feldspar matrix, within biotite grains, or amongst sapphirine grains.

Figure 8 shows a compositional map for this sample. It highlights the embayed edges of both coarse orthopyroxene and garnet grains, as well as the complex intergrowths of plagioclase + k-felspar + orthopyroxene + cordierite between the two coarse-grained minerals.

Sample EG10-AK5: Al-Mg-rich Metapelite, Anakapalle 17 44.444 N 83 1.207 E

Peak assemblage: orthopyroxene + garnet + ternary feldspar + plagioclase + sillimanite + rutile

Post-peak assemblage: sapphirine + orthopyroxene + K-feldspar + plagioclase + sillimanite + cordierite + biotite + rutile

The sample is dominated by very coarse-grained orthopyroxene that contains abundant inclusions. Inclusions of medium- to fine-grained garnet are consistently isolated from coarse orthopyroxene by a well developed symplectite intergrowth of sapphirine and orthopyroxene and feldspar mantling garnet with a feldspar corona in direct contact with coarse orthopyroxene (Fig. 6g). Other less common inclusions comprise a complex diamond-shaped intergrowth of fine-grained orthopyroxene + sillimanite + cordierite + sapphirine + feldspar (Fig. 6h, Fig. 7b). That these intergrowths have a diamond shape suggests the former presence of a mineral that has been pseudomorphed. Other inclusions within orthopyroxene grains include fine-grained fibrous sapphirine grains and subhedral biotite grains. A weak fabric is defined by the ovoid shape of inclusions within the very coarse orthopyroxene (Figs 6g and 6i). Sapphirine + orthopyroxene symplectite intergrowths are oriented parallel to foliation around garnet inclusions, pinching together at times (see Fig. 7a). The matrix of the sample is defined by plagioclase, orthoclase and perthite. These exist as either coarse grains or as finer-grained intergrowths (Fig. 6j). Garnet grains in this sample are often very anhedral and may contain inclusions of sillimanite mantling fibrous sapphirine grains (Fig. 6k).

Sample EG10-118: UHT Metapelite, Araku region 18.354741N 82.880958 E

Peak assemblage: spinel + corundum + sapphirine + garnet + sillimanite + magnetite

Post Peak Assemblage: garnet + K-feldspar + biotite + sillimanite + cordierite

Coarse grained garnet, corundum and spinel define a strong foliation in the rock (Fig. 6l, Fig 9). Garnet grains are coarse (~ 0.5 mm by 3 mm) and poikioblastic, containing inclusions of quartz, spinel, orthopyroxene and sillimanite. Within the garnet grains, spinel grains can be subhedral, containing exsolution lamenallae of magnetite ($spinel_{ss}$). Occasionally $spinel_{ss}$ (solid solution) grains have a fine corona of sillimanite or are growing in contact with biotite crystals. Spinel inclusions can also be fibrous (Fig. 6m) grains that do not have a consistent orientation. Within coarse grained garnet, irregular shaped biotite grains occur along micro-fractures. At the rims of coarse-grained garnet, there is a mantling of fine-grained, euhedral garnet (Fig. 6n). Coarse grained garnet defines a strong foliation in the rock, which is overprinted

by a second foliation at approximately 30 º to the first. The second foliation is defined by coarse, anhedral corundum crystals, mantled by a fine corona of garnet (Fig. 6l). Corundum is coarse in size (~ 0.1 – 0.5 cm) and occurs in contact with anhedral ilmenite or sillimanite crystals. Inclusions within corundum include rare euhedral sapphirine and sillimanite grains. Biotite grains are coarse. Biotite grains are aligned along the first foliation. Biotite grains occur in contact with garnet, and are separated from corundum crystals by unoriented coarse-grained sillimanite (Fig. 6l).The matrix of this sample comprises both coarse grained and fine grained K-feldspar and quartz (Fig. 6o).

Sample EG10-136: Mg-Al granulite, Araku region 18.354472N 82.874275E

Peak assemblage: spinel-magnetite solid solution + perthite + biotite + garnet + sillimanite + ilmenite + corundum + quartz

Post-peak assemblage: garnet + K-feldspar + sillimanite + biotite

Large (0.2-0.5 cm by 0.5-2 cm), blocky garnet grains ($garnet_1$) in this sample are highly fractured and contain mineral inclusions (Fig 6q). The inclusions consist of subhedral grains of spinel-magnetite solid solution ($spinel_{ss}$) where spinel grains either contain exsolution lamenallae of magnetite or spinel and magneitite grains occur in contact with each other. These are often mantled by either sillimanite or sapphirine or in some cases both, as sapphirine coronas are further enclosed by sillimanite coronas. $Spinel_{ss}$ inclusions can be found to be in contact with subhedral grains of corundum, magnetite or ilmenite (Fig. 6s). Subhedral quartz grains are found as inclusions within coarse grained garnet as well as euhedral inclusions of biotite grains that occur within garnet, and more fibrous and irregular-shaped biotite grains occur along micro-fractures within the garnet grains. K-feldspar inclusions within garnet grains are perthitic (Fig. 6q) and contain numerous lamellae of plagioclase. These are occasionally separated from their garnet host by a fine rim of K-feldspar, sometimes in contact with biotite inclusions.

Blocky (g1) garnets contain mantling on the edges with a second, fine grained and more euhedral (g2) garnet growth (Fig. 6s). Fine-grained, anhedral biotite occurs in contact with the rims of ‘g1’ garnet grains, within a K-feldspar matrix. Coarse grained corundum also comprised the peak mineral assemblage and defines a foliation in the sample. Corundum grains are typically rimmed by sillimanite and in contact with

ilmenite crystals (Fig. 6r). The matrix of this sample comprises perthitic K-feldspar, with plagioclase exsolution blebs and lamellae. There is a distinct variation in the grain-size of matrix perthite and K-feldspar. Finer grained feldspars occur close to garnets and at the grain boundaries between coarse perthite grains. Coarse perthites are separated from garnet grains by a rim of fine grained K-feldspar.

In contact with fine-grained feldspar grains there also exists coarse ~ 250 μm sized sillimanite crystals. These lie parallel to foliation defined by coarse g1 grains. Sillimanite crystals occur in contact with biotite grains. Coarse-grained sillimanite contain inclusions of anhedral $spinel_{ss}$ and contains irregularly-shaped, needle-like edges (Fig 6p).

Sample EG10-BXX: Garnet-bearing Orthogneiss, central Eastern Ghats 18.36032848N 82.87685537E

Peak assemblage: garnet + quartz + ilmenite + plagioclase + magnetite + orthopyroxene + biotite + K-feldspar + apatite

Post-peak assemblage: garnet + quartz + ilmenite + plagioclase + magnetite + biotite + K-feldspar + apatite

Sample EG10-BXX contains porphyoclastic garnet grains, 0.3 – 1.0 cm in diameter (Fig 6u). Garnet grains define a distinct foliation and enveloped 0.1 – 0.5 cm strain shadows. Garnets contain abundant micro-fractures as well as inclusions of euhedral feldspar, quartz and biotite grains. Pressure shadows comprise biotite, ilmenite, magnetite and apatite. Garnet grains have irregular, embayed edges giving the grains an anhedral habit.

Orthopyroxene is part of the peak assemblage, forming coarse, elongate minerals along the same fabric as the biotite (Fig. 6u). The orthopyroxene grains have as skeletal shape and contain abundant microfractures with no preferential orientation. In parts, orthopyroxene is in contact with magnetite crystals. Magnetite and ilmentite have formed larger subhedral grains, but in strain shadows and the matrix they mostly form bladed crystal grains.

The matrix of sample EG10-BXX contains large (1-3 cm) K-feldspar megacrysts (Fig. 6t). These are oriented parallel to foliation and are oval shaped. This K-feldspar contrasts to the finer grained feldspars in

the matrix. Very fine grained feldspar and quartz crystals are in contact with both garnet crystals and K-feldspar megacrysts, forming a ~ 0.2 cm wide pressure shadow about these porphyroclasts.

Sample EG10-087: Schist, central Eastern Ghats 18 03 20.9N 83 07 21.5E

Peak assemblage: garnet + biotite

This sample contains garnet porphyroblasts of 0.2 – 0.6 cm in size. They are subhedral and contain abundant biotite inclusions. Biotite inclusions are tabular and are partially oriented parallel to the enclosing foliation. Garnet porphyroblasts comprise *approx.* 40 % of the rock and are in contact with foliated, platy biotite grains, which comprise the remainder of the rock (Fig. 6v).

Sample EG10-110: Schist, near Araku 18.268241N 82.880515E

Peak assemblage: biotite + garnet + quartz + ilmenite + spinel

Post-peak assemblage: plagioclase + K-feldspar + quartz + ilmenite + melt

The sample contains large (0.5 – 2 cm in diametre) garnet grains with embayed edges (Fig.6w). Garnet grains contain microfractures and very minor spinel inclusions. Spinel grains are euhedral. Biotite inclusions also exist within the garnet porphyroblasts and are anhedral and ~ 5 – 10 μm in size. The sample contains leucosomes that are 2 – 4 cm wide, and are characterised by a 0.5 cm layer of fibrous biotite separating them from the melanosome. Garnet grains are contained within both the leucosomes and melanosome and between the two layers. The leucosome comprises coarse interlocking K-feldspar, plagioclase and quartz grains. In the melanosome, garnets are in contact with fibrous, foliated biotite grains and fine-grained plagioclase, K-feldspar, and quartz crystals. Ilmenite grains are stumpy and anhedral and exist both in contact with garnet grains and in contact with matrix quartz and feldspars.

METHODOLOGIES

Whole rock and elemental chemistry

Whole rock chemistry data were obtained using solution ICPMS at Amdel Laboratories, Ltd. The sample was fused with lithium metaborate before dissolution and analysed using ICP-MS and ICP-OES (see Payne *et al.* 2010). To determine the amount of FeO in the rocks, wet chemistry (titration) was also performed at Amdel, Australia.

Mineral chemistry spot analyses, including transects across garnet and compositional maps were obtained using the Cameca SX51 electron microprobe at Adelaide Microscopy, The University of Adelaide. For spot analysis beam conditions were a current of 20 nA and an accelerating voltage of 15 kV (including transects across grains). Representative mineral compositions are given in Tables 1 - 5 and all mineral analyses are available upon request of the author. X-ray elemental mapping used a beam current of 100 nA and an accelerating voltage of 20 kV. Fe, Mg, Mn and Ca were measured on WDS spectrometers.

Quantified metamorphic analysis

The rocks were considered to be sufficiently homogeneous to allow for whole rock composition data obtained from Amdel Laboratories, Ltd to be used for metamorphic analysis of peak *P-T* conditions. *P-T* pseudosections were created using THERMOCALC v3.3 (March 2003 update of Powell and Holland, 1988), using the internally consistent dataset tcds55s (Holland and Powell 1998; November 2003 update) so that calculations involving sapphirine could be performed. Pseudosections were calculated using the model chemical system NCKFMASHTO (Na_2O-CaO-K_2O-FeO-MgO-Al_2O_3-SiO_2-H_2O-TiO_2-Fe_2O_3). A-X files used were: White (2007) for garnet, biotite and silicate melt; White et al (2002) for orthopyroxene, spinel and magnetite; Holland and Powell (2003) for cordierite, Holland et al (1996) for osumilite; Holland and Powell (2003) for plagioclase and K-feldspar, White et al (2000) for ilmenite and Taylor-Jones and Powell (2010) for sapphirine.

LA-ICPMS and SHRIMP U-Th-Pb Geochronology

Samples were selected for geochronological analyses that involve different mineral assemblages, compositions and spatial locations across the belt. Rocks containing the upright-foliation as well as the flat-foliation structural settings were analysed to understand the relationship between both domains. Samples

that were forward modelled to create *P-T* pseudosections were also dated to determine links between specific metamorphic events. Monazite grains were analysed *in situ* from various microstructural locations within thin sections to allow for high resolution age data that may be related to differences in the microstructral location of monazite grains (e.g. Kelsey *et al*. 2007).

Sample Preparation

Monazite grains for geochronology were located and imaged using using backscatter electron (BSE) imaging on a Philips XL30 FEGSEM at Adelaide Microscopy, University of Adelaide. Operating procedures included an acceleration voltage of 20 kV and a working distance of 10 mm.

SHRIMP operating procedures and data reduction

Individual monazites were identified in thin section, imaged using BSE and were drilled out from polished thin section, cast in 25mm epoxy disks with chips of the India monazite standard Ind-1 (509 Ma, $^{206}Pb/^{238}U$ = 0.082133) and coated with a thin membrane of gold that produced a resistivity of 10–20 Ω across the disc. Monazite elemental mapping for Ce, Y, Th, U and Pb was undertaken using the Jeol Superprobe at James Cook University in order to visualise variations in monazite chemistry. An accelerating voltage of 15 kV and a current of 250 nA with a step size of 0.5 microns in both the x and y directions were used for electron probe mapping. Maps were processed using Image J software using the garnet look up table. U–Pb isotopic measurements were carried out using the SHRIMP-II at the John de Laeter Centre for Mass Spectrometry, Curtin University, Western Australia, and analysed with ~0.5 nA O_2^- primary beam focused onto ~ 10μm spots, a 5-scan duty cycle, and a mass resolution of c. 5000 (a more detailed description of the Curtin SHRIMP procedure for monazite analysis is provided by (Foster *et al.* 2000). Data reduction was undertaken using Squid software of Ludwig (2001). Isotopic ratios and single spot ages are reported within a 1σ error, while mean ages are given at the 95% confidence level.

LA-ICPMS operating procedures and data reduction

U-Th-Pb analysis of zircon was conducted using an Agilent 7500cs ICPMS coupled with a New Wave 213 nm Nd-YAG laser. Ablation was performed in a helium atmosphere, with a beam diameter of 15 μm, repetition rate of 5 Hz and laser intensity of 70%. Total acquisition time for each analysis was 110 seconds, and involved 30 seconds of background measurement, 10 seconds for beam and crystal stabilisation with the shutter closed, and 50 seconds of sample ablation. Dwell times for isotope measurements were 10ms, 10ms, 15ms, 30ms and 10ms for ^{31}P, ^{204}Pb, ^{206}Pb, ^{207}Pb and ^{238}U respectively. Detailed procedure was completed as outlined in (Payne *et al.* 2008). U-Pb fractionation was corrected using the standard 44069 (Aleinikoff *et al.* 2006) for all samples except EG10-BXX, which was corrected to the MAdel standard (Payne *et al.* 2008). Data reduction was completed using GLITTER software (E. Van Achterbergh 2001). The in-house standard 222 and MAdel were used to monitor accuracy for each sample except EG10-BXX, where 222 and 44069 monitored accuracy. Weighted average $^{207}Pb/^{206}Pb$ age for standard 222 is 464 ± 13 Ma (n = 28, MSWD = 0.33), for MAdel is 523 ± 23 Ma (n = 13, MSWD = 0.063) and for 44069 (for sample EG10-BXX) was 444 ± 42 Ma (n = 14, MSWD = 0.1117) (See Appendices 1).

Conventional concordia plots and discordia chords were generated using Isoplot/Ex 3.00. Errors shown on the concordia diagrams and quoted in the data tables are at the 2σ level.

Garnet cooling rate estimates

Conventional temperature estimates preserved by the analysed chemistry of garnet cores or rims were obtained using THERMOCALC v.3.21, using the compositional of analysed biotite grains in contact with garnet and garnet compositions at rims or cores. Activities of garnet and biotite end members were calculated using software AX (Powell *et al.* 1998). Estimates of cooling rate were modelling using the diffusion code of Robl *et al* (2001). This requires X_{Mg}* [Mg/(Fe + Mg)] values of biotite grains in contact with garnet grains. A linear model of cooling was used to model various cooling rates and transects of X_{Mg}* across the radii of garnet grains were compared to the forward-modelled profiles. In three samples, 14 profiles were measured along garnet grains with care taken to ensure analyses were measured on garnets that had been cut through their centres. Four transects from various-sized garnet grains free from biotite inclusions within garnet grains were chosen for temperature-time modelling. Starting temperatures used for

calculations were 900 °C and end temperatures were the temperatures recorded from conventional thermobarometry from the rims of the garnet grains (see Table 13).

RESULTS

Mineral Chemistry

Garnet

Sample EG10-063 is dominated by almandine-rich garnet with X_{Fe} [Fe/(Mg+Fe+Ca+Mn)] values of 0.701 – 0.709 and X_{Mg} [Mg/(Mg+Fe+Ca+Mn)] values from 0.239 – 0.250. Garnet grains in this sample contain very little manganese with X_{Mn} [Mn/(Mg+Fe+Ca+Mn)] of *approx.* 0.008 and also lack grossular-rich garnets with X_{Ca} [Ca/(Mg+Fe+Ca+Mn)] of *ca* 0.04.

Mg-Al granulite samples EG10-118, EG10-AK5 and EG10-136 all contain garnet that is dominated by almandine-pyrope solid solution ranging in X_{Mg} of 0.42-0.58 and X_{Fe} of 0.42 - 0.51. Figure 15 demonstrates there is little compositional change in cations across a garnet grain of sample EG10-AK5.

Figures 10, 11, 12, 13 and 14 show garnet compositional maps and X_{Mg} and X_{Mg}* [Mg/Fe + Mg)] profiles across garnet grains suitable for diffusion-based cooling estimates. Higher X_{Mg} values occur in the cores of garnet grains and lower X_{Mg} at the rims. The maps all describe similar features in the compositions of garnets, with distinct, but gradual decrease and increase of magnesium and iron (respectively) from the cores to the rims. All samples show an increase of calcium content towards the rims, but garnet 1 in sample EG10-BXX shows the most distinct variation in calcium composition between cores and rims. At the core X_{Ca} is *approx.* 0.9 and at the rims X_{Ca} = is *approx.* 0.15. There is little change in manganese content from the cores to the rims in any of the samples.

X_{Mg}* values range from 0.19 – 0.29 for Sample EG10-087, 0.19 – 0.29 for sample EG10-110 and 0.15 – 0.25 for sample EG10-BXX. EG10-BXX contains garnet grains that the most grossular-rich of all of the samples and contains XCa of 0.66. This sample also contains garnet grains rich an almandine with X_{Fe} of

0.69. $X_{(g)}$ [Fe/(Fe + Mg)] of garnet cores in sample EG10-BXX is approximately 0.72 – 0.74 and 0.78 – 0.8 at the rims. At the cores and rims of garnet grains $Z_{(g)}$ [Ca/(Ca + Fe + Mg)] corresponds to values of 0.1 and 0.13, respectively.

Orthopyroxene

In sample EG10-AK5, there are two compositionally distinct types of orthopyroxene grains. The first type of orthopyroxene (opx_1) occurs as fibrous symplectite growths with sapphirine and also as coarse grains. These grains contain y(opx) 0.140 – 0.177 (see Fig. 16f). The second type (opx_2) occurs in a symplectite microstructure composed of orthopyroxene, sapphirine, cordierite, K-feldspar and sillimanite which contains a y(opx) of 0.07 – 0.1 (see Figs. 16 a – 16e). Orthopyroxene transets across grains in sample EG10-AK5 (Fig. 16) all show a composition trend in its aluminium content across grains. Opx_1 show cores that contain higher aluminium content that the rims. In sample EG10-BXX, y(opx) values are lower than sample EG10-AK5, ranging from 0.006 – 0.0.007.

Sapphirine

Sapphirine in each sample is aluminous with a consistent Al_2O_3 of ~ 57.0 wt %. The sapphirine is stoichiometry of sapphirine grains between samples shows some variability, as displayed in Fig. 17. Sample EG10-136 shows a broader spead of sapphirine compositions than sample EG10-AK5 or EG10-118. Between samples, sapphirine grains have ~1 wt % Cr_2O_3, and a consistent ~15 wt % MgO.

Cordierite

Sample EG10-AK5 is more magnesium than sample EG10-118 with X_{Mg} values of 0.88 and 0.72 respectively. Sample EG10-118 cordierite grains contain 0.31 – 0.38 wt % Na_2O and are more sodic than sample EG10-AK5 cordierite grains which contain 0.03 wt % Na_2O.

Alkali feldspar

Figure 18 shows a compositional transect across a feldspar grain in the matrix of the sample, displaying plagioclase-rich rims and an orthoclase rich core. Figure 19a displays compositions of all feldspars of all samples. Sample EG10-BXX contains plagioclase that is more calcium rich than other samples, with $X_{(an)}$ [Ca/(Na+Ca+K)] values of approximately 0.5, than samples EG10-AK5 and EG10-136 with $X_{(an)}$ values ranging from 0.21 – 0.35. Sample EG10-BXX also contains orthoclase, which occur with an $X_{(K)}$ of 0.85 – 0.88. Sample EG10-AK5 contains orthoclase, mesoperthite, antiperthite and albite feldspars. $X_{(K)}$ values for this sample ranges from 0.02 – 0.87. Sample EG10-136 shows two compositionally variable plagioclase feldspars (see Fig. 19b) depending on their microstructural location within the sample. Occurring as inclusions within garnet, feldspars range from antiperthite to mesoperthites with $X_{(K)}$ [Ca/(Na + Ca + K)] ranging from 0.23 – 0.44 and $X_{(an)}$ from 0.42 – 0.54. Occuring within the matrix of the sample, oligoclase to mesoperthitic feldspars have $X_{(an)}$ of 0.51 – 0.58. Orthoclase feldspars also reside in the matrix and as inclusions in garnet with $X_{(K)}$ values of approximately 0.87. Sample EG10-118 contains the most K-rich, orthoclase with $X_{(K)}$ values of 0.88 – 0.93.

Biotite/Phlogopite

Biotite analyses in EG10-AK5 show two compositionally distinct types of biotite, one that is low in TiO_2 (0.17 wt %) and has an $X_{(Mg)}$ of approximately 0.72 resides within a symplectic microstructure composed of orthopyroxene, sapphirine, cordierite, K-feldspar and sillimanite. Biotite within the symplectite growth surrounding garnets has a ~ 5.0 wt % TiO_2 and X_{Mg} values of approximately 0.82.

Phlogopites within Mg-Al granulite samples EG10-136 and EG10-118, and garnet-biotite schist EG10-110 shows just one main composition, whether growing as inclusions within garnet or on the edges of garnets in the matrix. These have ~ 8 - 10 wt % K_2O, and consistent TiO_2 values of 4 – 5 wt %. Phlogopites in sample EG10-087 are less titanium rich with 1 – 2 wt % TiO_2. EG10-136, EG10-118 and EG10-087 are more magnesian than EG10-110, with $X_{(Mg)}$ values of 0.7 – 0.8 compared to 0.6 – 0.7, respectively.

Spinel

In sample EG10-136, spinel exhibits solid solution with magnetite. Spinel is mainly reduced, with ($Fe^{3+}/(Fe^{3+} + Fe^{2+})$) values 0.10 – 0.2. Spinel grains in sample EG10-118 contain less (0.0002 wt %) Cr_2O_3 than in sample EG10-136 (0.02 wt %). ZnO wt % varies in both samples between 7 – 8.6 wt % and sample EG10-118 contains less titanium with approximately 0.0002 wt % TiO_2 compared to 0.15 – 0.164 in sample EG10-136. Both samples have spinel grains with $X_{(Mg)}$ values of 0.4 – 0.5.

Magnetite

Magnetite occurs in samples EG10-BXX and EG10-136. Sample EG10-BXX contains less TiO_2 with approximately 0.0002 wt % compared to magnetite grains in sample EG10-BXX with approximately 0.02 wt % TiO_2.

Corundum

Corundum in samples EG10-118 and EG10-136 has a minor (~1 wt %) iron Fe_2O_3 incorporated in its structure.

Ilmenite

Ilmenite in sample EG10-118 is more oxidised than in sample EG10-136 [(Fe3+/(Fe3+ + Fe2+) = 0.30 and 0.08 respectively]. Sample EG10-136 is more titanium-rich with ~ 40 wt % TiO_2 compared to sample EG10-118's ~ 20 wt %. Ilmenite in sample EG10-BXX has slightly more titanium-rich with 52 wt % TiO_2 and is completely reduced, which is almost analogous in ilmenite from sample EG10-063.

Sillimanite

Each sample has a minor incorporation of iron (0.4 – 1 wt % Fe_2O_3).

PHASE DIAGRAM ANALYSIS

Sample EG10-063

The field containing the peak mineral assemblage occurs above 750 ºC at pressures between *ca* 6.5 and 10.5 kbar. The absence of kyanite suggests that temperatures below *ca* 680 ºC were not attained. No overall *P-T* path could be described for the sample. An upper limit on the peak temperature can also not be restrained.

Sample EG10-AK5

The field containing the peak mineral assemblage is constrained to pressures of 10.5 – 11.5 kbar and temperatures of 1030 –1100 ºC (Fig. 21a). The absence of quartz from the sample confines the field to above 1000 ºC. Loss of garnet from the peak assemblage then constrains the post peak assemblage to a narrow field with a wide range of pressures from 5 – 10.5 kbar and temperatures of 940 – 1040 ºC. Cordierite and post-peak biotite in the sample reveal that the sample reached pressures of 3 – 5 kbar and temperatures of 850 – 950 ºC. Biotite inclusion in garnet in the sample indicates that pre-peak conditions included pressures of 10.5 – 11.5 kbar and temperatures of *ca.* 900 ºC. This sample has been contoured for the aluminium content of orthopyroxene [y(opx)] to further constrain *P-T* conditions of the sample. This demonstrates y(opx) values increase up pressure and temperature. In the peak field the y(opx) values are 0.160 – 0.165 corresponding with opx_1 (see mineral chemistry). This suggests that pressures could be as high as 12.5 kbar. The presence of sapphirine in the post-peak assemblage constrains the peak pressure to lie below 12.5 kbar. The presence of ternary feldspars also attests to higher temperatures. The feldspar exsolvus is shown by the dashed line on Fig. 21a above pressures of 11.5 – 12.5 kbar and temperatures of *ca.* 900 ºC. The sample's post peak assemblage corresponds to y(opx) values of 0.06 – 0.1. $Orthopyroxene_2$ (see mineral chemistry) contain values of y(opx) ranging from 0.073 – 0.106, placing the post-peak mineral assemblage at pressures of 4 – 5 kbar, 860 – 940 ºC. The overall trajectory described is clockwise with a flat prograde path showing little change in pressure but a change in temperature of *ca* 100 ºC followed by a steep retrograde path with little change in temperature (50 – 150 ºC) compared to the *ca* 6.5 kbar change in pressure.

Sample EG10-BXX

The peak mineral assemblage of garnet + quartz + ilmenite + plagioclase + magnetite + orthopyroxene + biotite + K-feldspar + apatite is constrained within pressures of 5 – 10 kbar and temperatures at *ca* 875 ºC.

The presence of interpreted peak or slightly post-peak biotite in the sample constrains the upper limit on temperature and the presence of orthopyroxene constrains the lower limit of temperature. The presence of magnetite in the sample's peak assemblage constrains the peak field to pressures below *ca* 10 kbar. The absence of orthopyroxene from the post-peak mineral assemblage constrains the post-peak mineral assemblage to temperatures below *ca* 850 ºC, but with no lower limit.

Garnet compositional contours (Fig. 23) show an increase in $X_{(g)}$ [Fe / Fe + Mg] down pressure and temperature. They also describe a decrease in $Z_{(g)}$ [Ca/(Ca + Mg + Fe)] down pressure and slightly decreasing up temperature. Profiles in calcium content of garnet grains in sample EG10-BXX (Figs. 10 and 11) across garnets show an increase from core to rim. Garnet cores have Z(g) compositions of *ca.* 0.09 and rims of 0.13. The iron content also increases from cores to rims. The values based on mineral chemistry of the cores and rims of garnet grains in sample EG10-BXX constrain *P-T* estimates as shown by the labelled circles on the *P-T* pseudosection. The aluminium content of orthopyroxene [y(opx) = Si + Al - 2] values decrease with increasing pressure and decreasing temperature. Y(opx) values in EG10-BXX constrain the sample to lie within the highest pressures and lowest temperatures available in the field at 10 kbar, 875 ºC.

Sample EG10-136

The earliest assemblage preserved in *P-T* space is shown by the oval on Fig. 25a, constrained by the presence of quartz inclusions within coarse-grained garnet growth. The peak assemblage of spinel-magnetite solid solution + perthite + biotite + garnet + sillimanite + ilmenite + corundum + quartz for the sample is then constrained to pressures of 8.3 – 9.5 kbar and temperatures of *ca* 910 ºC. The post peak mineral assemblage of this sample does not contain corundum, sapphirine or spinel, but is characterised by an increase in garnet, implying a recorded decrease in temperature of the sample. The sample does not contain post-peak quartz, constraining post-peak temperatures to be above 880 ºC. The sample is also constrained to pressures above *ca.* 8 kbar, due to the absence of orthopyroxene. The sample could follow a near-flat or decompression to *ca*. 9 kbar retrograde *P-T* path, should biotite inclusion be a later feature than

early corundum + sillimanite + $spinel_{ss}$ + sapphirine such as within field 8 on Fig. 24. This would allow for peak pressures of 10 – 11.5 kbar.

Contouring of the pseudosection (Fig. 25) allows for the best possible estimate of the samples *P-T* evolution. $X_{(g)}$ contours of the pseudosection shows an increase up temperature, but with values that are lower than the mineral chemistry of the garnet in the sample. $Z_{(g)}$ [$Ca/(Fe^{2+} + Mg + Ca)$] values correspong to $garnet_1$ (see mineral chemistry) values, suggesting *P-T* conditions above 8.6 kbar and 930 ºC . $Garnet_2$ corresponds to the same $Z_{(g)}$ values and *P-T* estimates. $X_{(sp)}$ [$Fe^{2+}/(Fe^{2+} + Mg)$] show values that increase with decreasing temperature. The values of $X_{(sp)}$ (*ca.* 0.5) do not match to the contours calculated on the pseudosection, and if the trend continued, would correspond to peak conditions at a higher temperature of *ca*. 970 ºC. The value of $X_{(sa)}$ [Fe/ (Fe + Mg)] show increasing values with decreasing temperature. The *P-T* pseudosection has been contoured for mineral abundance in Fig. 25b. Mineral abundance contours show that with decreasing temperature, abundance of sapphirine, corundum and spinel all decrease, which supports the argument for post-peak conditions at temperatures below peak conditions. The overall trajectory is deduced to be anticlockwise, to follow a decrease in the mineral abundance of spinel, which is absent from the post-peak assemblage. The absence of orthopyroxene from the sample's mineral assemblage inhibits the interpretation of any significant decrease in pressure (pressures remained above *ca.* 8.3 kbars). The peak *P-T* conditions recorded by the entire peak assemblage is at 8.3 kbar and *ca*. 900 ºC followed by peak minerals at a higher temperature and a decrease in temperature described by mineral abundance contours which show decrease in corundum + spinel + sapphirine.

GEOCHRONOLOGY

SHRIMP and LA-ICPMS U-Pb monazite data are reported in Table 12.

Sample EG10-063

Monazite grains on the edges of garnets and in the matrix were targeted, as no monazite grains included within garnet grains were present in the sample. Compositional maps show little variable zoning of monazites in this sample in Y, Pb or Ce but a high Th and Pb rim can be identified.

Fifteen analyses of 8 monazite grains were conducted. All age data is plotted on a conventional concordia with images of representative monazite grains in Fig. 26. A weighted average plot is also included as Fig. 26b for $^{207}Pb/^{206}Pb$ age estimates. The concordia plot for this sample shows very discordant age data with an upper intercept of 1013 ± 42 Ma and a lower intercept of 474 ± 230 Ma (n = 15, MSWD = 1.05). The $^{207}Pb/^{206}Pb$ weighted average age is 942 ± 12 Ma (n = 14, MSWD = 1.3).

Sample EG10-AK3

22 analyses of 11 monazite grains were conducted. Representative compositional plots of monazite grains are shown in Fig. 27a – 27d. Three series of monazite grains could be identified by compositional maps. The first series contain high yttrium-cores (Fig. 27a), surrounded by secondary, low-yttrium growth. This is then encompassed by moderate to high-yttrium rims, with the highest yttrium values at the very edges of the rims. The second series (Fig. 27b) of monazite grains contain low-yttrium cores with heterogeneous and complicated yttrium-zoning, surrounded by moderate to high yttrium rims, with the highest values at the very edges of the rims. The third series (Fig. 27c) of monazite grains have high Y values, low uranium and rims of high Pb and Th. A fourth series (Fig. 27d) also shows no compositional zoning and low-Y values. These are the smallest monazites that were analysed (< 30 µm). The first series of monazites contain a low-Th $core_1$, high Th core $_2$ and moderate rims. Lead has no significant zoning apparent in the compositional maps. The second series of monazites contain high Th cores and moderate to low Th-rims. Uranium in these monazites is low compared to other monazites with a complex high-U rim surrounding the core and low values again at the rim. This corresponds to a high-Th core and a low-Th rim. Compositionally, lead follows the same pattern as uranium. Fig. 27e shows a $^{207}Pb/^{206}Pb$ weighted mean average plot of analyses taken from the high-Y cores of series 1 monazite grains corresponding to 976 ± 6 Ma (n = 7, MSWD = 1.01), the second outer-most rim, which has low-Y composition corresponds to a $^{207}Pb/^{206}Pb$ weighted mean average age of 969 ± 12 Ma (n = 9, MSWD = 5.0) (Fig. 27f) and the outermost rims of series 1, 2 and 3 of monazite grains display a $^{207}Pb/^{206}Pb$ weighted mean average age of 983 ± 18 (n = 6, MSWD = 4.7) (Fig. 27g).

A conventional concordia plot of all analyses is shown in Fig. 28a. This shows a discordia with an upper intercept of 989 ± 21 Ma and a lower intercept of 318 ± 310 Ma (n = 33, MSWD = 2.2). The $^{207}Pb/^{206}Pb$ weighted mean average age (shown in Fig. 28b), shows an average age of all monazites as 973 ± 8.8 Ma (n = 29, MSWD of 1.18).

Sample EG10-AK5

56 analyses on 34 monazites were conducted on this sample. Monazite were targeted from within different mineral textural locations in the sample, shown in Fig. 29i, with a particular emphasis to target monazite grains from within coarse grained orthopyroxene, porphyroblastic garnet grains, coarse grained feldspar grains and symplectite mineral intergrowths. The monazite grains all show very irregular and inconsistent habits with no systematic shape of monazite grains observed (Fig. 29e and Fig. 29f).

A conventional concordia plot of the sample is shown in Fig. 29a. This displays a discordia with an upper intercept of 943 ± 39 Ma and a lower intercept of 680 ± 68 Ma (n = 55, MSWD = 5.0). The $^{207}Pb/^{206}Pb$ weighted mean average age is 885 ± 15 Ma (n = 51, MSWD = 4.4). A frequency histogram describing the spread of data is shown in Fig. 29h.

Depending on textural location, different monazite ages are inferred. Any monazite grain within the sapphirine + orthopyroxene symplectite mineral texture was characterised as ‘younger monazite data’ with the rest as ‘older monazite data’. Older monazite analyses are taken on monazite grains from within coarse-grained orthopyroxene grains, porphyroblastic garnet grains or feldspar crystals. Older data is displayed on a conventional concordia plot in Fig. 29c and clusters with a weighted mean average $^{207}Pb/^{206}Pb$ age of 933 ± 20 (n = 15, MSWD = 1.9) (Fig. 29d). Younger data sits on a conventional concordia plot (Fig. 29f) with an upper intercept of 952 ± 74 Ma and a lower intercept of 639 ± 92 Ma (n = 15, MSWD = 6.5). Its $^{207}Pb/^{206}Pb$ weighted mean average age (Fig. 29g) is 860 ± 30 Ma (n = 17, MSWD = 5.3).

Sample EG10-BXX

25 analyses from 14 different monazites were conducted on this sample. A conventional concordia plot of all data (Fig. 30a) shows a discord with an upper intercept of 938 ± 140 Ma and a lower intercept of 580 ± 320 Ma (n = 25, MSWD = 1.7). A $^{207}Pb/^{206}Pb$ weighted average age estimate (Fig. 30b) shows a mean age

of 877 ± 42 Ma (*n* = 23, MSWD = 9.2). Backscatter electron images of monazites show no growth patterns, yet data was divided depending on textural location of monazites. A cluster of age data (Fig. 30d) represents monazites armoured within garnet grains. These have a $^{207}Pb/^{206}Pb$ weighted mean average age of 938 ± 23 Ma (*n* = 13, MSWD of 1.5) (Fig. 30h). Monazite grains situated within the matrix show a greater smear across a discordia with an upper intercept of 890 ± 370 Ma and a lower intercept of 523 ± 630 Ma (MSWD = 2.4). The Pb^{207}/Pb^{206} weighted mean average of matrix monazite data shows an age estimate of 763 ± 68 Ma and a MSWD of 10.3.

Sample EG10-087

21 analyses from 7 different monazite were conducted. All monazites resided within the biotite matrix of the schist. Some monazites were located on edges of garnet porphyroclasts, however were not suitably large enough to analyse. BSE images of monazites show some compositional zoning of cores and rims (see Fig. 31c). All analyses were conducted on cores. Data was plotted on a conventional concordia diagram in Fig. 31a, showing just one cluster of ages. A $^{207}Pb/^{206}Pb$ weighted mean average age of 965 ± 17 Ma (*n* = 21, MSWD = 0.39) is shown in Fig. 31b.

Sample EG10-118

24 analyses of seven monazite grains were conducted. Monazite grains from within the matrix mineral assemblage and within coarse grained feldspars were targeted. Compositional maps of monazite grains are shown in Figs. 32a – 31c. Compositional maps show monazite grains have two distinct zones. The cores of the monazite grains show heterogeneous and high Y compositions, with compositionally-homogeneous, lower Y rims. Rims are high in Th and Pb. Analyses of monazite cores show age data with a weighted mean average of 903 ± 32 Ma (*n* = 17, MSWD = 9.4) (Fig. 32e) and from rims of 903 ± 30 Ma (*n* = 6, MSWD = 1.4) (Fig. 32f).

All age data is plotted on a conventional concordia in Fig. 33a. A weighted average plot is also included as Fig. 33b for $^{207}Pb/^{206}Pb$ age estimations. Two analyses of one monazite were discarded from the calculation of results due to high common lead. This monazite was small (~ 80 µm long, 30 µm in width), resulting in spots on the high Pb rims. In this sample, U-Pb discordia shows an upper intercept of 1003 ± 49 Ma and a

lower intercept of 613 ± 83 Ma (*n* = 23, MSWD = 1.13). $^{207}Pb/^{206}Pb$ weighted average mean estimate gives an age of 928 ± 14 Ma (*n* = 19, MSWD = 1.6).

Texturally, monazites armoured within spinel display more clustering (Fig. 32c) and intercept conventional concordia at 917 ± 18 Ma. Weighted mean average ages for these calculation is shown in Appendices 2. Within the matrix the age represents a more widely-spread discordia with an upper intercept of 1035 ± 94 Ma and a lower intercept of 636 ± 96 Ma (*n* = 16, MSWD = 4.8) (Fig. 33d).

Sample EG10-136

19 analyses on 6 monazites were conducted on sample EG10-136. Compositionally, monazite grains show a core with heterogeneous Y concentrations and a low-Y rim (Fig. 31d – 31e). The Th and Pb values of the core are low, and the rims are high.

A conventional concordia plot (Fig. 34a) of all spots shows a discordia with an upper intercept of 988 ± 48 Ma and a lower intercept of 579 ± 150 Ma (*n* = 19, MSWD = 1.8). Fig. 34b shows $^{207}Pb/^{206}Pb$ weighted average age estimate of 928 ± 14 Ma (*n* = 19, MSWD = 3.2). Texturally, monazites located within coarse-grained feldspars show a greater clustering of age estimates (Fig. 34c) compared to the discordant matrix-hosted monazite grains (Fig. 34d).

Conventional Thermobarometry and diffusion-based modelling cooling rates

Sample EG10-110

Results show that the cores of garnets in this sample record Fe-Mg exchange thermometry temperatures of *ca.* 650 – 750 ºC with the highest temperatures preserved within the cores of the largest garnet grains. The rims show temperatures of 500 – 690 °C. A curve with an estimation of X_{Mg} within biotite prior to diffusion of 0.6 shows that a slope with a rate of 5 °C/My is the best fitting rate (Fig. 35c).

Sample EG10-087

Results show that the cores of garnets in this sample record temperatures of *ca.* 580 – 600 °C and rims preserve temperatures of 470 – 485 °C. A curve with an estimation of X_{Mg} within biotite prior to diffusion of 0.6 shows that a slope with a rate of 0.1 °C/My is the best fitting rate (Fig. 35d).

Sample EG10-BXX

The larger garnet grain, EG10-BXX Garnet 1 shows core temperatures at *ca.* 690 °C and the smaller garnet grain shows core temperatures of 670 °C. Both samples contain garnets with rims recording temperatures of 570 – 580 °C. The best fitting cooling rate model for Garnet 1 is a rate of 0.05 °C/My and for Garnet 2 is 0.1 °C/My (Fig. 35a and b).

DISCUSSION

Interpretation of geochronology

In this study, monazite U-Pb geochronology has been directly coupled with *P-T* phase equilibria from the same samples to constrain the timing of metamorphic episodes in the Eastern Ghats Province. To correctly interpret this data it is necessary to comprehend what stage of the metamorphic cycle monazite growth has responded to. The growth and dissolution behaviour of monazite is affected by a variety of physical and chemical variables (Kelsey *et al.* 2008). Studies have shown that metamorphic monazite grows rapidly at mid- amphibolite grade and above (Smith & Barreiro 1990) and Rubatto *et al.* (2001) demonstrate that monazite growth is a response to prograde metamorphism. Monazite geochronology is particularly useful for UHT terranes because monazite grains can have a high (> 900 °C: Cherniak *et al.* 2004) closure temperature, but still a broad stability range (Harrison *et al.* 2002). The textural location of monazite can affect its growth with grains amoured within minerals such as garnet often resulting in different ages compared to matrix-hosted monazites (e.g. Cutts *et al.* 2010; in press, Montel *et al.* 2000).

This study recorded variability in U-Pb monazite ages depending on spatial location across the orogen as well as textural location within the sample. Identification of the timing of monazite growth with respect to the major mineral phases in a sample can be enhanced by analysing compositional zoning within the

monazite grains. Monazite grains can contain 40 – 80 % of a rock's REE quota (Bea 1996). As metamorphic minerals grow and interact with monazites, specific trace element zoning signatures can be recorded in the monazite grains (Kelly *et al.* 2006). Distinct age domains can then correlate to compositional variations (Cherniak *et al.* 2004). In this study, compositional zones within monazite grains were not found to hold any direct correlation to the age of the monazite grain. Monazite compositional maps can still, however, provide important geochemical markers of mineral growth and breakdown during metamorphism (Kelly *et al.* 2006) as monazites may grow or be consumed as major reactions proceed (Spear & Pyle 2002). The element yttrium (Y), for example, is a REE that is particularly compatible with garnet so its integration into monazite grains depends on the metamorphic growth of coexisting garnet (Pyle & Spear 2003).

The oldest average ages in this study of 975 ± 9 Ma and 973 ± 7 Ma were recorded by samples EG10-063 and EG10-AK3, respectively, from the eastern margin of the belt. Sample EG10-063 contains monazite grains that are dominantly located in contact with rims of garnets, show no compositional zoning and are rich in Y. This data suggests that monazite growth represents exclusively one metamorphic cycle (Spear and Pyle 2002), and high-Y values suggest growth may be at the expense of garnet (Pyle & Spear 2000) or may predate the garnet. In contrast, monazite grains within sample EG10-AK3 have more complex zoning patterns, with four different series of monazite grains identified according to their zoning pattern (See Fig. 27a – 27d). Complicated zoning in Sample EG10-AK3 indicates monazite grains that have undergone a series of growth and resorption reactions throughout their history, correlating to reactions involving major phases in the rock (Spear & Pyle 2002). High-Y rims could indicate initial growth of monazite during breakdown of garnet. Such interpretation is supported by textural evidence for garnet breakdown, including sapphirine and orthopyroxene symplectite growth around garnet grains. Figures 27e – 27g shows age plots of the three main identified zones in sample EG10-AK3 monazites. These plots demonstrate that there is little correlation between the age of the spot and the compositional zone it was taken from, as all three ages are within uncertainty of each other. Spear and Pyle (2002) demonstrate that the growth of one compositional zone may not indicate its presence as a part of the stable equilibrium assemblage in the rock. Lack of correlation could be due to consecutive re-precipitation of monazite grains above the closure

temperature of monazite within the time period reflected by the uncertainty of the analysis technique. In the Eastern Ghats, samples have experienced high-grade metamorphism and complex zoning may also be due to production, crystallisation or loss of silicate melt (Spear & Pyle 2002).

The two easternmost samples record effectively identical ages. These ages are interpreted to constrain the age of formation of the upright foliation within the belt. This foliation, however contains folding, which could be due to two metamorphic events (e.g. Bhattacharya & Gupta 2001), with monazite growth most likely relating to the second metamorphic episode (M_2). If monazite grains grew during the earlier metamorphic episode their chronometers appear to have been reset as a result of overprinting UHT-metamorphism. The steep foliation from the eastern region of the belt has also been dated by sample EG10-087, which yields an age of 965 ± 17 Ma, within uncertainty of the inferred *ca.* 975 Ma metamorphism.

A spatial trend across the belt is noted, with monazites armoured within porphyroclastic garnets of EG10-BXX, recording ages of 938 ± 23 Ma. Garnet-armoured monazite ages of *ca.* 940 Ma could be interpreted in a number of ways. Firstly, the monazite in the garnet could be inherited from the source of the granite protolith. This scenario implies that magmatism that is coeval with metamorphism and the source of the granite could derive from large-scale partial melting. On the other hand, the protolith granite could be older than 940 Ma but there are no igneous monazites in this sample. Harvey (2010) demonstrates that U-Pb ages of K-feldspar megacryst granites may have older *ca.* 1.2 Ma signatures. If these K-feldspar-megacryst granites were emplaced at the same time as sample EG10-BXX, it would then follow that the ages determined by this study were solely metamorphic.

In the western region of the province where the fabric has a shallow orientation, samples EG10-136 and EG10-118 have younger ages of 928 ± 23 Ma and 908 ± 39 Ma (respectively) not within error of the upright-foliation samples. Both samples record metamorphism within error of *ca.* 925 Ma. Monazite compositions in sample EG10-136 display high-Y values at the core and successive, low-Y values at the rims. This pattern can be related to the metamorphic *P-T* path of this sample, which describes growth of secondary garnet on the retrograde path of isobaric cooling. This suggests that monazite growth is retrograde with secondary garnet growth acting as the alternative reservoir for yttrium. In sample EG10-

118, however, once again monazite cores record metamorphism that is within uncertainty of the age of the rims (Fig. 33e and 33f), suggesting that variability in composition is not related to a distinctly separate metamorphic episode.

The study therefore concludes that the age of metamorphism varies between *ca.* 50 My from the east to the west of the belt. A spatial trend in the age of metamorphism has been recorded in other high-grade metamorphic belts Kelsey *et al.* 2010 and could record a shift in the locus of metamorphism across the belt Kelsey *et al.* 2010. It is possible, however that a trend in ages is a result in variations in the timing of monazite growth depending on the bulk composition of the rock (Fitzsimons *et al.* 2005) or differences in the timing of exhumation.

The ages of peak or near peak metamorphism from across the study area suggest that metamorphism occurred in the period of *ca.* 975 – 925 Ma. A metamorphic age of 980 – 940 Ma is consistent with published geochronological data from the Eastern Ghats (e.g. Dobmeier and Raith, 2003). This event is commonly labelled M_2 and is considered the dominant fabric forming event of Eastern Ghats Province.

Evidence for post-975 Ma metamorphism

Previous authors have indicated the presence of metamorphic events in the period of ~ 700 – 800 Ma and another related to the Pan African orogeny at *ca.* 550 Ma (e.g. Simmat & Raith 2008). This study provides some evidence for one younger event. Sample EG10-AK5 yields a weighted average $^{207}Pb/^{206}Pb$ age of 885 ± 15 Ma. Inspection of this data, however, shows a smear of ages from approximately 943 ± 39 Ma down to *ca*. 680 ± Ma. This could be interpreted in several ways: (1) it may represent the age of a younger event at 885 ± 15 (2) record the age of cooling below monazite closure temperature for this sample, i.e. high-temperature conditions were maintained in this case (3) be due to partial Pan-African-aged partial-recrystallisation of monazite grains. These three options will be discussed below.

Circa 800 Ma metamorphism has been previously proposed in the Eastern Ghats (Crowe 2003). There are no metamorphic textures or *P-T* paths yet shown to be related to this metamorphism, however, and a paucity of *in situ* geochronology coupled with *P-T* phase diagram analysis leaves this option unsupported in the study by Crowe (2003). A younger age of 885 ± 15 Ma could be a result of prolonged exposure of

monazite grains to high temperature conditions. The closure temperature of monazite depends on many variables such as grain size of the monazite or the pH of the enclosing environment (Cherniak *et al.* 2003), thus it is difficult to pin-point at what exact temperature monazite grains stopped diffusing. High temperatures coupled with slow cooling could infer extended periods of diffusion and resetting of U-Th-Pb geochronometres in monazite grains. This interpretation is strengthened by the interpretation of texturally-distinct age populations. The geochronology results display a consistent smear in age data in all samples except EG10-087. Using *in situ* analysis of monazites provides clarity for samples with various populations of monazites (Catlos *et al.* 2002) and this study reveals monazite grains in the matrix or along micro-fractured mineral grains significantly younger (*approx.* 100 Mys) than those armoured within minerals. Sample EG10-BXX matrix monazites are not within error of garnet-hosted monazites and represent a gap in age of *ca.* 150 my. Due to the high temperatures experienced by the samples (*approx.* 900 °C), the metamorphic systems have the potential to remain open before cooling sufficiently to allow monazite Pb diffusion to ceaset. Matrix-hosted monazite grains may also be more susceptible to recrystallisation due grain boundary migration upon cooling (Cherniak *et al.* 2003).

Each sample presents discordia with lower intercepts in the range of 474 ± 230 Ma to 580 ± 320 Ma. These intercepts have large errors therefore are not definitive of later metamorphic reworking. Table 12 shows that there is some consistency, however, between lower intercepts and demonstrates that ages are within error of *ca.* 600 Ma. This correlates well with the age of a Pan African thermal overprint proposed by some authors associated with the collision of East and West Gondwana (e.g. Rai *et al.* 2009), which, especially when coupled with the uncertainties of modern lead loss (e.g. Cherniak *et al.* 2003) makes this a viable option for post-peak metamorphic ages in the Eastern Ghats Province.

Evidence of an earlier event

Some monazites also record $^{206}Pb/^{207}Pb$ ages older than peak metamorphism. Ages of 1.1 – 1.3 Ma may be evidence for an earlier, Grenvillian aged metamorphic event denoted as M_1. They may also signify the presence of inherited, detrital monazites, as sedimentation is suggested to have persisted until 1.35 Ga (Jarick 1999), but this is unusual in high temperature granulite terranes (e.g. Williams 2001). Peak upper-

intercepts show low correlation between samples. This could result from a smear of lower discordant ages skewing the apparent upper intercept.

Interpretation of P-T evolution

The construction of P-T pseudosections for four samples distributed spatially across the belt provides new constraints on *P-T* conditions of UHT metamorphism in the Eastern Ghats. Each sample also has corresponding age data, to enable the metamorphic evolution of the Eastern Ghats orogen to be interpreted in time and space. In the easternmost region of the Eastern Ghats Province, peak metamorphic assemblages define a steeply dipping fabric and peak metamorphic assemblages indicate pressure and temperature conditions of > 8.5 kbar and > 750 ºC and 12 kbar and 1000 – 1050 ºC for samples EG10-063 and EG10-AK5 respectively. The P-T path for sample EG10-063 cannot be defined. In contrast, the mineral assemblage and mineral composition of sample EG10-AK5 provides tight constraints on the *P-T* path. Sample EG10-AK5 describes some prograde metamorphism of isobaric heating recorded by the presence of early biotite inclusions in coarse-grained orthopyroxene and porphyroblastic garnet grains. Heating reached peak temperatures of 1000 – 1100 °C and peak pressures of 10.5 – 11.5 kbar. Peak pressures are superseded by retrograde near-isothermal decompression to temperatures of 870 – 950 °C and pressures of 3.5 – 5.5 kbar. This sample describes a metamorphic evolution in which a significant decrease of temperatures does not follow decompression or exhumation. The peak conditions are consistent with overall apparent high geothermal gradients recorded for the sample of *ca.* 30 °C/km (at peak) and *ca.* 50 °C/km (post-decompression). The metamorphic mineral assemblages, deformation and *P-T* path for these easternmost samples are interpreted to represent the regional M_2 event in the framework of previous studies (Mukhopadhyay & Basak 2009 and references therein) due to corresponding geochronological estimates.

As the spatial location across the belt changes so too does the metamorphic evolution recorded in the samples. Near the middle of the province sample EG10-BXX, an orthogneiss, also preserves UHT peak conditions based on the modelled mineral assemlage. This sample describes a metamorphic evolution from peak temperatures of 850 – 900 °C and pressures of 9.5 – 10.5 kbar corresponding to an apparent geothermal gradient of *ca.* 25 °C/km. This sample appears to have undergone near-isobaric cooling to

temperatures of 650 °C and pressures of 8 – 8.5 kbar, suggesting that rocks were buried at 25 – 30 km depth. Further west, sample EG10-136 preserves peak temperatures of 900 – 930 °C, and pressures of 9.5 – 10.5 kbar indicating a peak geothermal gradient of 30 – 35 °C/km and near-isobaric cooling. The *P-T* paths in the Province describe contradicting evolutions for the eastern and western parts of the province. The eastern portion is characterised by a clockwise *P-T* path with steep, near-isothermal retrograde *P-T* evolution, while the western samples record limited decompression/exhumation and likely anticlockwise *P-T* paths.

Inconsistencies in *P-T* paths could be a result of a trend in style of metamorphism across the belt, or be due to limitations in the analysis of *P-T* paths in high-grade and polymetamorphic terranes. Orogenic belts characterised by clockwise *P-T* paths in the east of the belt are associated with crustal thickening such as through collision, followed by erosional exhumation, extensional thinning or lithospheric delaminantion and orogenic collapse (Brown 1993). During clockwise metamorphism, melt is transferred from protolith rocks to the leucosomes through dehydration reactions. Crustal anatexis is particularly associated with high-temperature metamorphism that experiences decompression at high temperatures (Brown 1993). The production of melt can result in leucosomes formation in migmatites or, should the melt escape, granitic plutons such as those abundant in this study area can form contemporaneously with metamorphism (e.g. Schnetger 1994). Granite production is favoured in orogens that incorporate large quantities of fertile sedimentary rocks (Brown 2001) such as the Fe-Mg rich metapelites of the Eastern Ghats. Metamorphism can also be related to the advection of heat from a migrating magma that was produced by crustal anatexis in thickened continental crust. This can result in high-grade metamorphism at pluton contacts (DeYoreo *et al.* 1989), such as the anticlockwise metamorphism preserved in the west of the Eastern Ghats belt. In this region, younger, anticlockwise metamorphism is also accompanied by: a low-angle foliation compared to the high angle foliation pervasive across the rest of the belt, the possibility of two overprinting fabrics (preserved in sample EG10-118), and leucosomes that do not lie parallel to foliation compared to the upright foliation-defined region of the belt. Brown (2001) demonstrates that leucosomes developing as a result of contact metamorphism may lie non-parallel to compositional layering. Two fabrics could be due to metamorphism that is overprinting an earlier event. Alternatively, the metamorphic peak of *ca.* 925 Ma of

these samples could post-date the cessation of deformation, allowing melt to become discordant from the foliation as a result of dissipated stress.

There are alternative options to describe the inconsistent style of metamorphism that is evident across the Eastern Ghats. These revolve around the ambiguities in extracting *P-T* paths from high-grade and polymetamorphic terranes. In high grade terranes the generation of *P-T* paths depended largely on the interpretation of post-peak mineral textures, as high-temperature metamorphism can obliterate prograde mineral assembles (Kelsey *et al.* 2003b). The results are incomplete *P-T* paths with no prograde constraints. Retrograde reactions, however, can also be difficult to constrain. Granulite facies rocks often record only weak retrogression due to substantial melt loss. A paucity of retrogressive minerals can result in confusion when differentiating post peak regression reaction textures from unrelated partial metamorphic overprints (White & Powell 2002). Sample EG10-063, for example, not only contains a khondalite bulk composition that does not favour the generation of *P-T* diagnostic mineral assemblages (Kelsey *et al.* 2007) but it has also lost melt and contains no distinguishable retrograde minerals to define its *P-T* path. The loss of melt has other profound implications in disentangling one metamorphic episode from another. A high amount of melt loss from an earlier event will increase the solidus temperature of subsequent events so samples could record different metamorphic episodes depending on when and how much melt they have lost (White & Powell 2002).

Evidence for an earlier metamorphic event

There has been proposed to have been an earlier metamorphic event, M_1, to have affected the Eastern Ghats belt (Dobmeier and Raith 2007). The peak metamorphic assemblage of sample EG10-AK5 contains sapphirine inclusions within coarse grained garnet and orthopyroxene (Fig. 6k), which, at the same sample location, has been used as evidence by Dasgupta *et al.* (1994) for earlier M_1 UHT metamorphism. They interpret early sapphirine to be evidence for M_1 metamorphism. The pseudosection of sample EG10-AK5 does not directly account for sapphirine growth before orthopyroxene or garnet. As shown by Vernon (1996), however, inclusions and partial inclusions do not necessary indicate reactions. Instead, early sapphirine may be due to varying rates of nucleation between coexisting garnet – orthopyroxene and

sapphirine. This study therefore provides no definitive mineralogical evidence for an M_1 event, however it does demonstrate the value of coupled, rather than separated, geochronological and metamorphic interrogations.

Overall the *P-T* evolution of the Eastern Ghats may be summarised by two main scenarios. Firstly, that the Eastern Ghats has experienced a dominantly clockwise *P-T* metamorphic event consistent across the orogen. This is possible under the premises that varying *P-T* styles across the belt are mere segments of a more complete overall path. Inconsistent *P-T* paths could record segments of one, more complicated, *P-T* path because phase diagram *P-T* analysis was conducted on samples of differing bulk composition, which can preserve different *P-T* paths due to varying reaction kinetics of minerals (Kelsey *et al.* 2003a). The second option is that variations in the style of *P-T* evolution across the belt are as a result of varying tectonic development across the orogen. A combination of clockwise and anticlockwise *P-T* paths in one orogen is not unique (Brown 1993). Variations in P-T paths could also correspond to variations in exhumation experienced by samples (Schulmann *et al.* 2008). Isobaric cooling suggests that rapid exhumation was not a feature of the orogeny in the westernmost samples. In the east, the maintenance of high temperatures subsequent to decompression prescribes high geothermal gradients possibly related enhanced crustal heat flow. An understanding of the duration of metamorphism can constrain *P-T-t* paths and corroborate metamorphic evolutions of different samples. This will enable a more thorough grasp of the mechanisms allowing for varied *P-T* evolutions across the belt.

Duration of thermal event

In this study the equilibrium between coexisting garnet and biotite was used to assess diffusion rates of three samples across the Eastern Ghats Belt. The exchange of Fe and Mg between garnet and biotite has been used by a number of studies to determine cooling histories of metamorphic rocks because the diffusive chemical profiles that are produced in a mineral such as garnet depend specifically on the physical conditions constraining that minerals evolution (Robl *et al.* 2006).

If the Eastern Ghats experienced a polyphase deformation it would have experienced successive bouts of thermal influx, followed by independent cooling events. If the area followed a singular model of

deformation, the rocks would be heated to ultra-high temperatures and cooled just once. Cooling rates can thus help to derive tectonic scenarios and determine exhumation history of the region.

The zoning patterns of garnets and diffusion-modelled cooling rates have been correlated with results from phase diagram analysis as well as geochronology in this study to deduce that the Eastern Ghats underwent very slow cooling. Each of the three modelled samples are interpreted to preserve retrograde diffusional zoning profiles in garnet grains under the assumption that samples EG10-110 and EG10-087 were subjected to the pervasive UHT metamorphism recorded elsewhere across the belt (as they were not constrained through *P-T* phase diagram analysis). At high temperatures the rate of diffusion between iron and magnesium is fast, which can homogenise the garnet composition (Storm & Spear 2005). Consequently core-to-rim transects of pyrope, almandine, grossular and spessartine (Figs. 10 - 14) and of magnesium content (see garnet transects in Fig. 35) record retrograde cooling profiles.

The zoning profiles show gradual decrease in the magnesium content of garnet grains from the core to the rims, where the magnesium content decreases more rapidly. Although peak metamorphism is predicted to have reached > 900 °C in the Eastern Ghats Province, the cores of the analysed garnet grains do not record such extreme temperatures. Conventional garnet-biotite thermobarometric estimates show that temperatures recorded in the garnet cores range from 580 – 780 °C. Low core temperatures preserved in garnet cooling profiles suggest garnet grains were completely reset during cooling (Hauzenberger *et al.* 2005). Garnet grains can be reset during early, high temperature diffusion that results from volume diffusion. At lower temperatures, volume diffusion decreases and the retrograde rims in the garnet grains are produced. Smooth cooling profiles indicate that diffusion was the principle control on zoning rather than a complicated polyphase cooling/heating/cooling cycle of polymetamorphism (Hauzenberger *et al.* 2005). The zoning profiles measured in this study are inferred to preserve a record of slow cooling, where Fe-Mg exchange between garnet and biotite is enhanced (Hauzenberger *et al.* 2005). Garnet grain zoning profiles that result from slow cooling contrast to faster cooling profiles, which are often flat along the centre of the garnet with steep X_{Mg} slopes at the rims (Robl *et al.* 2007).

The calculated rates of cooling were found to be in the range of 0.05 – 5 °C/My. Based on the starting temperature of 900 °C and using temperatures recorded in garnet rims as the end temperature of garnet-

biotite diffusional cooling, it is apparent that rates below 1 °C/My are not geologically feasible (see Table 14). Should a cooling rate of 1 °C/My be applied to the metamorphic evolution of sample EG10-BXX, the duration of cooling experienced by the terrain is 330 million years. With an assumed metamorphic event at 940 Ma, this constrains the cessation of cooling to *ca.* 660 Ma. A cooling age of 660 Ma is within error of the lower intercept of all samples, and could provide evidence that smeared age data is a result of a prolonged duration above monazite closure temperatures.

Geologically infeasible cooling rates could be related to the assumptions in the diffusion modelling code by Robl *et al. (2007),* such as that the garnets are completely surrounded by a rim of biotite, that chemical equilibrium is solely binary and that the garnet has no zoning at peak temperature. The study could be strengthened also by testing the modelling of cooling rates based on different diffusional constants. A linear rate was used, however this is unlikely to be geologically realistic (Hauzenberger *et al.* 2005) and variable models may better suit the diffusional profiles.

Fernando *et al.* (2003) demonstrate that garnet and biotite grains were likely to have changed their compositions when diffusing between garnet cores and biotite to diffusing between garnet rims and biotite. They retrieve compositions of garnet and biotite phases at peak temperature and pressure using mass balance and equilibrium coefficient equations for Fe and Mg exchange, and a similar assumption was trialled in this study. The *apparent temperature* is considered the temperature that the garnet cores record using conventional thermobarometry and the *calculated temperature* is the temperature that garnets record with recovered peak temperature compositions. (Fernando *et al.* 2003) show that there was less magnesium in biotite at metamorphic peak before retrograde diffusion of the garnet. Garnet grains decrease in X_{Mg} from cores to rims, so follows that biotite grains in equilibrium with garnet cores would contain lower X_{Mg} than those in equilibrium with garnet rims. Using this assumption of lower X_{Mg} of biotite grains in equilibrium with cores, this study included cooling rate estimates using the X_{Mg} of biotite in equilibrium with rims of garnets, as well as an estimate of the X_{Mg} of biotite in equilibrium with garnet cores during peak metamorphism. To avoid geologically unjustifiable cooling rate estimates, estimations of recovered peak temperature X_{Mg} values for biotite were included in the calculation.

Another potential cause for geologically unreasonably low cooling rates could be because the samples contained garnet and biotite that were not growing within equilibrium with one another. Samples EG10-110 and EG10-087 are migmatites containing abundant leucosomes. Leucosomes are very anhydrous, comprising dominantly K-feldspar and quartz crystals. There is occasional evidence for retrogression and preservation of H_2O in the rocks, with distinct biotite selvedges separating anhydrous leucosomes from ferromagnesian-rich restite layers. While the occurrence of biotite grains in selvedges provides evidence that the biotite is a retrograde mineral (White and Powell 2010), garnet grains can be found in leucosomes and restite layers non-exclusively. It may be the case that an open system of melt migration has resulted in euhedral garnet merely accumulating in, but existing in chemical isolation from the melt and from retrograde reactions (Waters 1988; Kriegsman 2001; White & Powell 2002, 2010).

Although an exact cooling rate was unable to be applied in this study, it is apparent that slow cooling as opposed to fast cooling is the only model to fit the data produced by this study. Such cooling rates of 1 – 5 °C/My are advocated to be typical for extensive high grade terranes (Mezger *et al.* 1991) Sample EG10-BXX only experienced *approx.* 1 kbar of decompression but cooled for potentially as long as *ca.* 300 million years. These results resolve that the Eastern Ghats terrain was almost completely isostatically compensated following metamorphism and experienced prolonged crustal residence times. To further clarify residence time in the crust it would be useful to quantify the age of cooling, such as through direct age constraints on the rims of garnet, biotite closure temperature estimates, Ar-Ar dating of biotite or K-feldspar or more integrated geochronology and phase diagram forward modelling of retrograde assemblages in the belt.

Potential causative mechanisms leading to the development of a large hot orogen

To postulate a tectonic scenario capable of fulfilling the data produced for the Eastern Ghats belt through this study there are two dominant questions that need to be addressed. Firstly, what mechanism enables the production of enough heat for the crust to experience ultrahigh-temperatures on a regional scale? Secondly, what tectonic scenario supports collision-style deformation and the incubation of high temperatures within the crust, resisting decompression?

The generation of heat required for ultrahigh-metamorphism is a contentious topic. There still remains some problems in modelling UHT conditions in the crust at 35 – 50 km depth in collisional orogenesis (Kelsey 2008), and currently few accurate thermo-mechanical modelling has been able to replicate such conditions. In collisional orogenesis, crustal thickening could allow for self-heating of the thickened orogen (Brown, 2001), or an elevated thermal budget may be a result of the initial distribution of radioactive heat production in the crust (Jameison *et al*. 1998). The Eastern Ghats is known to be characterised by high levels of high-heat-producing elements such as U, Th and K (Kumar *et al.* 2008) and a particular enrichment in Th is associated with the study area (Barker 2010). Heat production levels shown in Table. 17 show particularly high heat production rates in Mg-Al granulites. Other, more transient, mechanisms to account for excess heat in continental orogenesis include internal heat generation, frictional heating along faults, lithospheric delamination, convective instability of the lower lithosphere, incident thermal plumes and viscous self-heating particularly of the sub-lithospherical mantle (Kincaid & Silver 1996 and references within). There is dispute, however, as to whether collisional processes have the capacity to generate enough heat for sufficient UHT metamorphism. An alternative proposal (Dasgupta & Sengupta 2003) is that the heat available for UHT metamorphism in the Eastern Ghats was related to mantle heat flow generated in a continental back-arc basin. Back-arc basins have Moho temperatures of 800 – 900 °C sufficient for UHT metamorphism (Hyndman 2005). Should this be the case, however, to generate the thickened crustal segment that currently comprises the Eastern Ghats (Subrahmanyam & Verma 1986), extension would have to be superseded by a mechanism of crustal thickening. There is also no evidence for a suture of significant mafic magmatism that could indicate the former presence of a back-arc basin.

The second major question to be addressed by this study concerns the long-durations of cooling experienced by the Eastern Ghats terrain. This study proposes that the Eastern Ghats represents a single long-duration orogenic event from *ca.* 975 Ma to *ca. 925* Ma, in agreement with Bhattacharya and Gupta (2002), but furthermore that the Eastern Ghats granulites comprise a large hot orogen. Large hot orogens are collisional orogens in which an abundance of heat gives rise to a highly viscous middle-crust enabling lateral, gravity-driven channel flow of the crust (see Fig. 37) (e.g. Beaumont, 2006). The classic example of a large hot orogen is the Himalayan-Tibetan orogen. Evidence supporting this large hot orogen model includes: (1) the

Eastern Ghats orogen is ~ 900 km long and > 300 km wide (2) it reached UHT metamorphic conditions implying that it was hot and (3) high temperatures were prolonged for as long as 300 million years. Prolonged heating in large hot orogens gives rise to an orogenic plateau beneath which the viscosity of the crust becomes sufficiently low to flow under gravitational or tectonic forcing (Rivers 2008). This aids lateral flow through the crust and inhibits the development of significant topography or exhumation (Beaumont *et al.* 2006), resulting in high-temperature granulites that remain incubated in a post-orogenic lower crust over a long durations (Brown 2006). The viscous channel often coincides with an area of elevated heat flow (Jamieson *et al.* 2002) and the lower crust of a LHO can exceed temperatures of 900 ºC (Jamieson *et al.* 2004) *P-T-t* paths are dominantly clockwise but different exhumation styles can have contrasting effects on channel flow (Jamieson *et al.* 2002) and variations in channel flow and exhumation style can also account for anticlockwise *P-T-t* paths and both vertical and horizontal structural fabrics (Schulmann *et al.* 2008).

CONCLUSIONS

1. The Eastern Ghats experienced a single metamorphic event at *ca.* 975 Ma within steeply-foliated metasediments of the east of the belt and at *ca.* 925 in shallow-foliated metasediments in the west of the belt.
2. The metamorphism likely to have been contemporaneous with extensive felsic magmatism that could be related to partial melting of the crust generated from ultrahigh-temperature metamorphism.
3. *P-T* paths vary in style depending on the spatial location across the belt with generalised near-isothermal decompression characterising eastmost samples and isobaric cooling in the west.
4. Cooling was very slow and occurred over long durations, with rates from *approx.* 1 – 5 ºC/My.
5. There is plausible, however not concrete, evidence for an earlier Grenvillian-ages event.
6. The most likely tectonic scenario for the Eastern Ghats is large hot collisional orogenesis involving lateral channel flow rather than mechanical thickening of the crust.

ACKNOWLEDGEMENTS

I would like to thank my supervisors Martin Hand and Dave Kelsey. I would also like to thank Justin Payne and Kathryn Cutts, who both demonstrated considerable patience and support through this project. The staff at Adelaide Microscopy deserve particular gratitude, especially Angus Netting and Ben Wade, for answering their phones at all hours of the morning. For their help and expertise I would like to acknowledge Chris Clark and Richard Taylor at Curtin University, Western Australia. I was also lucky enough to spend time in the field with Saibal Gupta and Anando Modak, from the Indian Institute of Technology, Kharagapur, India and I thank them for their help in the field. Thanks also go to Adelaide University and all of the other honours students who made the year truly memorable.

REFERENCE LIST

BATT G. E. & BRAUN J. 1999. The tectonic evolution of the Southern Alps, New Zealand: Insights from fully thermally coupled dynamical modelling. *Geophysical Journal International* **136**, 403-420.

BARKER A. 2010. The thermal properties, temperature structure and thermal evolution of the Eastern Ghats, India. *Honours Thesis.* Adelaide University.

BEAUMONT C., NGUYEN M. H., JAMEISON R. A. & ELLIS S. 2006. Crustal flows in large hot orogens *(eds) Channel Flow, Ductile Extrusion and Exhumation in Continental Collision Zones. Geological Society, London, Special Publications.* **268**, 91-145.

BHATTACHARYA & KAR 2002. High-temperature dehydration melting and decompressive P-T path in a granulite complex from the Eastern Ghats, India. *Contributions to Mineralogy and Petrology* **143**, 175-191.

BHATTACHARYA A. & GUPTA S. 2001. A reappraisal of polymetamorphism in the Eastern Ghats belt — A view from north of the Godavari rift. *Journal of Earth System Science* **110**, 369-383.

BHATTACHARYA S. 1997. Evolution of Eastern Ghats granulite belt of India in a compressional tectonic regime and juxtaposition against Iron Ore Craton of Singhbhum by oblique collision — transpression. *Journal of Earth System Science* **106**, 65-75.

BHATTACHARYA S., KAR R., MISRA S. & TEIXEIRA W. 2001. Early Archaean continental crust in the Eastern Ghats granulite belt, India: isotopic evidence from a charnockite suite. *Geological Magazine* **138**, 609-618.

BHATTACHARYA S., SEN S. K. & ACHARYYA A. 1994. The structural setting of the Chilka Lake granulite-migmatite-anorthosite suite with emphasis on the time relation of charnockites. *Precambrian Research* **66**, 393-409.

BHOWMIK S. K., DASGUPTA S., HOERNES S. & BHATTACHARYA P. K. 1995. Extremely high-temperature calcareous granulites from the Eastern Ghats, India; evidence for isobaric cooling, fluid buffering, and terminal channelized fluid flow. *Eur J Mineral* **7**, 689-703.

BOSE, FUKUOKA, SENGUPTA & DASGUPTA 2000. Evolution of high-Mg–Al granulites from Sunkarametta, Eastern Ghats, India: evidence for a lower crustal heating–cooling trajectory. *Journal of Metamorphic Geology* **18**, 223-240.

BROWN M. 1993. P-T-t evolution of orogenic belts and the causes of regional metamorphism. *Journal - Geological Society (London)* **150**, 227-241.

BROWN M. 2001. Orogeny, migmatites and leucogranites: A review. *Proceedings of the Indian Academy of Sciences, Earth and Planetary Sciences* **110**, 313-336.

BROWN M. 2006. Duality of thermal regimes is the distinctive characteristic of plate tectonics since the Neoarchean. *Geology* **34**, 961-964.

BROWN M. 2007. Metamorphic Conditions in Orogenic Belts: A Record of Secular Change. *International Geology Review* **49**, 193 - 234.

CATLOS E. J., GILLEY L. D. & HARRISON T. M. 2002. Interpretation of monazite ages obtained via in situ analysis. *Chemical Geology* **188**, 193-215.

CHARDON D., GAPAIS D. & CAGNARD F. 2009. Flow of ultra-hot orogens: A view from the Precambrian, clues for the Phanerozoic. *Tectonophysics* **477**, 105-118.

CHERNIAK D. J., WATSON E. B., GROVE M. & HARRISON T. M. 2004. Pb diffusion in monazite: a combined RBS/SIMS study. *Geochimica et Cosmochimica Acta* **68**, 829-840.

CHETTY T. & MURTHY D. 1994. Collision tectonics in the late Precambrian Eastern Ghats Mobile Belt: mesoscopic to satellite-scale structural observations. *Terra Nova* **6**, 72-81.

CROWE W. A., NASH C. R., HARRIS L. B., LEEMING P. M. & RANKIN L. R. 2003. The geology of the Rengali Province: Implications for the tectonic development of northern Orissa, India. *Journal of Asian Earth Sciences* **21**, 697-710.

DAS K., BOSE S., OHNISHI I. & DASGUPTA S. 2006. Garnet-spinel intergrowths in ultrahigh-temperature granulite, Eastern Ghats, India: Possible evidence of an early Tschermak-rich orthopyroxene during prograde metamorphism. *American Mineralogist* **91**, 375-384.

DASGUPTA S. 1993. Contrasting mineral parageneses in high-temperature calc-silicate granulites: examples from the Eastern Ghats, India. *Journal of Metamorphic Geology* **11**, 193-202.

DASGUPTA S., SANYAL S., SENGUPTA P. & FUKUOKA M. 1994. Petrology of Granulites from Anakapalle—Evidence for Proterozoic Decompression in the Eastern Ghats, India. *Journal of Petrology* **35**, 433-459.

DASGUPTA S. & SENGUPTA P. 2003. Indo-Antarctic Correlation: a perspective from the Eastern Ghats Granulite Belt, India. *Geological Society, London, Special Publications* **206**, 131-143.

DASGUPTA S., SENGUPTA P., EHL J., RAITH M. & BARDHAN S. 1995. Reaction Textures in a Suite of Spinel Granulites from the Eastern Ghats Belt, India: Evidence for Polymetamorphism, a Partial Petrogenetic Grid in the System KFMASH and the Roles of ZnO and Fe2O3. *Journal of Petrology* **36**, 435-461.

DASGUPTA S., SENGUPTA P., FUKUOKA M. & BHATTACHARYA P. K. 1991. Mafic Granulites from the Eastern Ghats, India: Further Evidence for Extremely High Temperature Crustal Metamorphism. *The Journal of Geology* **99**, 124-133.

DASGUPTA S., SENGUPTA P., FUKUOKA M. & CHAKRABORTI S. 1992. Dehydration melting, fluid buffering and decompressional P–T path in a granulite complex from the Eastern Ghats, India. *Journal of Metamorphic Geology* **10**, 777-788.

DOBMEIER C. J. & RAITH M. M. 2003. Crustal architecture and evolution of the Eastern Ghats Belt and adjacent regions of India. *Geological Society, London, Special Publications* **206**, 145-168.

E. VAN ACHTERBERGH C. R., SE JACKSON, WL GRIFFIN 2001. Data reduction software for LA-ICP-MS.

FERNANDO G. W. A. R., HAUZENBERGER C. A., BAUMGARTNER L. P. & HOFMEISTER W. 2003. Modeling of retrograde diffusion zoning in garnet: evidence for slow cooling of granulites from the Highland Complex of Sri Lanka. *Mineralogy and Petrology* **78**, 53-71.

FITZSIMONS I. C. W., KINNY P. D., WETHERLEY S. & HOLLINGSWORTH D. A. 2005. Bulk chemical control on metamorphic monazite growth in pelitic schists and implications for U–Pb age data. *Journal of Metamorphic Geology* **23**, 261-277.

FOSTER G., KINNY P., VANCE D., PRINCE C. & HARRIS N. 2000. The significance of monazite U-Th-Pb age data in metamorphic assemblages; a combined study of monazite and garnet chronometry. *Earth and Planetary Science Letters* **181**, 327-340.

FRITZ H., TENCZER V., HAUZENBERGER C., WALLBRECHER E. & MUHONGO S. 2009. Hot granulite nappes - Tectonic styles and thermal evolution of the Proterozoic granulite belts in East Africa. *Tectonophysics* **477**, 160-173.

GREW E. S. & MANTON W. I. 1986. A new correlation of sapphirine granulites in the indo-antarctic metamorphic terrain: Late proterozoic dates from the eastern ghats province of India. *Precambrian Research* **33**, 123-137.

GUPTA S., BHATTACHARYA A., RAITH M. & NANDA J. 2000. Contrasting pressure–temperature–deformation history across a vestigial craton–mobile belt boundary: the western margin of the Eastern Ghats Belt at Deobhog, India. *Journal of Metamorphic Geology* **18**, 683-697.

HARLEY S. L. 2008. Refining the P–T records of UHT crustal metamorphism. *Journal of Metamorphic Geology* **26**, 125-154.

HARRISON T. M., CATLOS E. J. & MONTEL J.-M. 2002. U-Th-Pb Dating of Phosphate Minerals. *Reviews in Mineralogy and Geochemistry* **48**, 524-558.

HARVEY C. 2010. Architecture and evolution of the central Eastern Ghats province: Araku-Paderu-Visakhapatnam. *Honours Thesis.* Adelaide University.

HAUZENBERGER C. A., ROBL J. & STUWE K. 2005. Garnet zoning in high pressure granulite-facies metapelites, Mozambique belt, SE-Kenya: constraints on the cooling history. *Eur J Mineral* **17**, 43-55.

JAMIESON R. A., BEAUMONT C., MEDVEDEV S. & NGUYEN M. H. 2004. Crustal channel flows: 2. Numerical models with implications for metamorphism in the Himalayan-Tibetan orogen. *J. Geophys. Res.* **109**, B06407.

JAMIESON R. A., BEAUMONT C., NGUYEN M. H. & LEE B. 2002. Interaction of metamorphism, deformation and exhumation in large convergent orogens. *Journal of Metamorphic Geology* **20**, 9-24.

JARICK J. 1999. Die thermotektonometamorphe Entwicklung des Eastern Ghats Belt, Indien - ein Test der SWEAT-Hypothese. . *PhD Thesis, Johann Wolfgang Geothe Universitaet, Frankfurt am Main, Germany*.

KAMINENI D. C. & RAO A. T. 1988. Sapphirine-Bearing Quartzite from the Eastern Ghats Granulite Terrain, Vizianagaram, India. *The Journal of Geology* **96**, 209-220.

KELLY N. M., CLARKE G. L. & HARLEY S. L. 2006. Monazite behaviour and age significance in poly-metamorphic high-grade terrains: A case study from the western Musgrave Block, central Australia¹1Abbreviations: After Kretz, 1983. *Lithos* **88**, 100-134.

KELSEY, D.E., SMITHIES, R.H., HAND, M., EVINS, P.M., CLARK, C., KIRKLAND, C. What is the tectonic setting of long-lived Grenvillian-aged ultrahigh temperature, high geothermal gradient metamorphism in the Musgrave Province, central Australia? Geological Society of America Abstracts with Programs, 42(5), Denver, Colorado, Oct-Nov 2010.

KELSEY D. E. 2008. On ultrahigh-temperature crustal metamorphism. *Gondwana Research* **13**, 1-29.

KELSEY D. E., CLARK C. & HAND M. 2008. Thermobarometric modelling of zircon and monazite growth in melt-bearing systems: examples using model metapelitic and metapsammitic granulites. *Journal of Metamorphic Geology* **26**, 199-212.

KELSEY D. E., HAND M., CLARK C. & WILSON C. J. L. 2007. On the application of in situ monazite chemical geochronology to constraining P-T-t histories in high-temperature (>850 {degrees}C) polymetamorphic granulites from Prydz Bay, East Antarctica. *Journal of the Geological Society* **164**, 667-683.

KELSEY D. E., WHITE R. W. & POWELL R. 2003a. Orthopyroxene–sillimanite–quartz assemblages: distribution, petrology, quantitative P–T–X constraints and P–T paths. *Journal of Metamorphic Geology* **21**, 439-453.

KELSEY D. E., WHITE R. W., POWELL R., WILSON C. J. L. & QUINN C. D. 2003b. New constraints on metamorphism in the Rauer Group, Prydz Bay, east Antarctica. *Journal of Metamorphic Geology* **21**, 739-759.

KINCAID C. & SILVER P. 1996. The role of viscous dissipation in the orogenic process. *Earth and Planetary Science Letters* **142**, 271-288.

KRAUSE O., DOBMEIER C., RAITH M. M. & MEZGER K. 2001. Age of emplacement of massif-type anorthosites in the Eastern Ghats Belt, India: constraints from U-Pb zircon dating and structural studies. *Precambrian Research* **109**, 25-38.

KRIEGSMAN L. M. 2001. Partial melting, partial melt extraction and partial back reaction in anatectic migmatites. *Lithos* **56**, 75-96.

LAL R. K., ACKERMAND D. & UPADHYAY H. 1987. P-T-X Relationships Deduced from Corona Textures in Sapphirine—Spinel—Quartz Assemblages from Paderu, Southern India. *Journal of Petrology* **28**, 1139-1168.

MEZGER K. & COSCA M. A. 1999. The thermal history of the Eastern Ghats Belt (India) as revealed by U-Pb and 40Ar/39Ar dating of metamorphic and magmatic minerals: implications for the SWEAT correlation. *Precambrian Research* **94**, 251-271.

MEZGER K., RAWNSLEY C. M., BOHLEN S. R. & HANSON G. N. 1991. U-Pb Garnet, Sphene, Monazite, and Rutile Ages: Implications for the Duration of High-Grade Metamorphism and Cooling Histories, Adirondack Mts., New York. *The Journal of Geology* **99**, 415-428.

MOHAN A., TRIPATHI P. & MOTOYOSHI Y. 1997. Reaction history of sapphirine granulites and a decompressional P-T path in a granulite complex from the Eastern Ghats. *Journal of Earth System Science* **106**, 115-129.

MUKHERJEE A. 1989. P-T-time history and thermal modelling of an anorthosite-granulite interface, Eastern Ghats metamorphic belt, India. *Geological Society, London, Special Publications* **43**, 265-274.

MUKHOPADHYAY A. K. & BHATTACHRYA A. 1997. Tectonothermal evolution of the gneiss complex at Salur in the Eastern Ghats Grnaulite Belt of India. *Journal of Metamorphic Geology* **15**, 719-734.

MUKHOPADHYAY D. & BASAK K. 2009. The Eastern Ghats Belt … A polycyclic granulite terrain. *Journal of the Geological Society of India* **73**, 489-518.

NANDA J., GUPTA S. & DOBMEIER C. J. 2008. Metamorphism of the Koraput Alkaline Complex, Eastern Ghats Province, India--Evidence for reworking of a granulite terrane. *Precambrian Research* **165**, 153-168.

PAUL D. K., BARMAN T. R., MCNAUGHTON N. J., FLETCHER I. R., POTTS P. J., RAMAKRISHNAN M. & AUGUSTINE P. F. 1990. Archean-Proterozoic Evolution of Indian Charnockites: Isotopic and Geochemical Evidence from Granulites of the Eastern Ghats Belt. *The Journal of Geology* **98**, 253-263.

PAYNE J. L., FERRIS G., BAROVICH K. M. & HAND M. 2010. Pitfalls of classifying ancient magmatic suites with tectonic discrimination diagrams: An example from the Paleoproterozoic Tunkillia Suite, southern Australia. *Precambrian Research* **177**, 227-240.

PAYNE J. L., HAND M., BAROVICH K. M. & WADE B. P. 2008. Temporal constraints on the timing of high-grade metamorphism in the northern Gawler Craton: implications for assembly of the Australian Proterozoic. *Australian Journal of Earth Sciences: An International Geoscience Journal of the Geological Society of Australia* **55**, 623 - 640.

POWELL R., HOLLAND T. & WORLEY B. 1998. Calculating phase diagrams involving solid solutions via non-linear equations, with examples using THERMOCALC. *Journal of Metamorphic Geology* **16**, 577-588.

PYLE J. M. & SPEAR F. S. 2000. An empirical garnet (YAG) – xenotime thermometer. *Contributions to Mineralogy and Petrology* **138**, 51-58.

PYLE J. M. & SPEAR F. S. 2003. Yttrium zoning in garnet: Coupling of major and accessory phases during metamorphic reactions. *American Mineralogist* **88**, 708-.

RAI A., GAUR V. K., RAI S. S. & PRIESTLEY K. 2009. Seismic signatures of the Pan-African orogeny: Implications for southern Indian high-grade terranes. *Geophysical Journal International* **176**, 518-528.

RICKERS K., RAITH M. & DASGUPTA S. 2001. Multistage reaction textures in xenolithic high-MgAl granulites at Anakapalle, Eastern Ghats Belt, India: examples of contact polymetamorphism and infiltration-driven metasomatism. *Journal of Metamorphic Geology* **19**, 563-582.

RIVERS T. 2008. Assembly and preservation of lower, mid, and upper orogenic crust in the Grenville Province--Implications for the evolution of large hot long-duration orogens. *Precambrian Research* **167**, 237-259.

ROBL J., HERGARTEN S., STÜWE K. & HAUZENBERGER C. 2007. THERMAL HISTORY: A new software to interpret diffusive zoning profiles in garnet. *Computers & Geosciences* **33**, 760-772.

RUBATTO D., WILLIAMS I. S. & BUICK I. S. 2001. Zircon and monazite response to prograde metamorphism in the Reynolds Range, central Australia. *Contributions to Mineralogy and Petrology* **140**, 458-468.

SARKAR A., BHANUMATHI L. & BALASUBRAHMANYAN M. N. 1981. Petrology, geochemistry and geochronology of the Chilka Lake igneous complex, Orissa state, India. *Lithos* **14**, 93-111.

SCHNETGER B. 1994. Partial melting during the evolution of the amphibolite- to granulite-facies gneisses of the Ivrea Zone, northern Italy. *Chemical Geology* **113**, 71-101.

SCHULMANN K., LEXA O., ŠTÍPSKÁ P., RACEK M., TAJČMANOVÁ L., KONOPÁSEK J., EDEL J. B., PESCHLER A. & LEHMANN J. 2008. Vertical extrusion and horizontal channel flow of orogenic

lower crust: key exhumation mechanisms in large hot orogens? *Journal of Metamorphic Geology* **26**, 273-297.

SEN S. & BHATTACHARYA S. 1997. Dehydration melting of micas in the Chilka Lake Khondalites: The link between the metapelites and granitoids. *Journal of Earth System Science* **106**, 277-297.

SEN S. K., BHATTACHARYA S. & ACHARYYA A. 1995. A multi-stage pressure—temperature record in the Chilka Lake granulites: the epitome of the metamorphic evolution of Eastern Ghats, India? *Journal of Metamorphic Geology* **13**, 287-298.

SENGUPTA P., DASGUPTA S., BHATTACHARYA P. K., FUKUOKA M., CHAKRABORTI S. & BHOWMICK S. 1990. Petro-tectonic Imprints in the Sapphirine Granulites from Anantagiri, Eastern Ghats Mobile Belt, India. *Journal of Petrology* **31**, 971-996.

SENGUPTA P., KARMAKAR S., DASGUPTA S. & FUKUOKA M. 1991. Petrology of spinel granulites from Araku, Eastern Ghats, India, and a petrogenetic grid for sapphirine-free rocks in the system FMAS. *Journal of Metamorphic Geology* **9**, 451-459.

SENGUPTA P., SANYAL S., DASGUPTA S., FUKUOKA M. & EHL J. 1997. Controls of mineral reactions in high-grade garnet-wollastonite-scapolite-bearing calcsilicate rocks: an example from Anakapalle, Eastern Ghats, India. *Journal of Metamorphic Geology* **15**, 551-564.

SENGUPTA P., SEN J., DASGUPTA S., RAITH M., BHUI U. K. & EHL J. 1999. Ultra-high Temperature Metamorphism of Metapelitic Granulites from Kondapalle, Eastern Ghats Belt: Implications for the Indo-Antarctic Correlation. *Journal of Petrology* **40**, 1065-1087.

SHAW R. K. & ARIMA M. 1996. High-temperature metamorphic imprint on calc-silicate granulites of Rayagada, Eastern Ghats, India: implication for the isobaric cooling path. *Contributions to Mineralogy and Petrology* **126**, 169-180.

SHAW R. K., ARIMA M., KAGAMI H., FANNING C. M., SHIRAISHI K. & MOTOYOSHI Y. 1997. Proterozoic events in the Eastern Ghats Granulite Belt, India: Evidence from Rb-Sr, Sm-Nd systematics, and SHRIMP dating. *Journal of Geology* **105**, 645-656.

SIMMAT R. & RAITH M. M. 2008. U-Th-Pb monazite geochronometry of the Eastern Ghats Belt, India: Timing and spatial disposition of poly-metamorphism. *Precambrian Research* **162**, 16-39.

SMITH H. A. & BARREIRO B. 1990. Monazite U-Pb dating of staurolite grade metamorphism in pelitic schists. *Contributions to Mineralogy and Petrology* **105**, 602-615.

SPEAR F. S. & PYLE J. M. 2002. Apatite, Monazite, and Xenotime in Metamorphic Rocks. *Reviews in Mineralogy and Geochemistry* **48**, 293-335.

STORM L. C. & SPEAR F. S. 2005. Pressure, temperature and cooling rates of granulite facies migmatitic pelites from the southern Adirondack Highlands, New York. *Journal of Metamorphic Geology* **23**, 107-130.

SUBRAHMANYAM C. & VERMA R. K. 1986. Gravity field, structure and tectonics of the Eastern Ghats. *Tectonophysics* **126**, 195-212.

VERNON R. H. 1996. Problems with inferring P–T–t paths in low-P granulite facies rocks. *Journal of Metamorphic Geology* **14**, 143-153.

WATERS D. 1988. Partial melting and the formation of granulite facies assemblages in Namaqualand, South Africa. *Journal of Metamorphic Geology* **6**, 387-404.

WHITE R. W. & POWELL R. 2002. Melt loss and the preservation of granulite facies mineral assemblages. *Journal of Metamorphic Geology* **20**, 621-632.

WHITE R. W. & POWELL R. 2010. Retrograde melt–residue interaction and the formation of near-anhydrous leucosomes in migmatites. *Journal of Metamorphic Geology* **28**, 579-597.

WHITE R. W., POWELL R. & HOLLAND T. J. B. 2007. Progress relating to calculation of partial melting equilibria for metapelites. *Journal of Metamorphic Geology* **25**, 511-527.

WILLIAMS I. S. 2001. Response of detrital zircon and monazite, and their U–Pb isotopic systems, to regional metamorphism and host-rock partial melting, Cooma Complex, southeastern Australia*. *Australian Journal of Earth Sciences* **48**, 557-580.

FIGURE CAPTIONS

1. Representative geological map of south-eastern India adapted from Dobmeier and Raith (2003).

2. Geological map of the sample region, also known as the Eastern Ghats Province (Dobmeier & Raith 2003). White dashed lines represent lithological subdivisions from Ramakrishnan *et al.* (1998), as labelled as Zones 1 – 4 on the figure. This figure was adapted from the 1993 geological map of India published by the Geological Survey of India. Lineations and foliations measured during field work are denoted on the figure as well as the sample localities.
3. *P-T* trajectories from various locations across the belt, compiled by Mukhopadhyay and Basak (2009). The red square corresponds to the sample area of this study.
4. Geochronological data compiled from Simmat and Raith (2008), Jarick (1999), Crowe (2003), Shaw *et al.* (1997), Paul *et al.* (1990) and Grew and Manton (1986).
5. Photographs of field structures in the Eastern Ghats Province: (a) shows a khondalite sample from the central belt with melt-parallel foliations (b) leucosomes are garnet-rich and contain Fe-Mg rich selvedges (c) khondalites within upright foliation in the east of the belt contain asymmetrical and symmetrical folding (d) in the west of the belt, melt cross-cuts foliation (e) L-tectonite orthogneisses contain a lineation defined by aligned K-feldspar megacryst grains. They also contain rafts of foliated metasediments (f) rafts of metasediments are folded within orthogneiss.
6. Petrological images taken with a transmitted-light microscope. (a) and (b) are sample EG10-063 (c) – (f) Sample EG10-AK3, (g) – (k) EG10-AK5, (l) – (n) sample EG10-118, (o) – (s) sample EG10-136, (t) – (u) sample EG10-BXX, (v) sample EG10-087, (w) and (x) sample EG10-110.
7. Compositional maps from sample EG10-AK5. (a) Garnet in the top of each image and orthopyroxene grain is in the bottom left. Sapphirine + plagioclase + cordierite symplectites comprise the rest of the image. (b) This mineral texture is orthopyroxene rimming a sapphirine + sillimanite + cordierite intergrowth. The mineral composition is suggested to possibly represent a relict osumilite mineral.
8. Compositional maps of mineral textures from sample EG10-AK3. The large mineral in the bottom right of the image is orthopyroxene and the large mineral in the top right is garnet. Symplectite intergrowths of orthopyroxene + sapphirine + cordierite + plagioclase surround these grains.

9. Compositional maps of Sample EG10-118, showing the two foliations preserved in the sample. This texture describes complex garnet + sillimanite + corundum intergrowths and is surrounded by a matrix of quartz and feldspar.
10. Compositional maps of garnet grain (1) from sample EG10-BXX, showing a representative transect across the garnet displaying end-member compositions. X(alm) = Fe/(Fe + Mg + Mn + Ca), X(py) = Mg/(Fe + Mg + Mn + Ca), X(grs) = Ca/(Fe + Mg + Mn + Ca), X(spss) = Fe + Mg + Mn + Ca.
11. Compositional map of garnet grain (2) from sample EG10-BXX, showing a representative transect across the garnet displaying end-member compositions. X(alm) = Fe/(Fe + Mg + Mn + Ca), X(py) = Mg/(Fe + Mg + Mn + Ca), X(grs) = Ca/(Fe + Mg + Mn + Ca), X(spss) = Fe + Mg + Mn + Ca.
12. Compositional map of a garnet grain from sample EG10-087, showing representative transects across the garnet displaying end-member compositions. X(alm) = Fe/(Fe + Mg + Mn + Ca), X(py) = Mg/(Fe + Mg + Mn + Ca), X(grs) = Ca/(Fe + Mg + Mn + Ca), X(spss) = Fe + Mg + Mn + Ca.
13. Compositional map of garnet grain (a) from sample EG10-110, showing a representative transect across the garnet displaying end-member compositions. X(alm) = Fe/(Fe + Mg + Mn + Ca), X(py) = Mg/(Fe + Mg + Mn + Ca), X(grs) = Ca/(Fe + Mg + Mn + Ca), X(spss) = Fe + Mg + Mn + Ca.
14. Compositional map of garnet grain (c) from sample EG10-110. (a) shows a representative transect across the garnet displaying end-member compositions (b) shows a garnet transect across another garnet (b) from the same sample. X(alm) = Fe/(Fe + Mg + Mn + Ca), X(py) = Mg/(Fe + Mg + Mn + Ca), X(grs) = Ca/(Fe + Mg + Mn + Ca), X(spss) = Fe + Mg + Mn + Ca.
15. Compositional transect across a garnet grain from sample EG10-AK5. X(alm) = Fe/(Fe + Mg + Mn + Ca), X(py) = Mg/(Fe + Mg + Mn + Ca), X(grs) = Ca/(Fe + Mg + Mn + Ca), X(spss) = Fe + Mg + Mn + Ca.
16. Transects across orthopyroxene grains from sample EG10-AK5. (a) – (e) show orthopyroxene$_1$ (see mineral chemistry), showing trend from feldspar grains to diamond-shaped sapphirine + sillimanite + cordierite intergrowth. (f) shows a transect across orthopyroxene$_2$ showing varying y(opx) values corresponding to rim and core analyses.

17. Plots of sapphirine compositions in four samples depending on number of aluminium and silicon cations.
18. Shows a feldspar transect across a grain in sample EG10-AK5 showing increased orthoclase at the core compared to plagioclase compositions at the rims.
19. (a) Ternary diagram representing feldspar compositions in various samples (b) ternary diagram representing feldspar compositions in sample EG10-136.
20. Calculated *P-T* pseudosection for sample EG10-063. The white circle indicates the estimate of peak pressure and temperature conditions.
21. (a) Calculated *P-T* pseudosection for sample EG10-AK5 (b) The same pseudosection as (a) contoured for the aluminium content of orthopyroxene. The arrow displays the interpreted evolution of the sample in *P-T* space.
22. Calculated *P-T* pseudosection for sample EG10-BXX.
23. The same pseudosection as Fig. 22 contoured for x(g) [Fe/(Fe + Mg)], y(opx) [Si + Al] and z(g) [Ca/(Ca + Fe + Mg)]. The circles represent the compositions of A. The peak mineral assemblage B. The garnet core composition and C. the garnet rim composition as defined by the mineral chemistry of the sample. Arrows denote the inferred evolution of the sample in *P-T* space.
24. A calculated *P-T* pseudosection of sample EG10-136. This includes a zoomed in view of the pseudosection from 895 – 935 °C and 7.8 – 9.6 kbar.
25. The sample calculated *P-T* pseudosection as Fig. 24. (a) shows contours for x(g) [Fe/(Fe + Mg)], y(opx) [Si + Al] and z(g) [Ca/(Ca + Fe + Mg)], ca(pl) [Ca/(Ca + Na + K)], x(sp) [Fe/(Fe + Mg)], x(sa) [Fe/(Fe + Mg)]. The circle presents the earliest assemblage recorded in the rock. The dotted lines represent a proposed prograde *P-T* path and the solid arrow is the inferred peak and retrograde *P-T* path experienced by the sample. (b) The *P-T* pseudosection is contoured for model proportions of spinel (sp), corundum (crn), and sapphirine (sa).
26. (a) Concordia plot of all monazite analyses for sample EG10-063. Intercept ages are in Table 12. (b) $^{206}Pb/^{207}Pb$ weighted average plot of sample EG10-063. (c) compositional maps of monazite 34 and

spots 5.1, 5.2, 5.3, 5.4 and measured $^{206}Pb/^{207}Pb$ age. (d) compositional maps of monazite 32 and $^{206}Pb/^{207}Pb$ ages of spots 1.1 and 1.2 (e) Compositional maps of monazite 36 and $^{206}Pb/^{207}Pb$ age of spot 7.1.

27. Sample EG10-AK3 monazite series: (a) A representative monazite grain containing characteristic zoning of 'Series 1' monazite grains. Compositional maps are of monazite 21 and $^{206}Pb/^{207}Pb$ ages of spots 8.1, 8.2, 8.3 and 8.4 (b) a representative monazite grain containing characteristic zoning of 'Series 2' monazite grains. Compositional maps are of monazite 24 and $^{206}Pb/^{207}Pb$ ages of spots 9.1, 9.2, 9.3 and 9.4 (c) a representative monazite containing characteristic zoning of 'Series 3' monazite grains. Compositional maps are of monazite 23 and $^{206}Pb/^{207}Pb$ ages of spot 6.1 (d) a representative monazite containing characteristic zoning of 'Series 4' monazite grains. Compositional maps are of monazites 20 and $^{206}Pb/^{207}Pb$ ages of spots 2.1, 2.2, 3.1 and 4.1 (e) Weighted average $^{206}Pb/^{207}Pb$ age of spots on the innermost Y-rich core as seen in *series 1* monazite grains (f) Weighted average $^{206}Pb/^{207}Pb$ age of spots on the Y-poor rim, that rims the innermost Y-rich core as seen in *series 1 and 2* monazite grains (g) Weighted average $^{206}Pb/^{207}Pb$ age of spots on the outermost Y-rich rim as seen in *series 1, 2 and 3* monazite grains.
28. (a) Concordia plot of all monazite analyses for sample EG10-AK3. Intercept ages are in Table 12 (b) $^{206}Pb/^{207}Pb$ weighted average plot of sample EG10-AK3
29. (a) Concordia plot of all monazite analyses for sample EG10-AK5. Intercept ages are in Table 12 (b) $^{206}Pb/^{207}Pb$ weighted average plot of sample EG10-AK5 (c) Concordia plot sample EG10-AK5 monazite grains situated within orthopyroxene, garnet or feldspar grains (d) $^{206}Pb/^{207}Pb$ weighted average plot of sample EG10-AK5 situated within orthopyroxene, garnet or feldspar grains (e) 'Older population' representative monazite BSE images showing spots 25a, 25b, 33a, 35a, 40a and 40b (f) Concordia plot sample EG10-AK5 analyses of monazite grains situated within symplectite mineral textures in sample EG10-AK5 (g) $^{206}Pb/^{207}Pb$ weighted average plot of analyses of monazite grains situated within symplectite mineral textures in sample EG10-AK5 (h) 'Younger population' representative monazite BSE images showing spots 16a, 23a, 24a, 24b, 24c, 24d and

51a (h) a frequency histogram of all $^{206}Pb/^{207}Pb$ ages analysed on monazites in sample EG10-AK5 (i) a BSE image of a thin section from sample EG10-AK5 showing distribution of ages depending on textural location in the sample. Red boxes are around monazite grains corresponding to 'older population' analyses. Yellow boxes are around monazite grains corresponding to 'younger population' analyses. All ages are $^{206}Pb/^{207}Pb$ average ages.

30. (a) Concordia plot of all monazite analyses for sample EG10-BXX. Intercept ages are in Table 12 (b) $^{206}Pb/^{207}Pb$ weighted average plot of all analyses in sample EG10-BXX. (c) monazite grain 16 from within the matrix of the sample and $^{206}Pb/^{207}$ age of spot 16a (d) monazite grain 10 from within the matrix of the sample and $^{206}Pb/^{207}$ age of spot 10a (e) monazite grain 20 from within a garnet grain and $^{206}Pb/^{207}$ age of spots 20a, 20d and 20e (f) monazite grain 19 from within a garnet grain in the sample and $^{206}Pb/^{207}$ age of spot 19a (g) concordia plot of analyses on monazite grains located within garnet grains for sample EG10-BXX (h) $^{206}Pb/^{207}Pb$ weighted average plot of analyses on monazite grains located within garnet grains for sample EG10-BXX (i) concordia plot of analyses on monazite grains located within the matrix of sample EG10-BXX (j) $^{206}Pb/^{207}Pb$ weighted average plot of analyses on monazite grains located within the matrix of sample EG10-BXX.
31. (a) Concordia plot of all monazite analyses for sample EG10-087. Intercept ages are in Table 12 (b) $^{206}Pb/^{207}Pb$ weighted average plot of all analyses in sample EG10-087 (c) Representative monazite BSE images of sample EG10-087.
32. (a) Compositional maps of monazite 46 from sample EG10-118. Spots shown are 6.1, 6.2, 6.3 and 6.4 (b) compositional maps of monazite 48 from sample EG10-118. Spots shown are 1.6, 1.5c, 1.4c, 1.1, 1.2 and 2.8 (c) compositional maps of monazite 49 from sample EG10-118. Spot shown is 5.2 (d) compositional maps of monazite 54 from sample EG10-136. Spots shown are 2.1, 2.2 and 2.3 (e) compositional maps of monazite 58 from sample EG10-136. Spots shown are 5.1, 5.2, 5.3, 5.4, 5.5 and 5.6.
33. (a) Concordia plot of all monazite analyses for sample EG10-118. Intercept ages are in Table 12 (b) $^{206}Pb/^{207}Pb$ weighted average plot of all analyses in sample EG10-118 (c) Concordia plot of all

analyses of monazite grains situated in spinel grains for sample EG10-118 (d) Concordia plot of all analyses of monazite grains situated in the matrix for sample EG10-118. (e) $^{206}Pb/^{207}Pb$ weighted average plot of all analyses from monazite rims in sample EG10-118 (f) $^{206}Pb/^{207}Pb$ weighted average plot of all analyses from monazite cores in sample EG10-118

34. (a) Concordia plot of all monazite analyses for sample EG10-136. Intercept ages are in Table 12 (b) $^{206}Pb/^{207}Pb$ weighted average plot of all analyses in sample EG10-136 (c) concordia plot of all analyses of monazite grains situated in feldspar grains for sample EG10-136 (b) concordia plot of all analyses of monazite grains situated in the matrix for sample EG10-136.
35. In this figure X_{Mg} = Mg/(Mg + Fe) (a) diffusional-based cooling estimates for sample EG10-BXX (garnet 1) compared to the measured transect of X_{Mg}, with different rates of linear cooling (b) diffusional-based cooling estimates for sample EG10-BXX (garnet 2) compared to the measured transect of X_{Mg}, with different rates of linear cooling (c) diffusional-based cooling estimates for sample EG10-110 (garnet a) compared to the measured transect of XMg, with different rates of linear cooling. Values A are modelling estimates using the XMg values measured in biotite grains in the sample, Values B are recorded with a systematic estimation of XMg of biotite being 0.6 (d) diffusional-based cooling estimates for sample EG10-087 (Centre – B) compared to the measured transect of XMg, with different rates of linear cooling. Values A are modelling estimates using the XMg values measured in biotite grains in the sample Values B are recorded with a systematic estimation of XMg of biotite being 0.6
36. A map of the Eastern Ghats province displaying a compilation of all results from this study.
37. A schematic diagram of the crust of a large hot orogen from Chardon *et al.* (2009)

TABLES

Without Fe_2O_3				Incorporating Fe_2O_3		
ID number	112	125	144	ID number	117	137.000
Analysis No.	063_1	063_14	063_33	Analysis No.	063_6	063_26
Mineral	**Gt**	**Ksp**	**Ru**	**Mineral**	**Sil**	**Ilm**
SiO2	38.0226	65.1318	0.0744	SiO2	36.7901	0.025
TiO2	0.0186	0.0739	98.4898	TiO2	0.0144	52.322
Al2O3	21.413	18.5921	0.0003	Al2O3	62.4459	0.000
Cr2O3	0.0391	0.0002	0.0386	Cr2O3	0.109	0.037
FeO	32.5416	0.0329	0.2808	FeO	0.2736	44.424
MnO	0.38	0.0002	0.0002	MnO	0.0194	0.125
MgO	6.325	0.0035	0.0129	MgO	0.0006	1.322
ZnO	0.0002	0.0069	0.0001	ZnO	0.0002	0.028
CaO	1.6214	0.1076	0.0369	CaO	0.0158	0.008
Na2O	0.0012	1.4298	0.0032	Na2O	0.0038	0.000
K2O	0.0001	14.5934	0.018	K2O	0.0166	0.000
NiO	0	0	0	NiO	0	0.000
Total	100.3628	99.9723	98.9552	Total	99.6894	98.29
No. Oxygens	12	8	2	No. Oxygens	5	3
Si	2.988553023	2.993051557	0.001000959	Si	0.996378992	0.000640716
Ti	0.001099573	0.002554215	0.996613052	Ti	0.000293324	1.000560585
Al	1.983475153	1.006884503	4.75658E-06	Al	1.993093239	8.9891E-06
Cr	0.002429634	7.26601E-06	0.000410559	Cr	0.002333807	0.000745733
Fe2+	2.138755841	0.001264213	0.003158957	Fe3+	0.01200131	0
Mn2+	0.025295396	7.78377E-06	2.27883E-06	Fe2+	-0.00580529	0.944455712
Mg	0.741147354	0.000239781	0.000258737	Mn2+	0.000444973	0.002685158
Zn	1.16054E-05	0.00023409	9.93243E-07	Mg	2.42253E-05	0.050120982
Ca	0.136530991	0.005297309	0.000531853	Zn	3.99886E-06	0.000533084
Na	0.000182856	0.12738103	8.34645E-05	Ca	0.00045843	0.000226081
K	1.0026E-05	0.855434222	0.000308905	Na	0.00019952	1.97166E-05
Ni	0	0	0	K	0.00057347	3.2432E-06
z(g)	0.04526238	0.77886686	0.134661818	Ni	0	0
Total Cations (S)	8.017491452	4.99235597	1.002374515			
Xmg (mg/(fe+mg))	0.257351482	0.159429294	0.07570506	Total cations (S)	3	2
Xmg(divalent)	0.243658914	0.034044386	0.065456251	Xfe2+	1.004190462	0.949605714
y(opx)1	-			Xfe(tot.)	0.996105406	0.949605714
y(opx)2	-			fe3+/(fe3+ + fe2+)	1.936938492	0
y(bt)	-			Xfe2 (C Zn etc)	1.191155436	0.94632848
y(spr)	-			Xal	0.666704048	0.013835667
X(alm)	0.703138061			Xal(tot.)	0.663457539	8.97155E-06
X(py)	0.243659843			y(opx1)		
X(grs)	0.044885973			y(spr)		
X(spss)	0.008316123					
x(g)	0.742648518			Xfe2+ (almandine)		
				Xmg (pyrope)		
				Xmn (spessartine)		
				Xfe3+ (andradite)		
				Xca (grossular)		

Table 1: Representative mineral chemistry of sample EG10-063

Mineral Chemistry without Fe2O3												Mineral Chemistry Incorporating Fe2O3			
Textural Location	Blocky rim of osm	Symplectite	Blocky around g							in osm	in symplectite			in osm	symplectite
ID number	1	77	63	7	11	41	49	83	106	34	71	ID number	29	39	112
Analysis No.	ak5_1_1	ak5_51	ak5_44_1	ak5_3	ak5_7	ak5_30	ak5_35	ak5_57	ak5_69	ak5_23	ak5_45	Analysis No.	ak5_18	ak5_28	ak5_75
Mineral	**Opx**	**Opx**	**Opx**	**Ru**	**Sil**	**Cd**	**Ksp**	**Pl**	**Gt**	**Bi**	**Bi**	**Mineral**	**Sil**	**Sa**	**Sa**
SiO2	47.5656	48.3044	49.5407	0.0781	35.0912	49.213	64.1323	63.1815	40.2666	45.9368	37.1809	SiO2	36.2364	11.7919	12.6431
TiO2	0.0938	0.1298	0.1848	97.2711	0.0306	0.0002	0.0389	0.0421	0.0565	0.1692	5.3193	TiO2	0.0002	0.1044	0.063
Al2O3	6.2672	7.8559	8.4724	0.0003	58.687	31.8695	18.0467	21.4958	22.4299	7.1042	13.1198	Al2O3	59.9038	57.1146	58.3
Cr2O3	0.1364	0.1718	0.1589	0.1443	0.2906	0.0185	0.0401	0.0002	0.0837	0.3222	0.2439	Cr2O3	0.2454	1.2119	1.094
FeO	17.3196	15.5896	16.4215	0.1128	0.4193	2.941	0.0729	0.1184	20.6772	16.499	7.1818	FeO	0.4384	8.3391	7.0102
MnO	0.1504	0.1346	0.1109	0.0343	0.0002	0.0452	0.0088	0.0002	0.4193	0.1433	0.0732	MnO	0.0002	0.0479	0.0002
MgO	24.0461	24.9352	24.7585	0.0195	0.0002	11.8329	0.0039	0.0244	14.96	23.1952	18.7311	MgO	0.0025	15.641	16.7772
ZnO	0.0218	0.0046	0.1044	0.0001	0.0002	0.0454	0.0002	0.1559	0.0307	0.0002	0.1062	ZnO	0.0002	0.0002	0.0002
CaO	0.0291	0.0497	0.0258	0.0063	0.0002	0.029	0.3818	3.6164	0.6888	0.0647	0.0002	CaO	0.0029	0.0121	0.0447
Na2O	0.0299	0.0159	0.0254	0.0509	0.0056	0.0329	3.1715	8.0075	0.0222	0.0003	0.078	Na2O	0.01	0.0427	0.0265
K2O	0.024	0.0041	0.0076	0.003	0.0079	0.0032	11.8847	2.9312	0.0081	0.0044	9.8833	K2O	0.0001	0.0001	0.0001
NiO	0	0	0	0	0	0	0	0	0	0	0	NiO	0	0	0
Total	95.6839	97.1956	99.8109	97.7207	94.533	96.0308	97.7818	99.5736	99.643	93.4395	91.9177	Total	96.8401	94.3059	95.9592
No. Oxygens	6	6	6	2	5	18	8	8	12	11	11	No. Oxygens	5	20	20
Si	1.817068675	1.79688928	1.797178697	0.001063605	1.004448057	5.061262258	2.993157794	2.836712298	2.999318712	3.288916659	2.795654061	Si	1.011996605	1.4931088	1.5631466
Ti	0.002695089	0.003631627	0.005042234	0.99633411	0.000658783	1.54704E-05	0.001365508	0.001421672	0.003165323	0.009111384	0.300822201	Ti	4.20103E-06	0.0099426	0.0058584
Al	0.28215127	0.344398035	0.362214363	4.81483E-06	1.979708581	3.862640983	0.992614669	1.137389107	1.968951809	0.59942852	1.162574625	Al	1.971598487	8.5228511	8.4946363
Cr	0.004119435	0.005052458	0.004557198	0.001553605	0.006576121	0.001504166	0.001479592	7.09905E-06	0.004928877	0.018237385	0.014498405	Cr	0.005418181	0.1213164	0.1069322
Fe2+	0.553247387	0.484922962	0.498132754	0.001284522	0.010035922	0.252916508	0.002845008	0.004445086	1.287871512	0.987763341	0.451543911	Fe3+	0	0.3602279	0.2667892
Mn2+	0.00486592	0.004240513	0.003407214	0.000395605	4.8484E-06	0.003936916	0.000347836	7.60491E-06	0.026450949	0.008689145	0.004661368	Fe2+	0.010237825	0.5227097	0.4579466
Mg	1.369455388	1.382841357	1.338993073	0.000395903	8.53462E-06	1.814241402	0.000271358	0.001633203	1.661246687	2.475797554	2.099673139	Mn2+	4.73045E-06	0.0051367	2.094E-05
Zn	0.000614819	0.000126329	0.00279603	1.00541E-06	4.22641E-06	0.003447046	6.8912E-06	0.005167538	0.001688217	1.05714E-05	0.005895224	Mg	0.000104088	2.9525486	3.0923632
Ca	0.001190949	0.001980674	0.001002699	9.19161E-05	6.13312E-06	0.003195206	0.019090207	0.173949722	0.05496582	0.004962704	1.61107E-05	Zn	4.1236E-06	1.87E-05	1.826E-05
Na	0.002214409	0.001146674	0.001786369	0.001343864	0.00031076	0.006559689	0.286962971	0.696996591	0.003205819	4.16411E-05	0.011370158	Ca	8.67669E-05	0.0016414	0.0059207
K	0.001169496	0.000194548	0.000351683	5.21146E-05	0.000288447	0.000419796	0.707538437	0.167872604	0.000769612	0.000401841	0.9479262	Na	0.00054143	0.010482	0.0063519
Ni	0	0	0	0	0	0	0	0	0	0	0	K	3.5624E-06	1.615E-05	1.577E-05
												Ni	0	0	0
Total Cations (S)	4.038792836	4.025424458	4.015462315	1.002521065	3.002050413	11.01013944	5.005680271	5.025602525	8.012563337	7.393360745	7.794635402				
Xmg (mg/(fe+mg))	0.712255376	0.74037251	0.72885213	0.235596944	0.000849684	0.877650127	0.087075077	0.268694461	0.56330285	0.714812769	0.82300843	Total cations (S)	3	14	14
Xmg(divalent)	0.70979243	0.737864908	0.72600445	0.182531939	0.0008484	0.873181415	0.012027578	0.008818438	0.547864252	0.712004185	0.819611811	Xfe2+	0.989935365	0.1504089	0.1289878
y(opx)1	0.099219945	0.141287315	0.15939306	-		-	-	-	-			Xfe(tot.)	0.989935365	0.2302023	0.1898656
y(opx)2	0.141075635	0.172199018	0.181107182	-		-	-	-	-			fe3+/(fe3+ + fe2+)	0	0.4079879	0.3681192
y(bt)	-	-	-	-		-		-	-			Xfe2 (C Zn etc)	0.980866314	0.1501153	0.1287716
y(spr)	-	-	-	-		-		-	-			Xal	0.660813021	0.850927	0.8445834
X(alm)	--	--	--	--		--			0.424965072			Xal(tot.)	0.659614239	0.8111248	0.8138681
X(py)	--	--	--	--		--			0.54816945			y(opx1)	-		
X(grs)	--	--	--	--		--			0.018137332			y(spr)	-		
X(spss)	--	--	--	--		--			0.008728145						
												Xfe2+ (almandine)	-		
												Xmg (pyrope)	-		
												Xmn (spessartine)	-		
												Xfe3+ (andradite)	-		
												Xca (grossular)	-		

Table 2: Representative mineral chemistry of sample EG10-AK5

Mineral Chemistry without Fe2O3						Mineral Chemistry Incorporating Fe2O3			
ID number	181	206	65	73	172	ID number	103	69.000	72
Analysis No.	bxxg1_2_9	bxxg1_13	bxx_7	bxx_15	bxxg1_1	Analysis No.	bxx_33_4	bxx_11	bxx_14
Mineral	**Gt Rim**	**Gt Core**	**Pl**	**Ksp**	**Bi**	**Mineral**	**Gt**	**Opx**	**Ilm**
SiO2	35.63	36.84	54.30	63.59	37.06	SiO2	37.800	49.124	0.046
TiO2	0.02	0.00	0.00	0.00	4.56	TiO2	0.087	0.082	52.190
Al2O3	20.35	21.03	28.05	18.27	12.29	Al2O3	21.149	1.104	0.000
Cr2O3	0.06	0.05	0.04	0.01	0.03	Cr2O3	0.009	0.000	0.015
FeO	30.73	30.74	0.06	0.00	13.23	FeO	30.588	32.648	44.738
MnO	0.99	1.01	0.00	0.00	0.02	MnO	1.000	0.397	0.303
MgO	4.13	5.21	0.01	0.00	15.56	MgO	5.007	14.812	0.836
ZnO	0.05	0.00	0.12	0.01	0.05	ZnO	0.085	0.197	0.000
CaO	4.74	3.49	10.96	0.19	4.11	CaO	4.645	0.529	0.012
Na2O	0.04	0.00	5.50	1.34	0.04	Na2O	0.025	0.028	0.000
K2O	0.02	0.00	0.15	14.82	9.76	K2O	0.000	0.000	0.013
NiO	0.00	0.00	0.00	0.00	0.00	NiO	0.000	0.000	0.000
Total	96.7596	98.3689	99.1959	98.2373	96.7084	Total	100.3955	98.92	98.1525
No. Oxygens	12	12	8	8	11	No. Oxygens	12	6	3
Si	2.945	2.967	2.474	2.985	2.760	Si	2.971	1.946	0.001
Ti	0.001	0.000	0.000	0.000	0.255	Ti	0.005	0.002	1.003
Al	1.982	1.996	1.506	1.010	1.079	Al	1.959	0.052	0.000
Cr	0.004	0.003	0.001	0.001	0.002	Cr	0.001	0.000	0.000
Fe2+	2.124	2.071	0.002	0.000	0.824	Fe3+	0.091	0.054	0.000
Mn2+	0.069	0.069	0.000	0.000	0.002	Fe2+	1.919	1.028	0.956
Mg	0.509	0.626	0.001	0.000	1.728	Mn2+	0.067	0.013	0.007
Zn	0.003	0.000	0.004	0.000	0.003	Mg	0.587	0.875	0.032
Ca	0.420	0.301	0.535	0.009	0.328	Zn	0.005	0.006	0.000
Na	0.007	0.000	0.486	0.122	0.006	Ca	0.391	0.022	0.000
K	0.002	0.000	0.009	0.887	0.927	Na	0.004	0.002	0.000
Ni	0	0	0	0	0	K	0.000	0.000	0.000
						Ni	0	0	0
Total Cations (S)	8.065	8.033	5.019	5.015	7.912				
Xmg (mg/(fe+mg))	0.193	0.232	0.272	0.641	0.677	Total cations (S)	8	4	2
Xmg(divalent)	0.163	0.204	0.002	0.001	0.599	Xfe2+	0.766	0.540	0.968
y(opx)1	-	-		-	-	Xfe(tot.)	0.774	0.553	0.968
y(opx)2	-	-		-	-	fe3+/(fe3+ + fe2+)	0.045	0.049	0.000
y(bt)	-	-			-	Xfe2 (C Zn etc)	0.647	0.529	0.961
y(spr)	-	-			-	Xal	0.397	0.026	0.008
X(alm)	0.680	0.675			--	Xal(tot.)	0.390	0.025	0.000
X(py)	0.163	0.204			--	y(opx1)	-	-0.002	
X(grs)	0.134	0.098			--	y(spr)	-		
X(spss)	0.022	0.022			--				
Z(g)	0.137	0.101				Xfe2+ (almandine)	0.648		
X(g)	0.807	0.768				Xmg (pyrope)	0.198		
						Xmn (spessartine)	0.022		
						Xfe3+ (andradite)	0.046	-	
						Xca (grossular)	0.086	-	

Table 3 : Representative mineral chemistry of sample EG10-BXX

Mineral chemistry without Fe2O3								
Textural location	Inclusion	Inclusion	Matrix	Matrix	Inclusion	Matrix	G1 blocky	G2-rimming sa
ID number	255	252	286	171	75	91	132	194
Analysis No.	136_193	136_190	136_204	136_137	136_62	136_73	136_106_1	136_150_2
Mineral	**Ternary fedspar**	**Ternary Feldspar**	Ksp	Pl	Bi	Bi	Gt	Gt
SiO2	63.4839	64.6088	65.5565	61.0994	38.9084	36.9556	39.5168	39.0482
TiO2	0.0002	0.0348	0.0002	0.0002	4.1336	4.7275	0.0505	0.0023
Al2O3	21.3812	20.3651	18.313	22.9251	13.8678	13.1469	22.2176	21.811
Cr2O3	0.0002	0.0002	0.0002	0.0598	0.0285	0.0002	0.0002	0.0015
FeO	0.2495	0.1682	0.082	0.0084	7.5306	7.1681	24.3232	24.6632
MnO	0.0252	0.0002	0.0002	0.0265	0.0002	0.0002	0.3528	0.4477
MgO	0.0003	0.0002	0.0119	0.0127	19.6165	19.1167	13.0616	11.9252
ZnO	0.0002	0.0002	0.0002	0.0401	0.0002	0.1345	0.0002	0.0002
CaO	3.6987	2.5452	0.0993	5.4557	0.0002	0.0002	0.8194	1.2124
Na2O	6.2889	4.9731	1.3677	6.8384	0.1173	0.0474	0.0003	0.0003
K2O	4.925	7.7521	14.7744	2.6518	9.9537	10.2867	0.0001	0.0001
NiO	0	0	0	0	0	0	0	0
Total	100.0533	100.4481	100.2056	99.1181	94.157	91.584	100.3427	99.1121
No. Oxygens	8	8	8	8	11	11	12	12
Si	2.850081605	2.905341193	3.006693492	2.760949	2.842147	2.794603	2.975413215	2.989565356
Ti	6.75329E-06	0.001177	6.89914E-06	6.8E-06	0.227103	0.268883	0.002859886	0.000132442
Al	1.131242897	1.079250123	0.989835412	1.220851	1.193826	1.171638	1.971481722	1.967943854
Cr	7.09853E-06	7.11018E-06	7.25184E-06	0.002136	0.001646	1.2E-05	1.19053E-05	9.07911E-05
Fe2+	0.009366286	0.006324623	0.003144781	0.000317	0.459977	0.45326	1.531402603	1.578918122
Mn2+	0.000958149	7.61683E-06	7.76859E-06	0.001014	1.24E-05	1.28E-05	0.022497426	0.029029053
Mg	2.00789E-05	1.34079E-05	0.000813664	0.000856	2.136238	2.155151	1.466178262	1.361123657
Zn	6.62882E-06	6.63969E-06	6.77198E-06	0.001338	1.08E-05	0.007509	1.11175E-05	1.13044E-05
Ca	0.177895402	0.122616609	0.004879154	0.264116	1.57E-05	1.62E-05	0.066097251	0.099443152
Na	0.547364633	0.433551813	0.121610925	0.599079	0.016612	0.006949	4.3792E-05	4.45284E-05
K	0.282038858	0.444665925	0.864355238	0.152852	0.927463	0.992259	9.6045E-06	9.76598E-06
Ni	0	0	0	0	0	0	0	0
	0.543398426	0.433190382	0.872341245	0.589618				
Total Cations (S)	4.99898839	4.992962059	4.991361359	5.003516	7.805051	7.850293	8.036006784	8.026312026
Xmg (mg/(fe+mg))	0.002139156	0.002115466	0.205551475	0.729404	0.822828	0.826231	0.489120503	0.462960651
Xmg(divalent)	0.000106663	0.000103962	0.091917235	0.003197	0.822816	0.823851	0.475077636	0.443575832
y(opx)1	-	-			-	-	-	-
y(opx)2					-	-	-	-
y(bt)					-	-	-	-
y(spr)					-	-	-	-
X(alm)					--	--	0.496213706	0.514554644
X(py)					--	--	0.475079347	0.443577466
X(grs)					--	--	0.021417204	0.032407593
X(spss)					--	--	0.007289743	0.009460297

Mineral Chemistry incorporating Fe2O3								
		rimming sp	rim of sa	inclusion				
ID number	1	6.000	61.000	95	152	42	132	194
Analysis No.	136_1	136_6	136_51	136_77	136_118	136_32	136_106_1	136_150_2
Mineral	Sp	Sa	Sil	Ilm	Crn	Mt	Gt	Gt
SiO2	0.0112	11.989	35.847	0.0076	0.555	0.0149	39.5168	39.0482
TiO2	0.0164	0.037	0.000	48.1483	0.0157	0.0277	0.0505	0.0023
Al2O3	56.5911	57.526	59.448	0.0003	96.3799	8.3103	22.2176	21.811
Cr2O3	0.2989	0.093	0.000	0.0002	0.0334	0.2919	0.0002	0.0015
FeO	25.8478	10.609	1.302	43.9455	1.114	79.4328	24.3232	24.6632
MnO	0.0831	0.011	0.026	0.079	0.0328	0.0001	0.3528	0.4477
MgO	11.7024	14.968	0.019	1.5953	0.0395	1.8436	13.0616	11.9252
ZnO	0.715	0.021	0.034	0.0671	0.0733	0.1151	0.0002	0.0002
CaO	0.0002	0.000	0.000	0.0103	0.0173	0.0001	0.8194	1.2124
Na2O	0.0111	0.000	0.028	0.0004	0.0002	0.0267	0.0003	0.0003
K2O	0.0025	0.008	0.011	0.0005	0.039	0.0023	0.0001	0.0001
NiO	0	0.000	0.000	0	0	0	0	0
Total	95.2797	95.26	96.71	93.8545	98.3001	90.0655	100.3427	99.1121
No. Oxygens	4	20	5	3	3	4	12	12
Si	0.000315	1.511	1.003761197	0.000201	0.009626	0.000563	2.962081	2.979765
Ti	0.000347	0.003	4.21208E-06	0.959613	0.000205	0.000787	0.002847	0.000132
Al	1.876281	8.543	1.961738179	9.37E-06	1.969924	0.370183	1.962648	1.961492
Cr	0.006648	0.009	4.42741E-06	4.19E-06	0.000458	0.008723	1.19E-05	9.05E-05
Fe3+	0.116442	0.421	0.032636033	0.080395	0.010827	1.620461	0.107536	0.078677
Fe2+	0.491619	0.697	-0.00215784	0.89334	0.005328	0.89011	1.417005	1.495065
Mn2+	0.00198	0.001	0.000618948	0.001773	0.000482	3.2E-06	0.022397	0.028934
Mg	0.490817	2.812	0.000784798	0.063022	0.001021	0.103887	1.459609	1.356662
Zn	0.01485	0.002	0.000694587	0.001313	0.000939	0.003212	1.11E-05	1.13E-05
Ca	6.03E-06	0.000	5.99967E-06	0.000292	0.000321	4.05E-06	0.065801	0.099117
Na	0.000605	0.000	0.00153085	2.05E-05	6.72E-06	0.001957	4.36E-05	4.44E-05
K	8.97E-05	0.001	0.000378608	1.69E-05	0.000863	0.000111	9.56E-06	9.73E-06
Ni	0	0.000	0	0	0	0	0	0
Total cations (S)	3	14.000	3	2	2	3	8	8
Xfe2+	0.500408	0.199	1.57157613	0.934103	0.839154	0.895486	0.492595	0.524267
Xfe(tot.)	0.553347	0.284	0.9748969	0.939213	0.940542	0.960264	0.510879	0.537039
fe3+/(fe3+ + fe2+)	0.191497	0.377	1.070799471	0.082564	0.670189	0.645455	0.070537	0.049994
Xfe2 (C Zn etc)	0.491977	0.198	40.32826445	0.930815	0.658516	0.892595	0.477939	0.501735
Xal	0.999832	0.850	0.661520348	0.044452	0.995138	0.998481	0.398529	0.396962
Xal(tot.)	0.938125	0.815	0.65431752	9.01E-06	0.989395	0.185025	0.389791	0.390723
y(opx1)							-	-
y(spr)							-	-
Xfe2+ (almandine)							0.477941	0.501737
Xmg (pyrope)							0.492311	0.45529
Xmn (spessartine)							0.007554	0.00971
Xfe3+ (andradite)							0.053768	0.039339
Xca (grossular)							-0.03157	-0.00608

Table 4: *Representative mineral chemistry of* sample EG10-136

Without Fe2O3						Incorporating Fe2O3							
ID number	5	82	203	**253**	206	ID number	5	4	25	42	50	110	253
Analysis No.	118_a_4_1	a_35	a_135	a_176	a_138	Analysis No.	118_a_4_1	118_a_3	a_12	a_21	a_24	a_53	a_176
Mineral	**Gt**	**Bi**	**Ksp**	Opx	**Cd**	**Mineral**	**Gt**	**Sil**	**Sp**	**Ülvo-spinel**	**Sa**	**Crn**	**Opx**
SiO2	39.1682	38.166	64.5047	49.8489	51.4743	SiO2	39.1682	36.4908	0.0119	0.0184	12.668	0.0869	49.8489
TiO2	0.0112	4.3985	0.0407	0.0933	0.0221	TiO2	0.0112	0.0002	0.0002	21.0541	0.0629	0.0256	0.0933
Al2O3	21.9576	15.1072	18.1681	6.4692	32.9599	Al2O3	21.9576	60.5919	58.9518	0.1039	57.4334	95.0824	6.4692
Cr2O3	0.0129	0.0733	0.0694	0.0269	0.0002	Cr2O3	0.0129	0.0002	0.3558	0.1128	0.0399	0.0002	0.0269
FeO	25.3142	9.2171	0.1819	21.1282	1.3006	FeO	25.3142	1.0943	25.6467	67.6779	10.6626	1.0543	21.1282
MnO	0.4519	0.039	0.0002	0.1793	0.0159	MnO	0.4519	0.0002	0.0624	0.0642	0.0002	0.0002	0.1793
MgO	11.8697	18.6975	0.0152	22.4117	1.8623	MgO	11.8697	0.0247	10.8453	0.3092	14.8826	0.0002	22.4117
ZnO	0.088	0.0642	0.0147	0.0002	0.0002	ZnO	0.088	0.1044	0.8421	0.064	0.0002	0.0002	0.0002
CaO	1.0246	0.036	0.0569	0.0149	0.1875	CaO	1.0246	0.0002	0.0002	0.0178	0.0299	0.0191	0.0149
Na2O	0.0339	0.1024	1.1453	0.0003	0.3758	Na2O	0.0339	0.0002	0.0136	0.0146	0.0346	0.0155	0.0003
K2O	0.0087	8.6585	14.8833	0.0097	6.3199	K2O	0.0087	0.0081	0.0001	0.0001	0.0228	0.0058	0.0097
NiO	0	0	0	0	0	NiO	0	0	0	0	0	0	0
Total	99.9409	94.5597	99.0804	100.1826	94.5187	Total	99.9409	98.3152	96.7301	89.437	95.8371	96.2904	100.1826
No. Oxygens	12	11	8	6	18	No. Oxygens	12	5	4	3	20	3	6
			0.925262										
Si	2.98176599	2.779135	2.998144	1.839903	5.459197	Si	2.968721	1.004898	0.00033	0.000502	1.588266	0.001537	1.832274
Ti	0.000641283	0.240896	0.001423	0.00259	0.001763	Ti	0.000638	4.14E-06	4.18E-06	0.432266	0.005931	0.00034	0.002579
Al	1.969948648	1.296424	0.995178	0.281397	4.119593	Al	1.96133	1.966452	1.92837	0.003342	8.486134	1.981496	0.280231
Cr	0.00077638	0.00422	0.00255	0.000785	1.68E-05	Cr	0.000773	4.35E-06	0.007808	0.002434	0.003955	2.8E-06	0.000782
Fe2+	1.611414628	0.561217	0.00707	0.652086	0.115341	Fe3+	0.105001	0.024034	0.063889	1.129463	0.333572	0.015409	0.049757
Mn2+	0.029135403	0.002405	7.87E-06	0.005605	0.001428	Fe2+	1.499363	0.001165	0.531359	0.415338	0.784273	0.00018	0.599625
Mg	1.347114664	2.029745	0.001053	1.233216	0.294451	Mn2+	0.029008	4.66E-06	0.001467	0.001484	2.12E-05	3E-06	0.005582
Zn	0.004945781	0.003451	0.000504	5.45E-06	1.57E-05	Mg	1.341221	0.001014	0.448776	0.012583	2.781756	5.27E-06	1.228102
Ca	0.083563421	0.002808	0.002833	0.000589	0.021304	Zn	0.004924	0.002123	0.017256	0.00129	1.85E-05	2.61E-06	5.43E-06
Na	0.005003201	0.014456	0.103202	2.15E-05	0.077269	Ca	0.083198	5.9E-06	5.95E-06	0.000521	0.004016	0.000362	0.000587
K	0.000844828	0.804238	0.882408	0.000457	0.854983	Na	0.004981	1.07E-05	0.000732	0.000773	0.00841	0.000531	2.14E-05
Ni	0	0	0	0	0	K	0.000841	0.000285	3.54E-06	3.48E-06	0.003646	0.000131	0.000455
						Ni	0	0	0	0	0	0	0
Total Cations (S)	8.035154227	7.738994	4.994374	4.016655	10.94536								
Xmg (mg/(fe+mg))	0.455332542	0.783394	0.129664	0.654121	0.718537	Total cations (S)	8	3	3	2	14	2	4
Xmg(divalent)	0.437918892	0.780783	0.091838	0.651977	0.680748	Xfe2+	0.527836	0.534609	0.542128	0.970595	0.219929	0.971546	0.328071
y(opx)1	-			0.1213		Xfe(tot.)	0.544667	0.961315	0.570148	0.99192	0.286656	0.999662	0.345879
y(opx)2	-			0.140699		fe3+/(fe3+ + fe2+)	0.065447	0.953773	0.107332	0.731138	0.298406	0.988452	0.076622
y(bt)	-					Xfe2 (C Zn etc)	0.506933	0.270146	0.531963	0.963179	0.219679	0.325698	0.326967
y(spr)	-					Xal	0.397832	0.661804	0.999829	0.869361	0.842346	0.999225	0.132653
X(alm)	0.524680866					Xal(tot.)	0.389426	0.656492	0.963992	0.002132	0.814576	0.99135	0.1294
X(py)	0.438624099					y(opx1)	-						0.112505
X(grs)	0.027208471					y(spr)	-						
X(spss)	0.009486564												
						Xfe2+ (almandine)	0.507779						
						Xmg (pyrope)	0.454222						
						Xmn (spessartine)	0.009824						
						Xfe3+ (andradite)	0.052501						
						Xca (grossular)	-0.02432						

Table 5: Representative mineral chemistry of sample EG10-118

Spot	% $206Pb_c$	ppm U	ppm Th	ppm 206*	232Th /238U	(1) 206Pb /238U Age	(1) 207Pb /206Pb Age	% Dis-cor-dant	(1) 238U/ $206Pb^*$	±%	(1) $207Pb^*$ /$206Pb^*$	±%	(1) $207Pb^*$ /235U	±%	(1) $206Pb^*$ /238U	±%
ak3-3.1	--	699	12788	90.9	18.9	908 ±12	972 ±15	+7	6.61	1.4	0.0715	0.7	1.491	1.5	0.1512	1.4
ak3-4.1	--	786	12683	106	16.7	942 ±12	966 ±119	+3	6.36	1.4	0.0713	5.8	1.546	6.0	0.1573	1.4
ak3-4.2	--	623	12801	81.9	21.2	918 ±11	960 ±15	+5	6.53	1.3	0.0711	0.7	1.500	1.5	0.1531	1.3
ak3-5.1	--	627	12380	80.1	20.4	894 ±10	963 ±14	+8	6.72	1.3	0.0712	0.7	1.461	1.4	0.1488	1.3
ak3-5.2	--	604	12361	76.8	21.1	890 ±11	971 ±15	+9	6.76	1.3	0.0715	0.7	1.458	1.5	0.1480	1.3
ak3-5.3	--	692	13061	95.4	19.5	960 ±11	968 ±17	+1	6.23	1.3	0.0714	0.8	1.580	1.5	0.1606	1.3
ak3-5.4	--	683	13707	85.6	20.7	879 ±10	967 ±47	+10	6.85	1.3	0.0713	2.3	1.436	2.6	0.1460	1.3
ak3-8.1	--	491	17558	69	36.9	976 ±12	989 ±18	+1	6.12	1.3	0.0721	0.9	1.626	1.5	0.1635	1.3
ak3-8.2	--	492	15913	68.7	33.4	970 ±12	1025 ±21	+6	6.16	1.3	0.0734	1.0	1.643	1.7	0.1624	1.3
ak3-8.3	--	590	15797	82.6	27.7	973 ±12	973 ±97	+0	6.14	1.4	0.0716	4.7	1.607	4.9	0.1629	1.4
ak3-8.4	--	675	16098	96.2	24.6	989 ±12	931 ±17	-7	6.03	1.3	0.0701	0.8	1.602	1.5	0.1658	1.3
ak3-9.1	--	682	17123	90.2	25.9	922 ±11	991 ±16	+7	6.50	1.3	0.0722	0.8	1.531	1.5	0.1538	1.3
ak3-9.2	--	419	16825	59	41.5	978 ±12	1101 ±40	+12	6.10	1.3	0.0762	2.0	1.722	2.4	0.1639	1.3
ak3-9.3	--	716	15815	93.8	22.8	914 ±11	969 ±18	+6	6.56	1.2	0.0714	0.9	1.501	1.5	0.1524	1.2
ak3-9.4	--	1727	15208	239	9.1	963 ±11	972 ±9	+1	6.21	1.2	0.0715	0.4	1.588	1.3	0.1610	1.2
ak3-9.5	--	542	15680	76	29.9	975 ±11	979 ±17	+0	6.12	1.3	0.0718	0.8	1.616	1.5	0.1633	1.3
ak3-10.1	--	335	14255	45.6	43.9	947 ±13	1079 ±27	+13	6.32	1.4	0.0754	1.3	1.645	2.0	0.1582	1.4
ak3-2.1	--	783	18344	110	24.2	976 ±10	995 ±12	+2	6.119	1.2	0.07233	0.60	1.630	1.3	0.1634	1.2
ak3-2.2	--	732	17952	103	25.3	980 ±11	998 ±18	+2	6.091	1.2	0.07242	0.90	1.639	1.5	0.1642	1.2

Table 6: SHRIMP U-Pb-Th data for Sample EG10-063

Spot	% $206Pb_c$	ppm U	ppm Th	ppm 206*	232Th /238U	(1) 206Pb /238U Age		(1) 207Pb /206Pb Age		% Dis-cor-dant	(1) 238U/ $206Pb^*$	±%	(1) $207Pb^*$ /$206Pb^*$	±%	(1) $207Pb^*$ /235U	±%	(1) $206Pb^*$ /238U	±%	err corr	Textural location
063-1.2	--	3373	51056	464	15.6	957	±18	982	±10	+3	6.25	2.0	0.0719	0.49	1.587	2.1	0.1601	2.0	0.97	edge of g
063-2.1	--	2791	55456	367	20.5	918	±18	1004	±13	+9	6.54	2.1	0.0726	0.66	1.532	2.2	0.1530	2.1	0.95	edge of g
063-3.1	--	2731	75450	361	28.5	922	±18	971	±13	+5	6.50	2.1	0.0715	0.66	1.515	2.2	0.1538	2.1	0.95	edge of g
063-4.1	--	2227	76975	305	35.7	953	±18	965	±12	+1	6.28	2.1	0.0713	0.58	1.565	2.1	0.1593	2.1	0.96	edge of g
063-1.1	--	2165	76956	297	36.7	956	±18	967	±13	+1	6.26	2.1	0.0713	0.64	1.572	2.2	0.1598	2.1	0.95	edge of g
063.1.3	--	2492	64825	340	26.9	951	±18	988	±14	+4	6.29	2.1	0.0721	0.70	1.580	2.2	0.1590	2.1	0.95	?
063-5.1	--	2541	75786	326	30.8	897	±17	988	±16	+10	6.70	2.1	0.0721	0.79	1.484	2.2	0.1493	2.1	0.93	edge of g
063-5.3	--	4504	80230	588	18.4	912	±17	988	±12	+8	6.58	2.0	0.0721	0.59	1.510	2.1	0.1520	2.0	0.96	middle of g
063-5.4	--	3786	68010	505	18.6	930	±18	970	±20	+4	6.44	2.0	0.0714	0.98	1.529	2.3	0.1552	2.0	0.90	middle of g
063-5.5	--	4126	76261	551	19.1	932	±18	978	±12	+5	6.43	2.1	0.0717	0.57	1.537	2.1	0.1555	2.1	0.96	middle of g
063-6.1	--	2460	73910	326	31.0	925	±19	973	±14	+5	6.48	2.2	0.0716	0.69	1.523	2.3	0.1544	2.2	0.95	matrix
063-6.2	--	2753	70160	359	26.3	911	±17	960	±13	+5	6.59	2.1	0.0711	0.62	1.488	2.1	0.1518	2.1	0.96	matrix
063-7.1	0.01	3774	62931	468	17.2	869	±17	944	±12	+8	6.93	2.1	0.0705	0.58	1.404	2.1	0.1444	2.1	0.96	matrix
063-8.1	--	3048	81090	376	27.5	865	±17	934	±13	+8	6.96	2.1	0.0702	0.63	1.390	2.2	0.1436	2.1	0.96	edge of g
063-8.2	--	3003	82924	393	28.5	914	±17	973	±12	+6	6.56	2.0	0.0715	0.61	1.503	2.1	0.1524	2.0	0.96	edge of g

Table 7: SHRIMP U-Pb-Th data for Sample EG10-AK3

Analysis_#	Pb207/U235		Pb206/U238		rho	Concorda	Pb207/Pb206		Pb206/U238		Pb207/U235		Textural Location
02a	1.52666	0.02456	0.15895	0.0025	0.97767	104	913.8	22.45	950.9	13.92	941.2	9.87	cordierite sapphirine intergrowth
03a	1.53341	0.02465	0.15778	0.00248	0.97778	101	939.6	22.41	944.4	13.81	943.9	9.88	cordierite sapphirine intergrowth
10a	1.32109	0.02143	0.14032	0.00221	0.97092	97	873.4	23.07	846.5	12.5	855	9.38	gt breakdown
11a	1.29776	0.02761	0.13468	0.0022	0.7678	88	926.1	37.96	814.5	12.47	844.7	12.2	gt breakdown
11b	1.13129	0.02077	0.12478	0.00201	0.87738	95	796	29.94	758	11.49	768.4	9.89	gt breakdown
12a	1.53364	0.02962	0.15309	0.00249	0.84215	92	1002.8	31.78	918.3	13.92	944	11.87	feldspar
13a	1.17704	0.01903	0.12823	0.00202	0.97435	94	823.1	23.19	777.8	11.54	789.9	8.88	gt breakdown
14a	1.1516	0.01926	0.12579	0.00197	0.93641	93	819	25.13	763.8	11.3	778	9.09	gt breakdown
15a	1.52262	0.02461	0.15435	0.00241	0.96603	95	972.7	22.72	925.3	13.47	939.5	9.9	inside gt
15b	1.4928	0.02501	0.15475	0.00246	0.94884	100	926.9	24.51	927.5	13.71	927.5	10.19	inside gt
16a	1.46808	0.02522	0.14914	0.00238	0.92894	92	969	25.56	896.1	13.35	917.3	10.37	gt breakdown
17a	1.33967	0.02167	0.14065	0.0022	0.96699	94	902	22.96	848.3	12.41	863.1	9.4	gt breakdown
20a	1.31174	0.02086	0.14079	0.00219	0.97815	99	856.8	23.32	849.1	12.35	850.9	9.16	gt breakdown
20b	1.29378	0.02007	0.13941	0.00215	0.99416	99	848.2	22.3	841.3	12.16	843	8.88	gt breakdown
21a	1.44546	0.02268	0.15306	0.00237	0.98685	104	883.7	22.57	918.1	13.26	908	9.42	edge of garnet
01a	1.31451	0.0214	0.14288	0.00225	0.9673	104	829.8	24.16	860.9	12.71	852.1	9.39	orthopyroxene
01b	1.39273	0.02518	0.14768	0.00238	0.89139	101	880.5	29.12	887.9	13.39	885.9	10.69	orthopyroxene
25a	1.38422	0.02327	0.14785	0.00235	0.94549	103	865.8	25.6	888.9	13.22	882.2	9.91	edge of opx/rim
25b	1.36162	0.02266	0.1458	0.00232	0.95615	102	860.5	25.14	877.4	13.03	872.6	9.74	edge of opx/rim
26a	1.21323	0.02136	0.13347	0.00215	0.91495	100	804	27.82	807.6	12.24	806.7	9.8	gt breakdown/growing with ru
06a	1.37862	0.02131	0.14226	0.00215	0.97773	92	936.1	21.82	857.4	12.11	879.9	9.1	symplectite
07a	0.7056	0.01127	0.08887	0.00134	0.94403	107	514.2	24.83	548.8	7.94	542.1	6.71	symplectite

Table 8: LA-ICPMS U-Pb data for sample EG10-AK5

Analysis_#	Pb207/U235		Pb206/U238		rho	Concordancy			Pb206/U238		Pb207/Pb206	
MZ01A	0.97802	0.07216	0.11943	0.00293	0.332510527	95			727.3	16.86	692.6	37.04
MZ02A	0.7884	0.06901	0.08323	0.00229	0.314333144	115			515.4	13.63	590.3	39.18
MZ06A	1.36069	0.06261	0.14166	0.00303	0.464847907	102			854	17.11	872.2	26.93
MZ10A	1.29423	0.07088	0.13735	0.0031	0.412117241	102			829.6	17.59	843.2	31.37
MZ12A	1.57276	0.06659	0.15013	0.00316	0.49713351	106			901.7	17.71	959.5	26.28
MZ14A	0.82122	0.05937	0.09519	0.00243	0.353107885	104			586.2	14.29	608.7	33.1
MZ16A	1.36734	0.07632	0.12557	0.003	0.428029318	115			762.6	17.16	875	32.74
MZ17A	1.54197	0.07869	0.15893	0.00358	0.441401213	100			950.8	19.91	947.3	31.43
MZ18A	1.06355	0.03639	0.12217	0.00228	0.545438927	99			743	13.11	735.6	17.91
MZ19A	1.67464	0.06481	0.15983	0.00322	0.520567453	105			955.8	17.88	998.9	24.6
MZ20A	1.39779	0.0506	0.14995	0.00289	0.532405809	99			900.7	16.18	888	21.43
MZ21A	1.52415	0.0461	0.16094	0.00288	0.591636931	98			962	15.99	940.1	18.54
MDC	0.63652	0.01858	0.08459	0.00148	0.599389368	96			523.4	8.78	500.2	11.53
MZ20B	1.39377	0.10108	0.15008	0.00427	0.392311404	98			901.4	23.94	886.3	42.87
MZ20C	1.46844	0.09276	0.15171	0.00391	0.407997982	101			910.5	21.91	917.5	38.16
MZ10B	1.59262	0.11919	0.16307	0.00481	0.394133501	99			973.8	26.64	967.3	46.68
MZ21B	1.44646	0.10291	0.15417	0.00435	0.396586781	98			924.3	24.27	908.4	42.71
MZ05A	1.1094	0.14764	0.14116	0.00538	0.286387957	89			851.2	30.4	757.9	71.07
MZ06B	1.24432	0.09505	0.13948	0.00406	0.381060607	98			841.7	22.98	820.8	43
MZ07A	0.85627	0.07694	0.11066	0.00343	0.344954648	93			676.6	19.93	628.1	42.09
MZ14B	1.16492	0.10529	0.11961	0.004	0.369999789	108			728.3	23.01	784.3	49.38
MZ17B	1.54665	0.11257	0.16113	0.00465	0.396502496	99			963	25.83	949.2	44.89
MZ17C	1.56958	0.12643	0.16058	0.00502	0.388101733	100			960	27.87	958.3	49.96
MZ19C	1.72123	0.13287	0.17117	0.00519	0.392782092	100			1018.5	28.57	1016.5	49.58
MZ20D	1.42653	0.1108	0.14962	0.00455	0.391528062	100			898.9	25.49	900.1	46.37
MZ20E	1.47538	0.11827	0.15718	0.0049	0.388891177	98			941.1	27.29	920.3	48.52

Table 9: LA-ICPMS U-Pb data for sample EG10-BXX

Spot	% $206Pb_c$	ppm U	ppm Th	ppm 206*	232Th /238U	(1) 206Pb /238U Age		(1) 207Pb /206Pb Age		% Dis-cor-dant	(1) 238U/ $206Pb^*$	±%	(1) $207Pb^*$ /$206Pb^*$	±%	(1) $207Pb^*$ /235U	±%	(1) $206Pb^*$ /238U	±%	err corr	Textural location
118-1.1	--	735	2E+5	97.8	231	929	±16	936	±22	+1	6.45	1.8	0.0703	1.1	1.50	2.1	0.155	1.8	0.9	ilmenite
118-1.2	--	823	1E+5	96.4	158	824	±14	929	±21	+12	7.33	1.8	0.0700	1.0	1.32	2.1	0.136	1.8	0.9	ilmenite
118-1.3	--	629	2E+5	61.9	272	700	±12	729	±30	+4	8.72	1.9	0.0636	1.4	1.01	2.3	0.115	1.9	0.8	ilmenite
118-1.4c	--	791	1E+5	99	157	877	±18	921	±21	+5	6.86	2.2	0.0698	1.0	1.40	2.4	0.146	2.2	0.9	ilmenite
118-1.5c	--	771	1E+5	90.6	160	826	±16	928	±22	+12	7.31	2.1	0.0700	1.1	1.32	2.4	0.137	2.1	0.9	ilmenite
118-1.6	--	645	2E+5	66.3	297	728	±13	728	±30	+0	8.36	1.9	0.0636	1.4	1.05	2.4	0.120	1.9	0.8	ilmenite
118-2.1	--	1072	2E+5	133	159	870	±15	906	±19	+4	6.92	1.8	0.0692	0.9	1.38	2.0	0.145	1.8	0.9	ilmenite
118-2.2	--	595	2E+5	79.4	267	931	±19	986	±24	+6	6.43	2.2	0.0720	1.2	1.54	2.5	0.155	2.2	0.9	ilmenite
118-3.1	--	550	1E+5	61.5	264	790	±14	905	±27	+14	7.67	1.9	0.0692	1.3	1.24	2.3	0.130	1.9	0.8	ilmenite
118-3.2c	--	726	1E+5	81.4	193	791	±14	861	±41	+9	7.66	1.8	0.0678	2.0	1.22	2.7	0.131	1.8	0.7	ilmenite
118-3.3c	--	700	1E+5	77.1	169	778	±14	855	±25	+10	7.80	1.9	0.0676	1.2	1.20	2.3	0.128	1.9	0.8	ilmenite
118-3.4	--	613	2E+5	68.8	268	792	±14	827	±27	+5	7.65	1.9	0.0667	1.3	1.20	2.3	0.131	1.9	0.8	ilmenite
118-4.1c	--	620	1E+5	72.8	241	827	±14	899	±25	+9	7.31	1.9	0.0690	1.2	1.30	2.2	0.137	1.9	0.8	ilmenite
118-4.2c	--	725	9E+4	92.3	129	891	±15	913	±22	+3	6.74	1.8	0.0695	1.1	1.42	2.1	0.148	1.8	0.9	ilmenite
118-4.3	--	552	2E+5	63.5	310	810	±15	868	±28	+7	7.47	2.0	0.0680	1.3	1.25	2.4	0.134	2.0	0.8	ilmenite
118-4.4	--	583	2E+5	70.7	297	851	±15	894	±26	+5	7.09	1.9	0.0689	1.3	1.34	2.3	0.141	1.9	0.8	ilmenite
118-6.1	--	1178	9E+4	150	75	894	±15	936	±17	+5	6.73	1.8	0.0703	0.8	1.44	1.9	0.149	1.8	0.9	spinel
118-6.2	--	4882	7E+4	638	16	913	±15	914	±13	+0	6.57	1.7	0.0695	0.7	1.46	1.8	0.152	1.7	0.9	spinel
118-6.3	--	710	1E+5	88.8	165	877	±15	942	±22	+7	6.86	1.8	0.0705	1.1	1.42	2.1	0.146	1.8	0.9	spinel
118-6.4	--	896	7E+4	113	81	883	±15	923	±18	+5	6.81	1.8	0.0698	0.9	1.41	2.0	0.147	1.8	0.9	spinel
118--7.1	--	1232	8E+4	161	70	912	±15	939	±30	+3	6.58	1.8	0.0704	1.5	1.47	2.3	0.152	1.8	0.8	spinel
118-7.2	--	2832	8E+4	362	28	895	±15	937	±11	+5	6.71	1.7	0.0703	0.5	1.44	1.8	0.149	1.7	1.0	spinel

Table 10: SHRIMP U-Pb-Th data for sample EG10-118

Spot	% $206Pb_c$	ppm U	ppm Th	ppm 206*	232Th /238U	(1) 206Pb /238U Age		(1) 207Pb /206Pb Age		% Dis-cor-dant	(1) 238U/ $206Pb^*$	±%	(1) $207Pb^*$ /$206Pb^*$	±%	(1) $207Pb^*$ /235U	±%	(1) $206Pb^*$ /238U	±%	err corr	Textural location
136-1.1	--	2893	102882	359	36.8	871	±17	938	±16	+8	6.92	2.1	0.0703	0.76	1.402	2.2	0.1446	2.1	0.94	matrix
136-1.2	--	3291	83621	396	26.3	845	±16	886	±13	+5	7.14	2.0	0.0686	0.64	1.325	2.1	0.1401	2.0	0.95	matrix
136-2.2	--	2253	82367	259	37.8	810	±16	874	±17	+8	7.47	2.1	0.0682	0.81	1.259	2.2	0.1339	2.1	0.93	matrix
136-2.1	--	546	131840	63.5	249.5	819	±17	868	±31	+6	7.38	2.2	0.0680	1.48	1.269	2.6	0.1355	2.2	0.83	matrix
136-2.3	--	739	113610	78.6	158.8	753	±16	883	±31	+16	8.07	2.2	0.0685	1.49	1.169	2.7	0.1238	2.2	0.83	matrix
136-3.1	--	2825	95139	358	34.8	886	±18	924	±14	+4	6.79	2.1	0.0698	0.70	1.419	2.2	0.1473	2.1	0.95	matrix
136-3.2	--	3852	94989	510	25.5	923	±18	936	±19	+1	6.49	2.1	0.0703	0.93	1.492	2.3	0.1540	2.1	0.91	matrix
136-3.3	--	3687	81839	482	22.9	913	±17	920	±11	+1	6.57	2.1	0.0697	0.53	1.463	2.1	0.1522	2.1	0.97	matrix
136-4.1	--	1764	101305	221	59.3	878	±17	924	±18	+5	6.86	2.1	0.0698	0.88	1.404	2.3	0.1458	2.1	0.92	matrix
136-4.2	--	1389	94345	178	70.2	898	±17	968	±19	+8	6.69	2.1	0.0714	0.91	1.470	2.3	0.1494	2.1	0.92	matrix
136-4.3	--	1657	90858	216	56.7	910	±18	919	±16	+1	6.59	2.1	0.0697	0.80	1.457	2.2	0.1517	2.1	0.93	matrix
136-5.1	--	2046	77638	266	39.2	909	±17	931	±15	+2	6.60	2.1	0.0701	0.75	1.464	2.2	0.1515	2.1	0.94	feldspar
136-5.2	--	1372	106497	179	80.2	912	±18	957	±18	+5	6.58	2.1	0.0710	0.87	1.487	2.2	0.1519	2.1	0.92	feldspar
136-5.3	--	730	151135	96.8	213.8	925	±18	944	±22	+2	6.48	2.1	0.0705	1.09	1.501	2.4	0.1543	2.1	0.89	feldspar
136-5.4	--	984	122237	130	128.4	922	±18	972	±21	+5	6.50	2.1	0.0715	1.04	1.515	2.3	0.1537	2.1	0.90	feldspar
136-5.5	--	1191	100766	153	87.4	895	±17	934	±20	+4	6.71	2.1	0.0702	0.96	1.442	2.3	0.1490	2.1	0.91	feldspar
136-5.7	--	883	135371	114	158.4	902	±18	915	±24	+1	6.66	2.1	0.0695	1.16	1.440	2.4	0.1502	2.1	0.88	feldspar
136-6.1	--	4724	88167	600	19.3	889	±17	967	±10	+9	6.76	2.0	0.0713	0.51	1.454	2.1	0.1478	2.0	0.97	matrix

Table 11: SHRIMP U-Pb-Th data for sample EG10-136

Sample	Method	Upper Intercept	Lower Intercept	6/U238 Weighted Av	Uncertainty	Pb207/Pb206 Weighted Average	Uncertainty
EG10-063	LA-ICPMS	1013 ± 42	474 ± 230	919	16	974.7	8.6
EG10-AK3	SHRIMP U-Pb-Th	989 ± 21	318 ± 310	942	12	973	6.6
EG10-AK5	LA-ICPMS	943 ± 39	680 ± 68	885	15	885	15
EG10-AK5: older population	SHRIMP U-Pb-Th			929	7.2	933	20
EG10-AK5: symplectite	SHRIMP U-Pb-Th	1023 ± 210	639±92	821	27	860	30
EG10-087	LA-ICPMS	N/A	N/A	946.3	8.5	965	17
EG10-BXX	LA-ICPMS	938 ± 140	580 ± 320	859	41	877	42
EG10-BXX- within garnet grains	LA-ICPMS	N/A	N/A	930	18	938	23
EG10-BXX: matrix	LA-ICPMS	890 ± 370	523 ± 630	720	80	763	68
EG10-118	SHRIMP U-Pb-Th	1003 ± 49	613 ± 83	821	23	908	39
EG10-136	SHRIMP U-Pb-Th	988 ± 48	579 ± 150	898	12	928	14

Table 12: Summary of geochronology data

			Average T (°C) depending on pressure (calculated from an estimate of pressure at 9 kbar)					
Sample/garnet grain	**Map/Transect Fig. no.**	**Garnet Diametre**	**7.5 kbars**	**8.2 kbars**	**8.9 kbars**	**9.6 kbars**	**10.3 kbars**	**11.0 kbars**
Upright foliation								
EG10-087 core	12	4300 µm	588	591	593	598	601	604
EG10-087 rims	12	4300 µm	473	475	479	481	484	486
Flat foliation								
EG10-110a core	13	3050 µm	748	752	755	758	761	768
EG10-110b core	14. b	4020 µm	779	783	787	791	795	799
EG10-110c core	14.a	3000 µm	649	653	656	659	663	666
EG10-110a rims	13	3050 µm	681	684	688	691	694	700
EG10-110b rims	14. b	4020 µm	616	619	623	626	629	632
EG10-110c rims	14.a	3000 µm	500	502	506	508	511	514
Felsic intrusive								
EG10-BXX1 cores†	10	2200 µm	684	687	691	694	698	701
EG10-BXX2 cores†	11	1350 µm	667	671	674	678	681	685
EG10-BXX1 rims†	10	2200 µm	569	572	575	578	581	584
EG10-BXX2 rims†	11	1350 µm	565	568	571	574	577	580

† This sample has a calculated pseudosection

Table 13: Conventional thermobarometric estimates calculated

Garnet	BXX1	BXX2	87	110
Peak T	**900**	**900**	**900**	**900**
End T	**570**	**565**	**485**	**690**
Rate	0.05	0.05	0.05	0.05
Duration	6600	6700	8300	4200
End age	-5660	-5760	-7360	-3260
Rate	0.1	0.1	0.1	0.1
Duration	3300	3350	4150	2100
End age	-2360	-2410	-3210	-1160
Rate	1	1	1	1
Duration	330	335	415	210
End age	610	605	525	730
Rate	2	2	2	2
Duration	165	167.5	207.5	105
End age	775	772.5	732.5	835
Rate	3	3	3	3
Duration	110	111.667	138.333	70
End age	830	828.333	801.667	870
Rate	4	4	4	4
Duration	82.5	83.75	103.75	52.5
End age	857.5	856.25	836.25	887.5
Rate	5	5	5	5
Duration	66	67	83	42
End age	874	873	857	898

Table 14: Calculations of rates from diffusion based modelling

Sample	Rock type	Structural feature	*In situ* SHRIMP U/Pb/Th geochronology	*In situ* LAICP-MS U/Pb geochronology	Conventional Thermo-barometry peak temperature estimate	Phase diagram peak P (kbars)	Phase diagram peak T (°C)	Cooling rate estimation
EG10-063	Migmatite	Upright foliation	974.7 ± 8.6 Ma	N/A	N/A	> 8.5	> 750	N/A
EG10-AK3	Mg-Al granulite	Upright foliation	973 ± 6.6 Ma	N/A	N/A	N/A (but from same location as sample EG10-AK5)		N/A
EG10-AK5	Mg-Al granulite	Upright foliation	N/A	885 ± 15 Ma	N/A	1000 - 1050	12	N/A
EG10-087	Garnet-biotite schist	Upright foliation	N/A	965 ± 17 Ma	600 °C	N/A		0.01 - 5
EG10-BXX	Recrystallised granite	Upright foliation	N/A	938 ± 23 Ma	700 °C	10	880	0.05 - 0.08
EG10-110	Biotite-garnet schist	Flat foliation	Contained insufficient monazites or zircons		760 °C	N/A		0.01 - 5
EG10-118	Mg-Al granulite	Flat foliation	928 ± 14 Ma	N/A	N/A	N/A		N/A
EG10-136	Mg-Al granulite	Flat foliation	922 ± 12 Ma	N/A	N/A	10 kbar	950 - 1000	N/A

Table 15: Summary of results

	Osm bulk c (wt%)*	Mine (wt%)	Difference (%)
K2O	3.48	1.92	-1.56
Na2O	0.76	0.86	0.1
MgO	5.95	8.32	2.37
Al2O3	26.35	40.63	14.28
FeO	3.54	3	-0.54
Fe2O3	5.9	6.61	0.71
SiO2	53.24	42.62	-10.62
	Average variation from mean %		0.68
	* From Webmineral.com		

Bulk Comp.	H2O	SiO2	Al2O3	CaO	MgO	FeO	K2O	Na2O	TiO2	O	**Total**
	0	42.62	40.63	0.43	8.32	3	1.92	0.86	0.26	0.85	**98.88**

Table 16: Calculating composition of potential osumilite grain in sample EG10-AK5

Sample Number	K	Th	U	?Time (Ma)	heat from U at t	heat from Th at t	heat from K at t	**total heat production at time t**
EG10-AK1	6.05	90	4.1	1000	1.24	6.76	0.88	8.88
EG10-AK2	1.67	32	1.2	1000	0.36	2.41	0.24	3.01
EG10-AK3	0.71	80	4.3	1000	1.30	6.01	0.10	7.41
EG10-AK4	3.39	55	6.5	1000	1.96	4.13	0.49	6.59
EG10-AK5	2.37	38	4	1000	1.21	2.86	0.34	4.41
EG10-AK6	3.66	35.5	0.9	1000	0.27	2.67	0.53	3.47
EG10-AK7	2.3	65	2.6	1000	0.78	4.89	0.33	6.00
EG10-AK8	2.97	55	7	1000	2.11	4.13	0.43	6.68
EG10-063	1.19	27	1.6	1000	0.48	2.03	0.17	2.68
EG10-064	2.34	10.5	1.8	1000	0.54	0.79	0.34	1.67
EG10-066	2.63	13	5	1000	1.51	0.98	0.38	2.87
EG10-118	1.2	31	1.8	1000	0.54	2.33	0.17	3.05
EG10-119	1.65	55	1.1	1000	0.33	4.13	0.24	4.70
EG10-136	2.81	15.5	1	1000	0.30	1.17	0.41	1.87
EG10-137	3.73	16.5	1.6	1000	0.48	1.24	0.54	2.26
EG10-140	2.74	10	0.6	1000	0.18	0.75	0.40	1.33
EG10-106	0.32	75	4.1	1000	1.24	5.64	0.05	6.92
EG10-BXX	3.24	11.5	0.3	1000	0.09	0.86	0.47	1.42
EG10-120	3.05	1.7	0.2	1000	0.06	0.13	0.44	0.63
							all depends on density above 4	

Table 17: Heat production calculations from bulk rock mineral chemistry in the Eastern Ghats using a formula from Turcotte & Schubert (1982). Yellow samples were the focus of this study.

	whole Fe										BHN2c standard									
	AK-1	AK-2	AK-3	AK-4	AK-5	AK-6	AK-7	AK-8	EG10-063	EG10-064	**EG10-066**	EG10-118	EG10-119	EG10-136	EG10-137	EG10-140	EG10-106	EG10-BXX	EG10-120	MXX
SiO2	40.4	48.6	43.3	59.4	56.6	77.6	48.7	40.7	67.7	72.4	52.8	61.6	69.3	46.4	52.9	47.2	50.8	67.1	69.6	57.4
TiO2	0.425	0.26	0.33	0.815	0.88	0.255	0.42	0.355	1.655	0.475	1.3	0.825	0.56	1.21	0.905	1.165	1.79	1.07	0.74	0.865
Al2O3	25.9	18.2	23.7	14.9	15.7	10.6	16.3	22.7	16.1	16.8	16.7	18.4	14.1	24.3	21.9	24.1	28.1	14.4	15.2	22.3
Cr	<20	<20	<20	310	500	<20	<20	<20	115	50	85	100	55	130	85	140	165	45	55	105
Fe2O3	2.53	10.9	10.9	7.24	9.63	2.85	8.1	8.94	11.2	1.66	10.2	11.7	8.18	14.3	11	14.6	16.8	7.31	4.72	7.75
MnO	<0.01	0.12	0.19	0.05	0.06	0.02	0.09	0.04	0.1	0.01	0.17	0.2	0.16	0.14	0.12	0.16	0.25	0.13	0.04	0.04
MgO	19.2	18.2	19.3	9.35	12.7	1.6	22.7	21.2	1.69	2.98	4.61	5.02	3.95	6.76	7.31	6.79	2.67	1.67	1.77	4.19
Zn	43	90	75	38	48	7.5	80	50	130	16.5	135	105	47.5	80	50	120	105	105	55	90
CaO	0.96	1.49	1.08	1	0.89	0.41	0.71	0.64	0.43	0.38	8.89	0.83	0.85	1.81	0.9	1.96	0.15	3.83	2.2	0.64
Na2O	1.27	1.34	1.16	2.33	1.88	2.17	1.05	0.67	0.1	2.46	2.65	0.67	0.89	1.99	1.41	2.07	0.02	1.64	2.46	1.12
K2O	6.05	1.67	0.71	3.39	2.37	3.66	2.3	2.97	1.19	2.34	2.63	1.2	1.65	2.81	3.73	2.74	0.32	3.24	3.05	4.19
LOI	1.28	-0.01	-0.08	0.17	0.05	0.34	0.34	1.33	0.7	0.7	-0.1	0.08	0.55	0.8	0.23	-0.26	-0.38	<0.01	0.27	0.74
	Fe3+										BHN2c standard									
	AK-1	AK-2	AK-3	AK-4	AK-5	AK-6	AK-7	AK-8	EG10-063	EG10-064	**EG10-066**	EG10-118	EG10-119	EG10-136	EG10-137	EG10-140	EG10-106	EG10-BXX	EG10-120	MXX
SiO2	40.4	48.6	43.3	59.4	56.6	77.6	48.7	40.7	67.7	72.4	52.8	61.6	69.3	46.4	52.9	47.2	50.8	67.1	69.6	57.4
TiO2	0.425	0.26	0.33	0.815	0.88	0.255	0.42	0.355	1.655	0.475	1.3	0.825	0.56	1.21	0.905	1.165	1.79	1.07	0.74	0.865
Al2O3	25.9	18.2	23.7	14.9	15.7	10.6	16.3	22.7	16.1	16.8	16.7	18.4	14.1	24.3	21.9	24.1	28.1	14.4	15.2	22.3
Cr2O3	0	0	0	0.045308	0.073077	0	0	0	0.016808	0.007308	0.012423	0.014615	0.008038	0.019	0.012423	0.020462	0.024115	0.006577	0.008038	0.015346
Fe2O3	2.53	10.9	10.9	7.24	9.63	2.85	8.1	8.94	11.2	1.66	10.2	11.7	8.18	14.3	11	14.6	16.8	7.31	4.72	7.75
MnO	0	0.12	0.19	0.05	0.06	0.02	0.09	0.04	0.1	0.01	0.17	0.2	0.16	0.14	0.12	0.16	0.25	0.13	0.04	0.04
MgO	19.2	18.2	19.3	9.35	12.7	1.6	22.7	21.2	1.69	2.98	4.61	5.02	3.95	6.76	7.31	6.79	2.67	1.67	1.77	4.19
ZnO	0.002676	0.005601	0.004668	0.002365	0.002987	0.000467	0.004979	0.003112	0.008091	0.001027	0.008402	0.006535	0.002956	0.004979	0.003112	0.007468	0.006535	0.006535	0.003423	0.005601
CaO	0.96	1.49	1.08	1	0.89	0.41	0.71	0.64	0.43	0.38	8.89	0.83	0.85	1.81	0.9	1.96	0.15	3.83	2.2	0.64
Na2O	1.27	1.34	1.16	2.33	1.88	2.17	1.05	0.67	0.1	2.46	2.65	0.67	0.89	1.99	1.41	2.07	0.02	1.64	2.46	1.12
K2O	6.05	1.67	0.71	3.39	2.37	3.66	2.3	2.97	1.19	2.34	2.63	1.2	1.65	2.81	3.73	2.74	0.32	3.24	3.05	4.19
LOI	1.28	-0.01	-0.08	0.17	0.05	0.34	0.34	1.33	0.7	0.7	-0.1	0.08	0.55	0.8	0.23	-0.26	-0.38	<0.01	0.27	0.74

Table 18: Bulk composition data for analysed samples

FIGURES

Figure 1

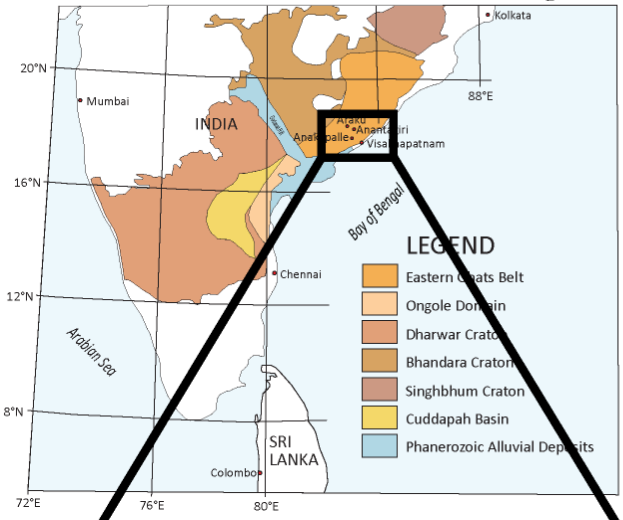

Figure 2
Eastern Ghats Province

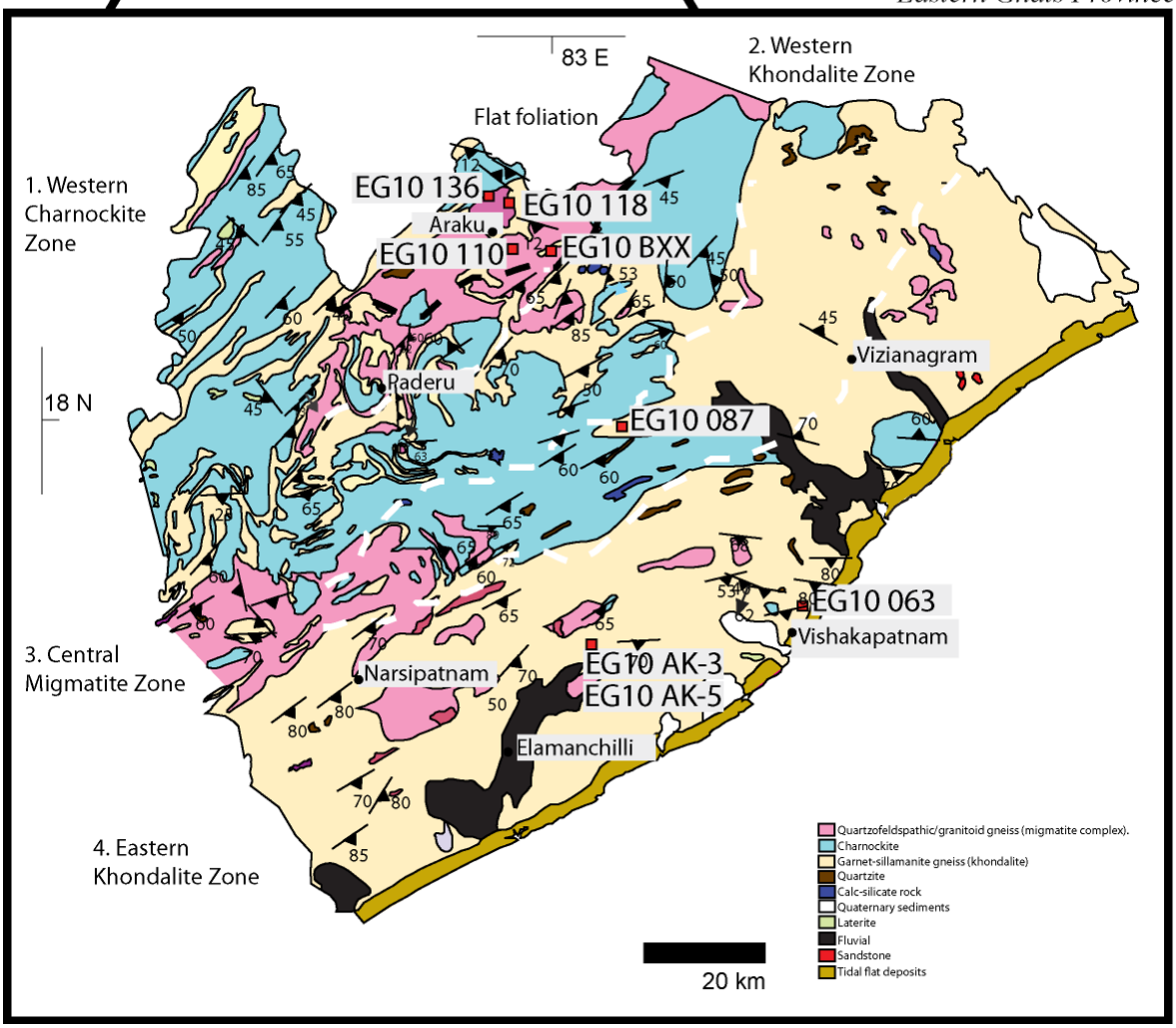

Figure 3

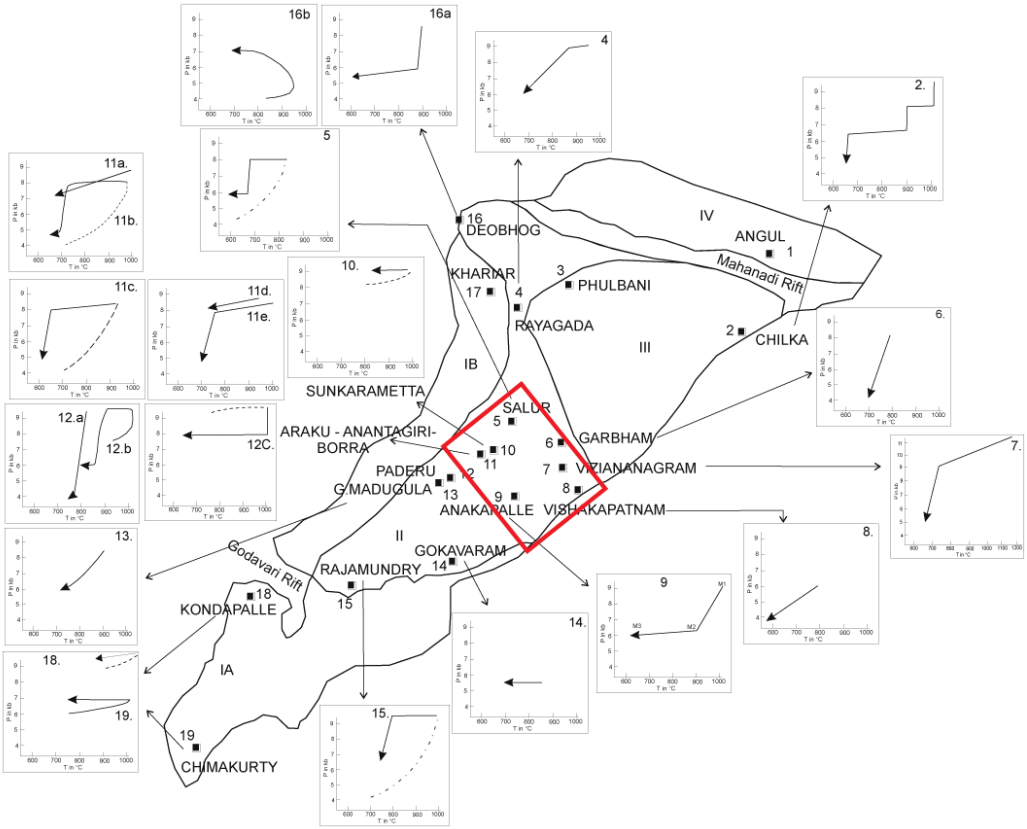

Figure 4

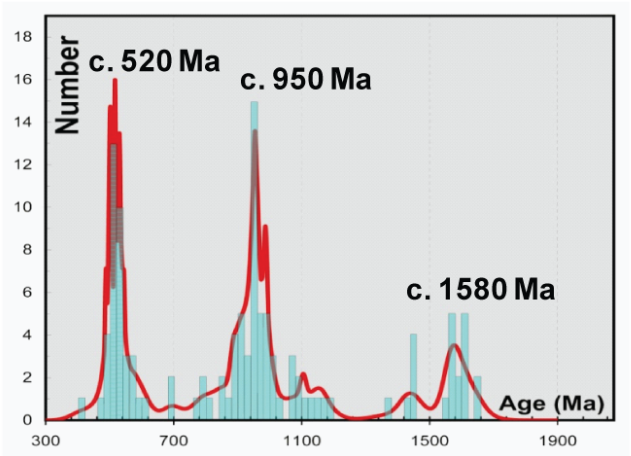

Figure 5

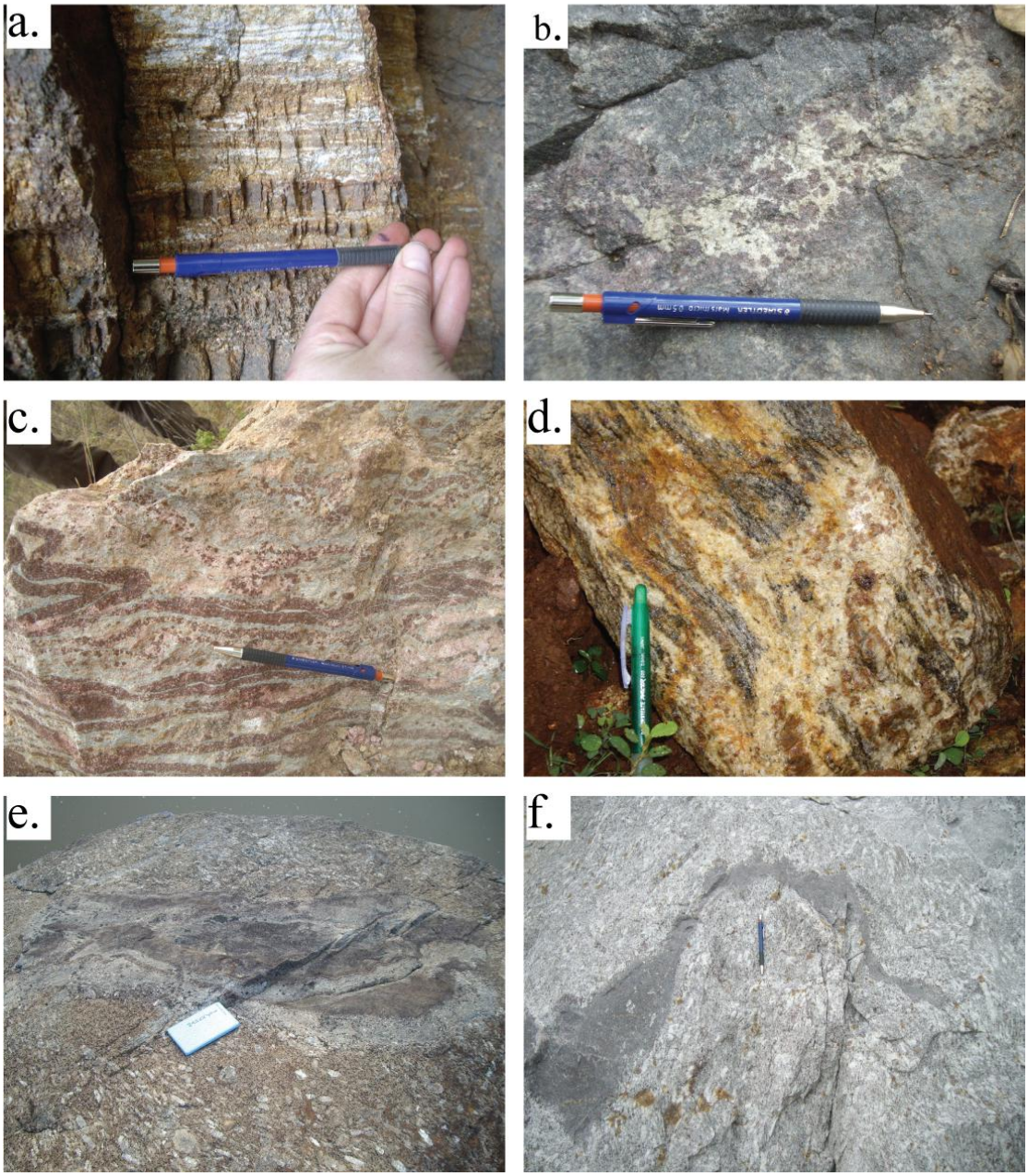

Figure 6

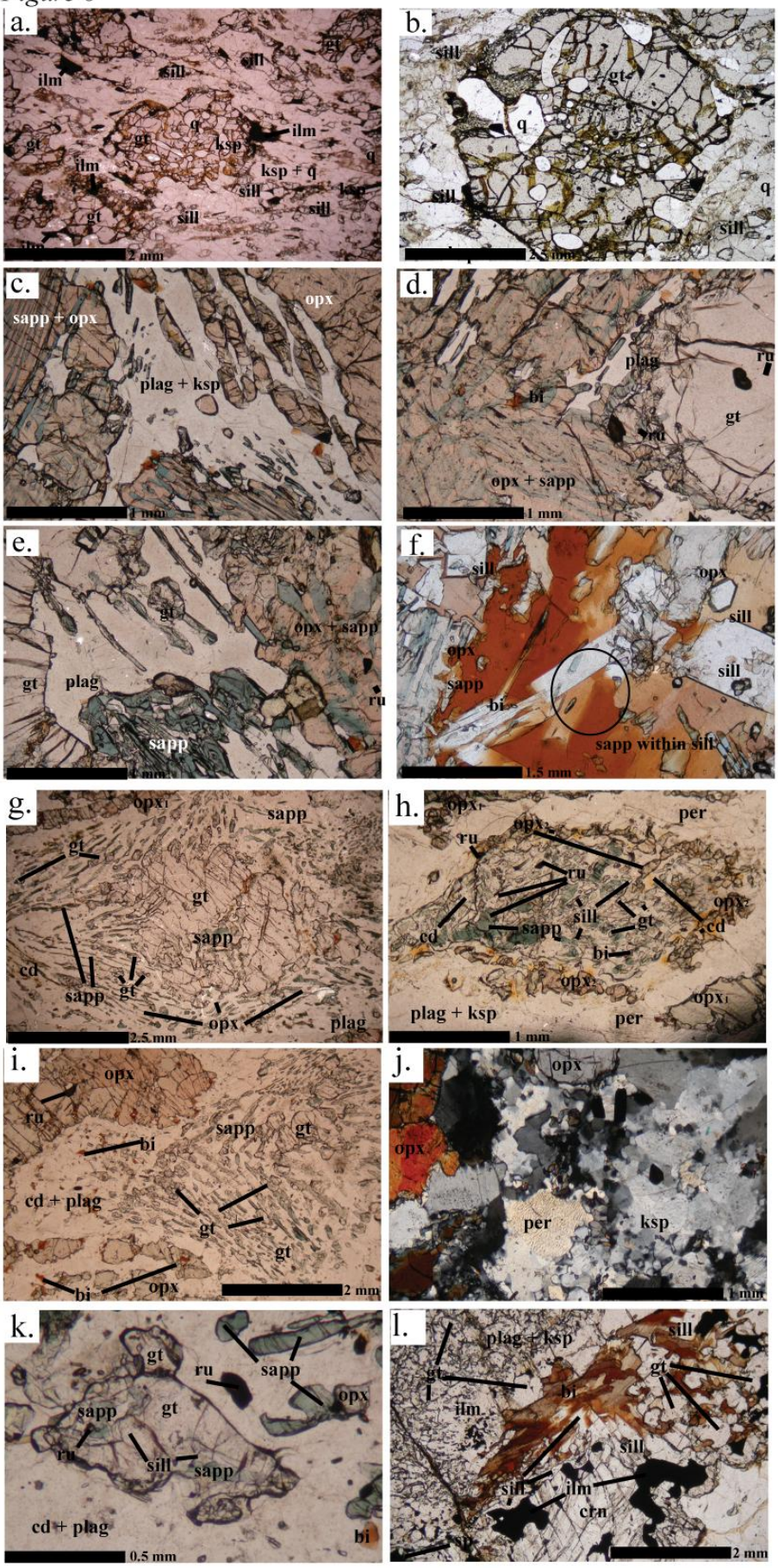
a.
ilm
sill
sill
gt
q
ilm
gt
gt
ksp
ilm
ksp + q
q
sill
sill
gt
sill
2 mm
b.
sill
gt
q
sill
q
sill
c.
opx
sapp + opx
plag + ksp
1 mm
d.
plag
ru
bi
gt
ru
opx + sapp
1 mm
e.
gt
opx + sapp
gt
plag
ru
sapp
1 mm
f.
sill
opx
sill
opx
sapp
sill
bi
sapp within sill
1.5 mm
g.
opx
sapp
gt
gt
gt
sapp
cd
sapp
gt
opx
plag
2.5 mm
h.
opx
opx
per
ru
ru
opx
sill
gt
cd
cd
sapp
bi
opx
plag + ksp
per
opx
1 mm
i.
opx
ru
sapp
gt
bi
cd + plag
gt
gt
bi
opx
2 mm
j.
opx
opx
per
ksp
1 mm
k.
gt
ru
sapp
opx
sapp
gt
ru
sill
sapp
cd + plag
bi
0.5 mm
l.
plag + ksp
sill
gt
gt
bi
ilm
sill
sill
ilm
crn
2 mm

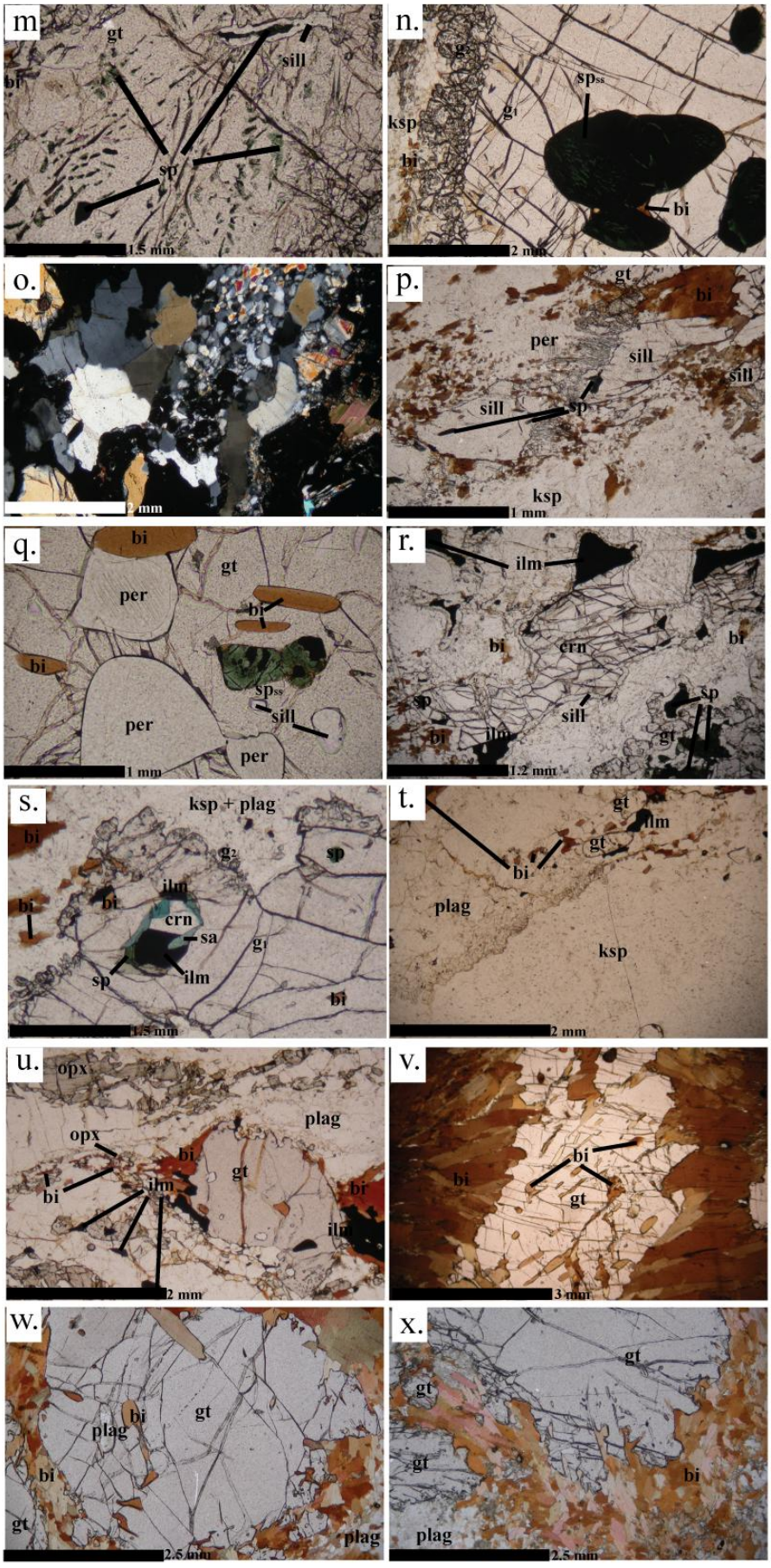
m.
gt
sill
bi
sp
1.5 mm
n.
g
spss
g1
ksp
bi
bi
2 mm
o.
2 mm
p.
gt
bi
per
sill
sill
sill
sp
ksp
1 mm
q.
bi
gt
per
bi
bi
spss
sill
per
per
1 mm
r.
ilm
bi
crn
bi
sp
sill
sp
bi
ilm
gt
1.2 mm
s.
ksp + plag
bi
g2
sp
ilm
bi
bi
crn
sa
g1
sp
ilm
bi
1.5 mm
t.
gt
ilm
gt
bi
plag
ksp
2 mm
u.
opx
plag
opx
bi
gt
bi
bi
ilm
bi
ilm
2 mm
v.
bi
bi
gt
3 mm
w.
plag
bi
gt
bi
gt
plag
2.5 mm
x.
gt
gt
gt
bi
plag
2.5 mm

Figure 7 Sample EG10-AK5

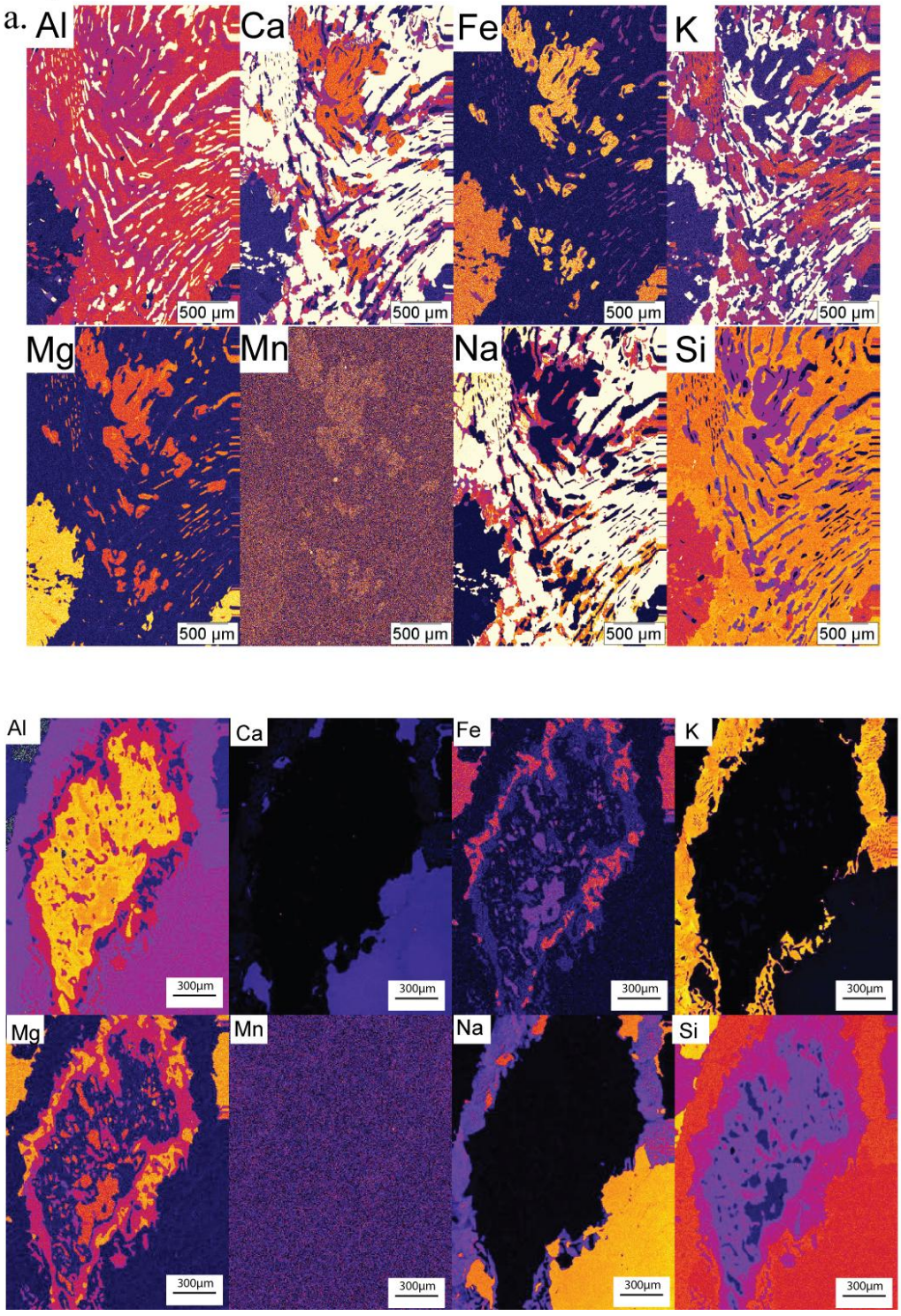

Figure 8 Sample EG10-AK3

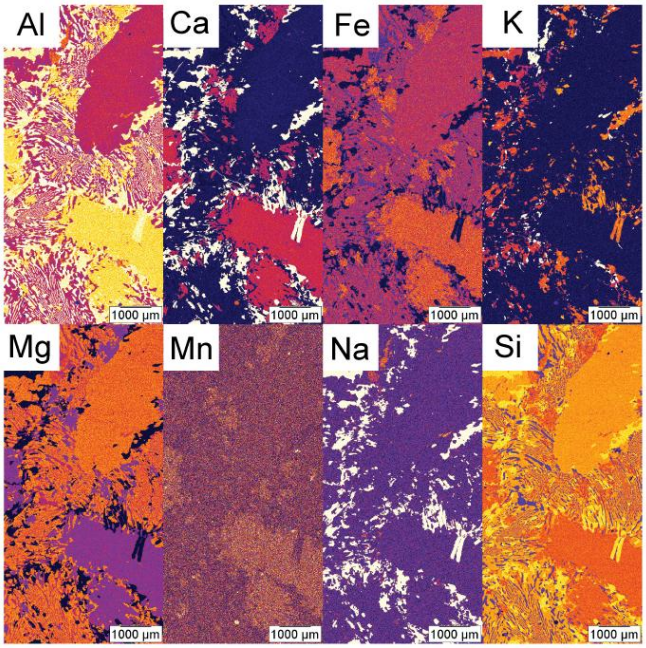

Figure 9 Sample EG10 118

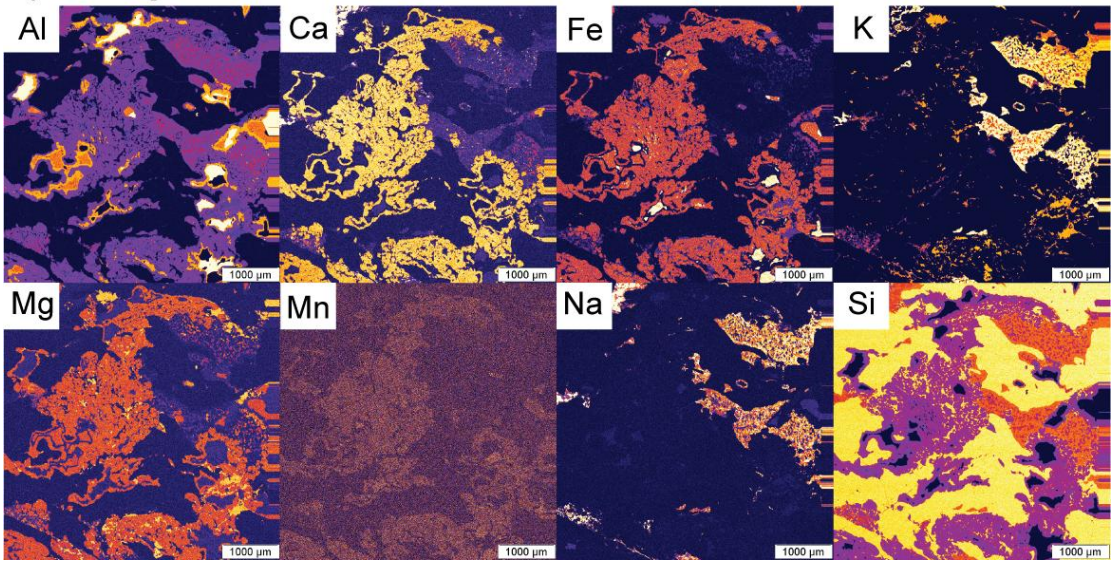

Figure 10: Sample EG10-BXX

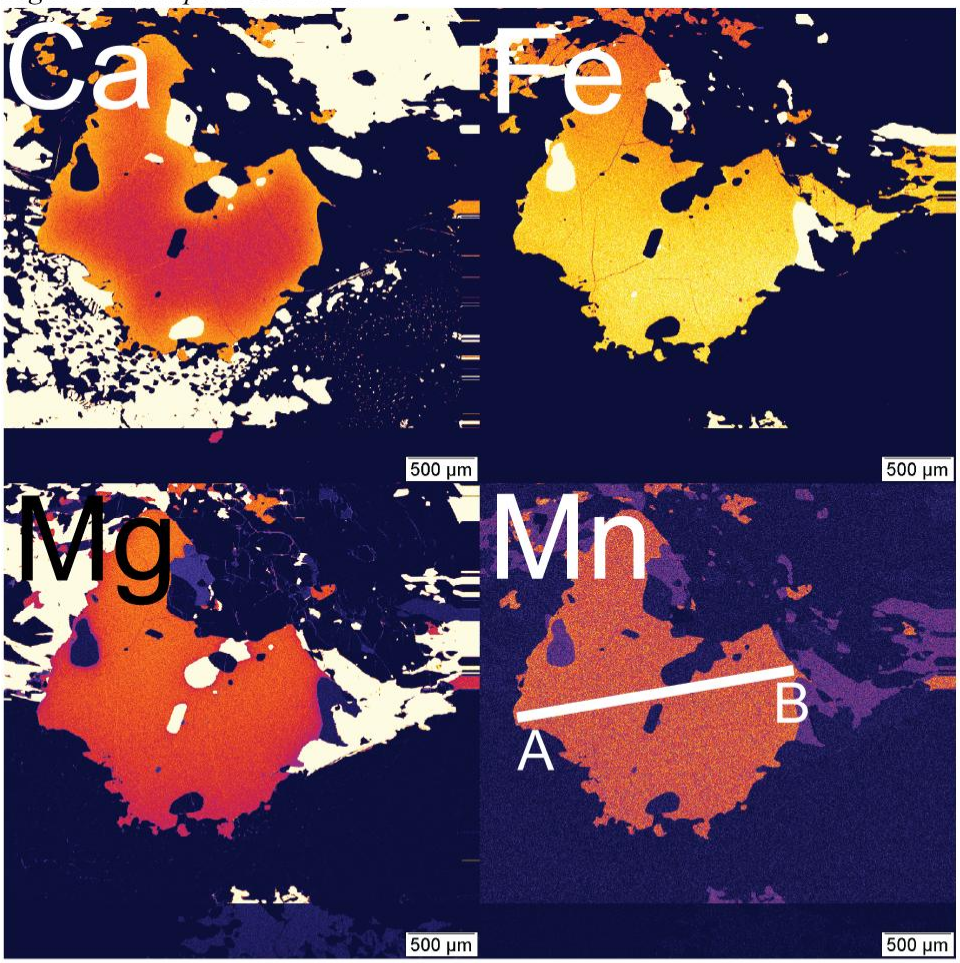

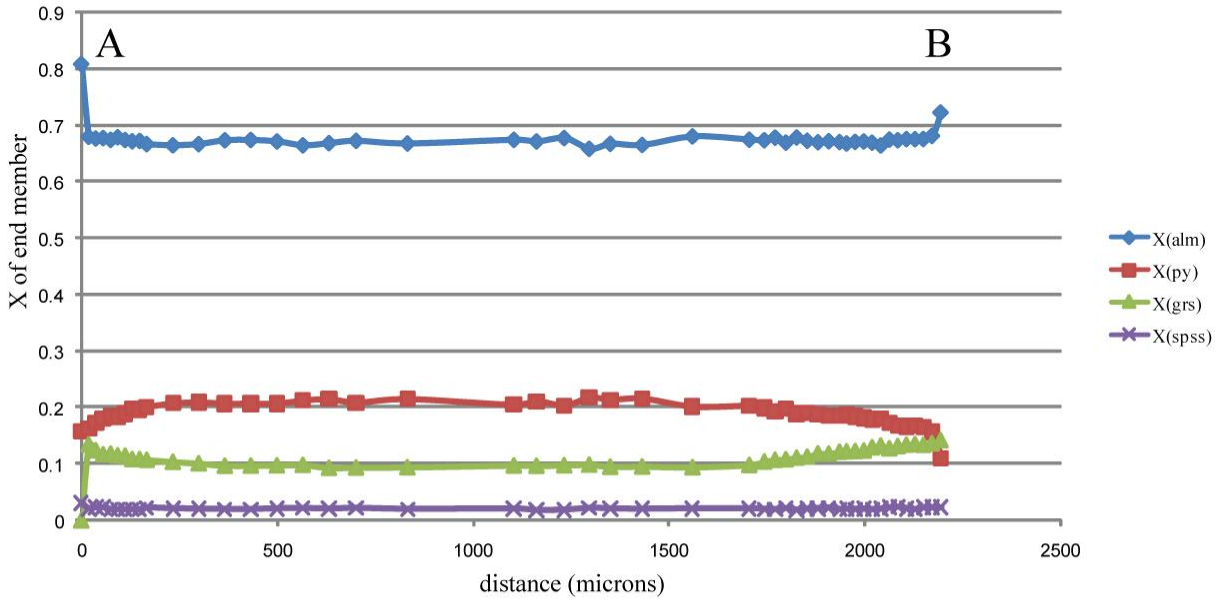

Figure 11 Sample EG10-BXX Garnet 2

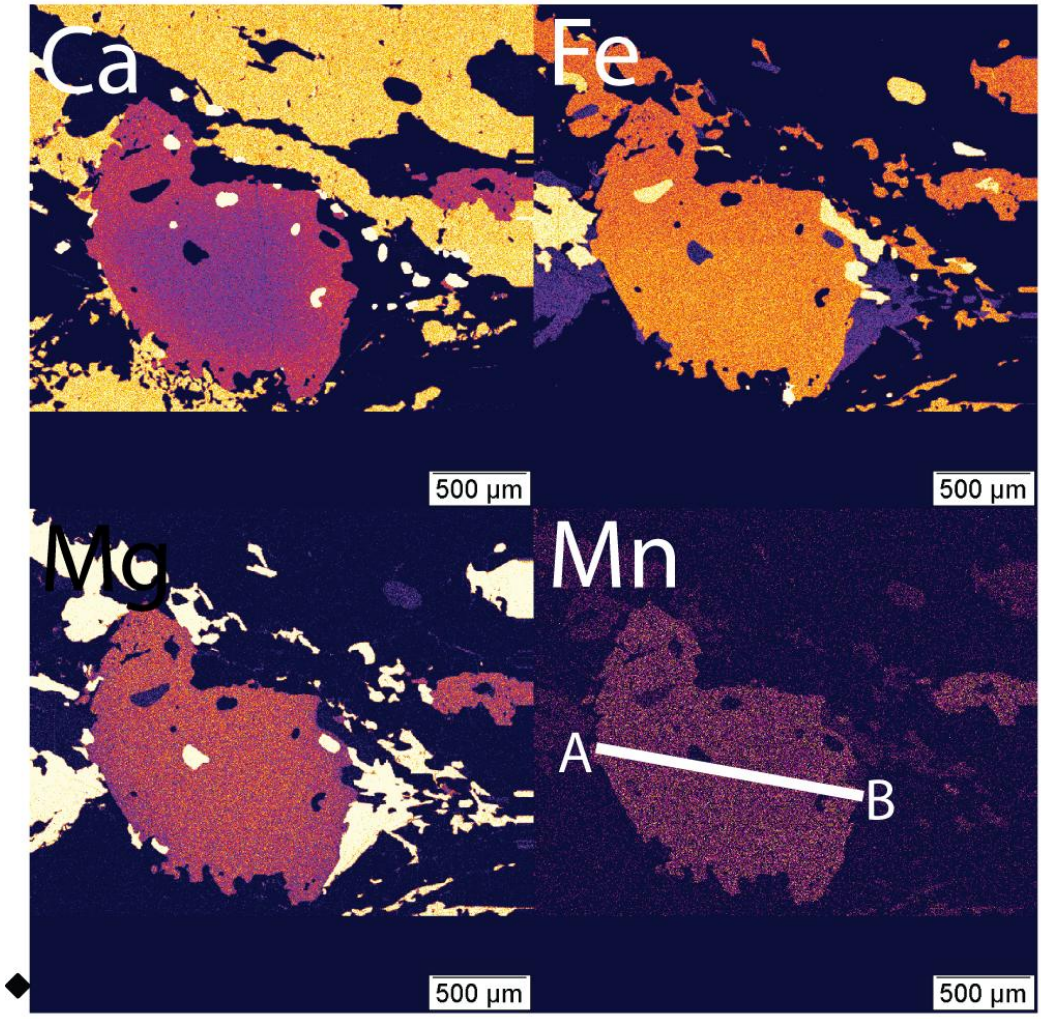

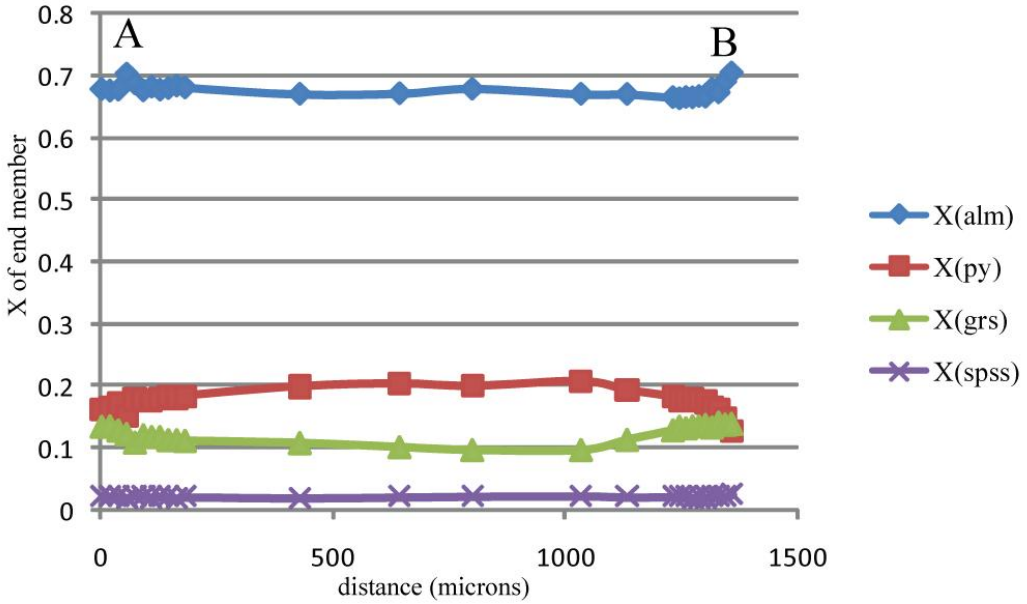

Figure 12 EG10-087

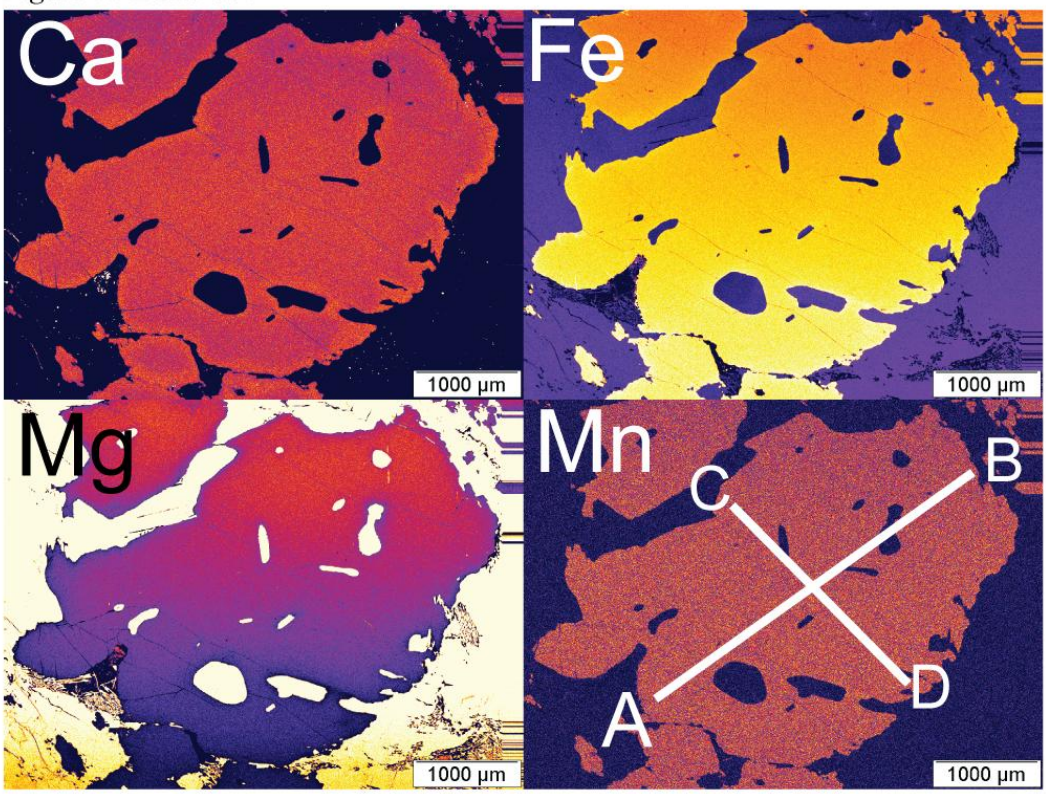

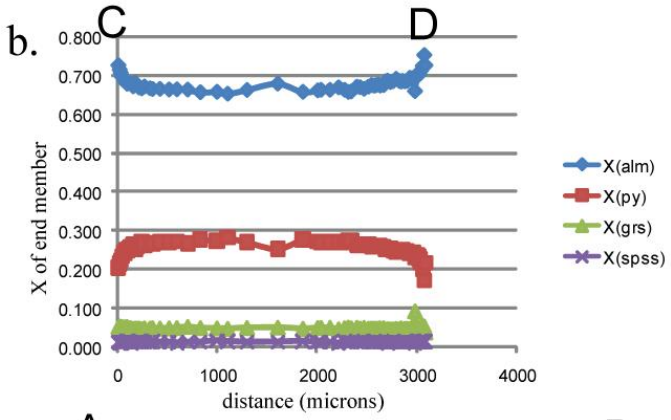

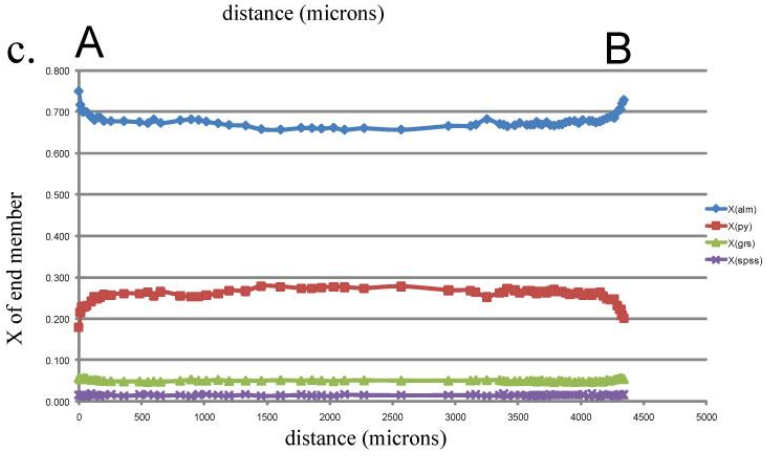

Figure 13 Sample EG10-110 Garnet A

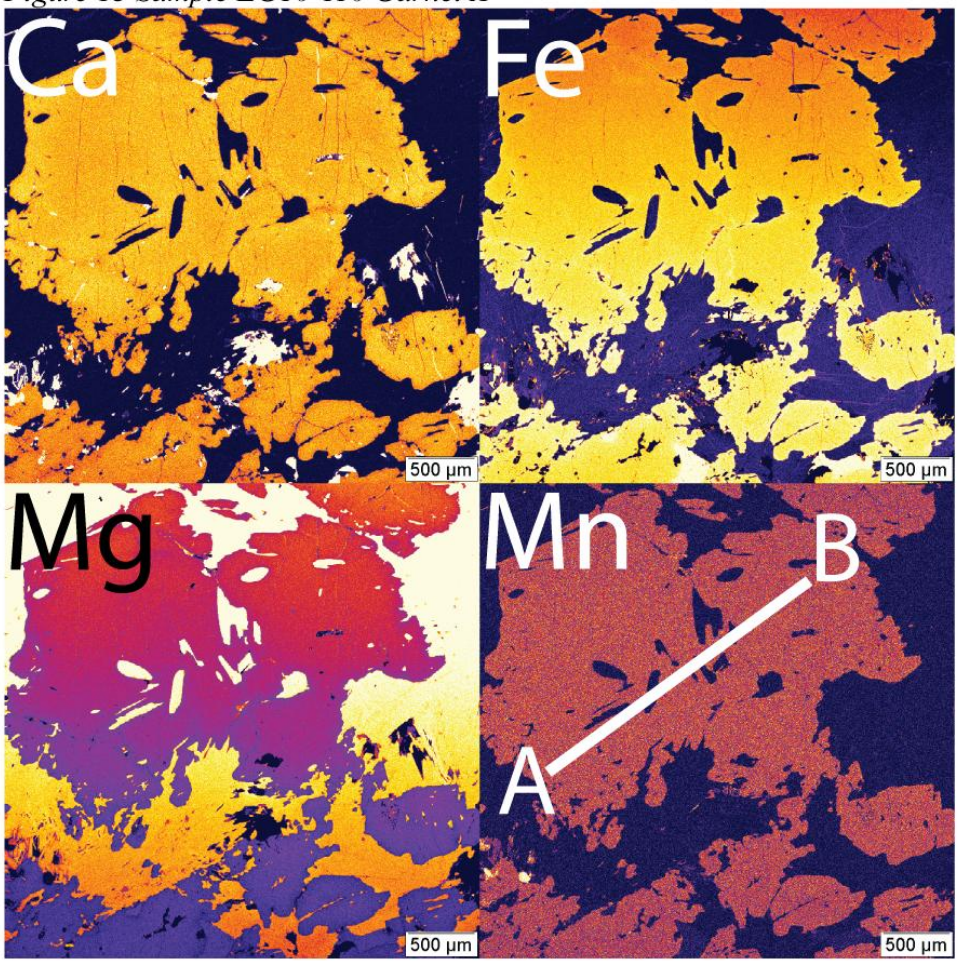

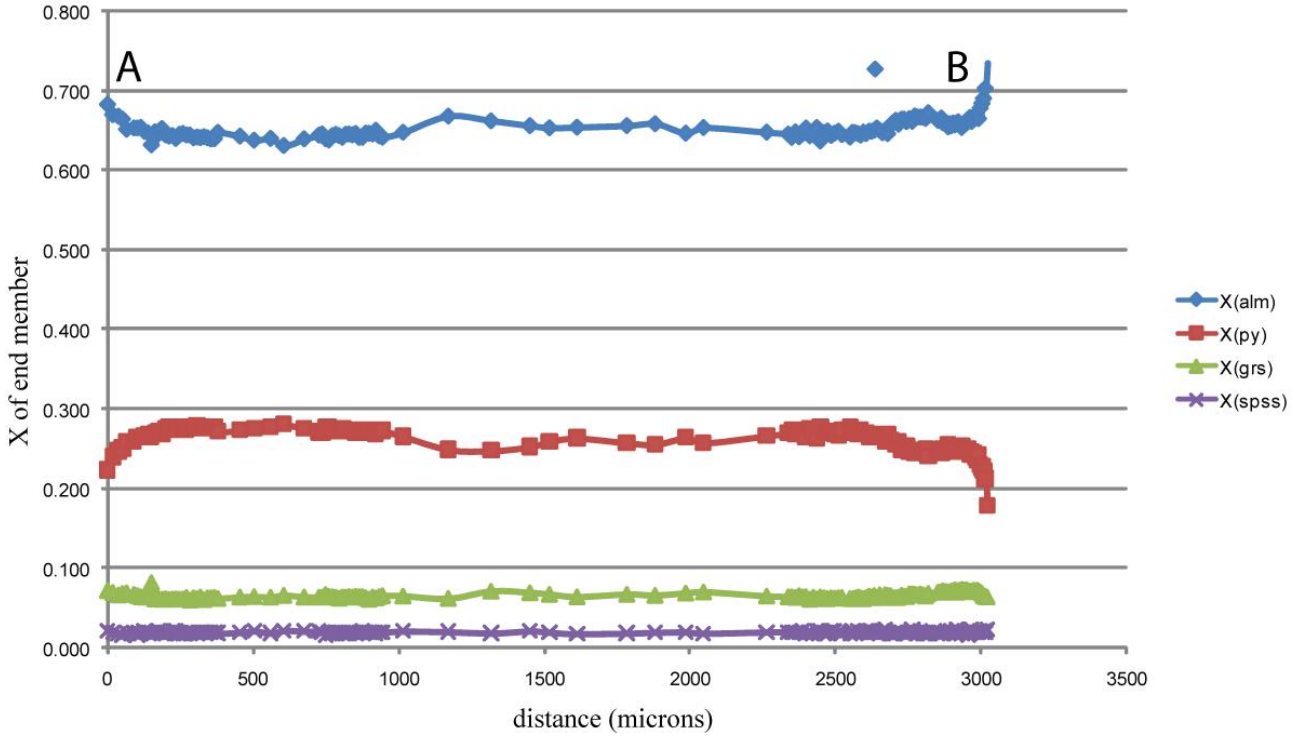

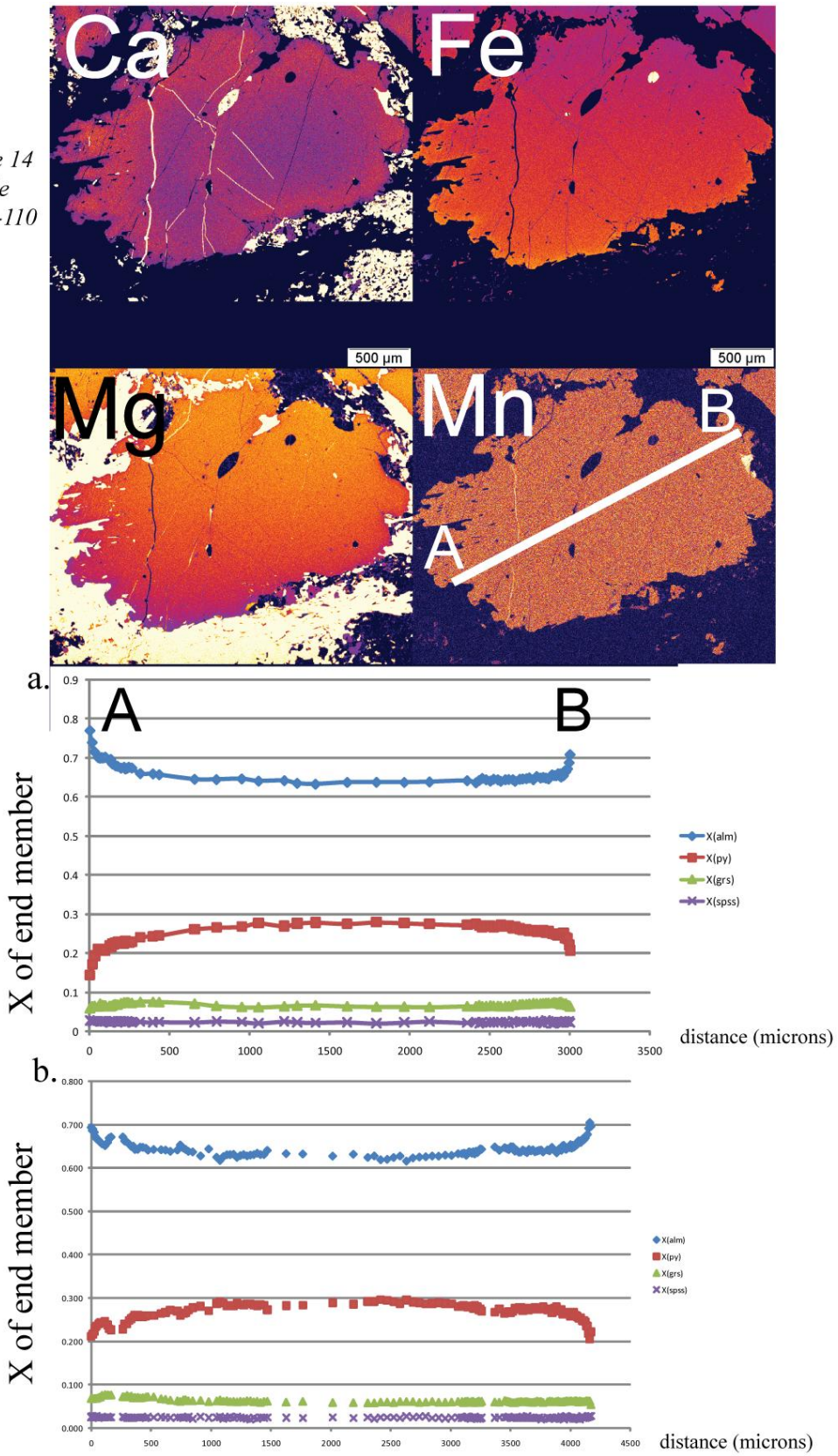

Figure 14
Sample
EG10-110

Figure 15 Sample EG10-AK5

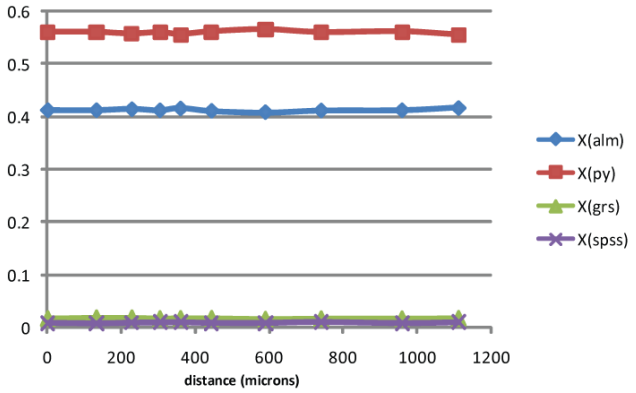

Figure 16 Sample EG10-AK5

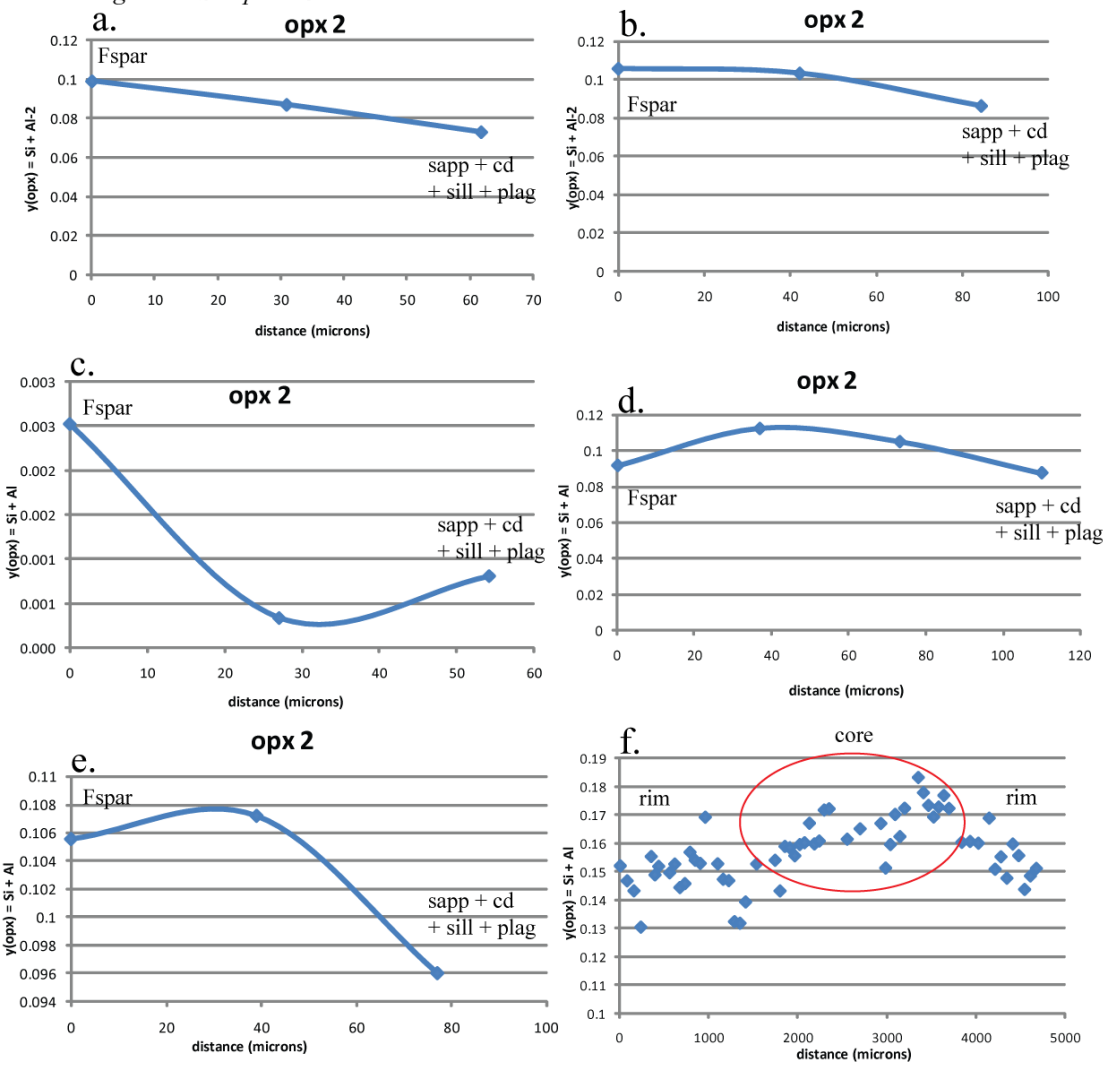

Figure 17

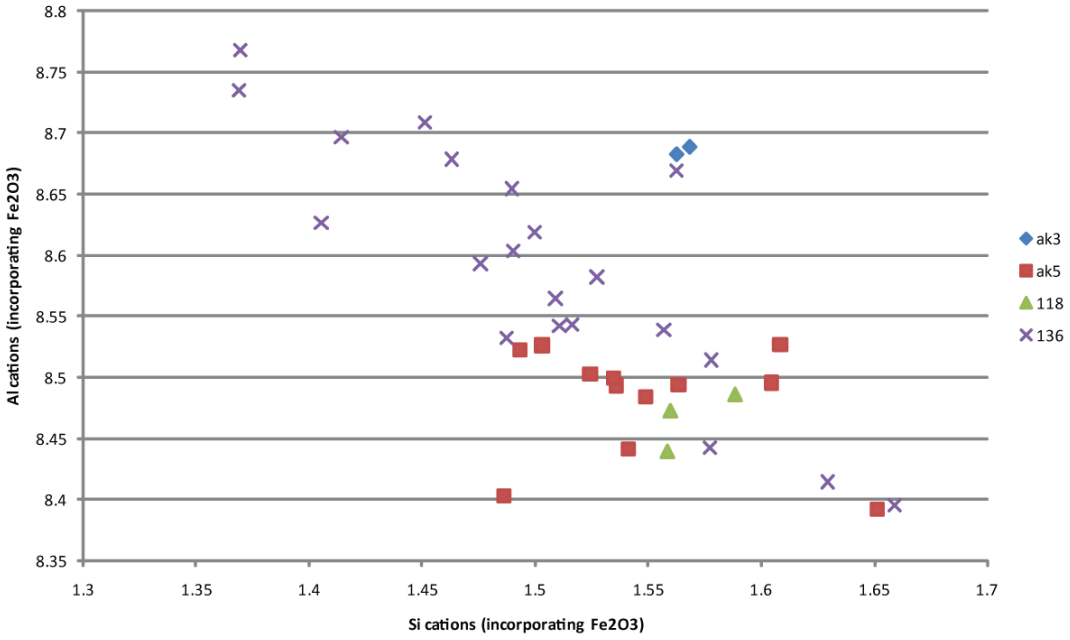

Figure 18 EG10-AK5

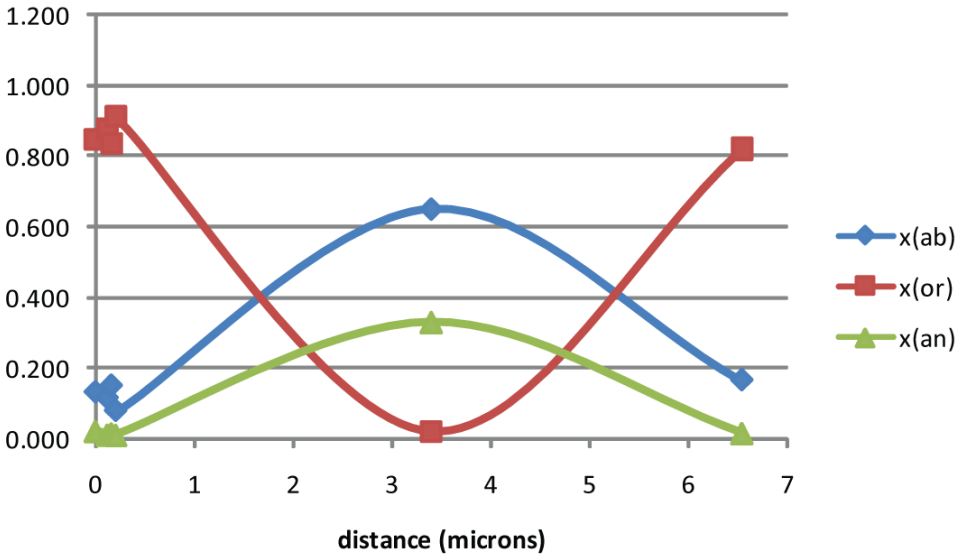

Figure 19

a.

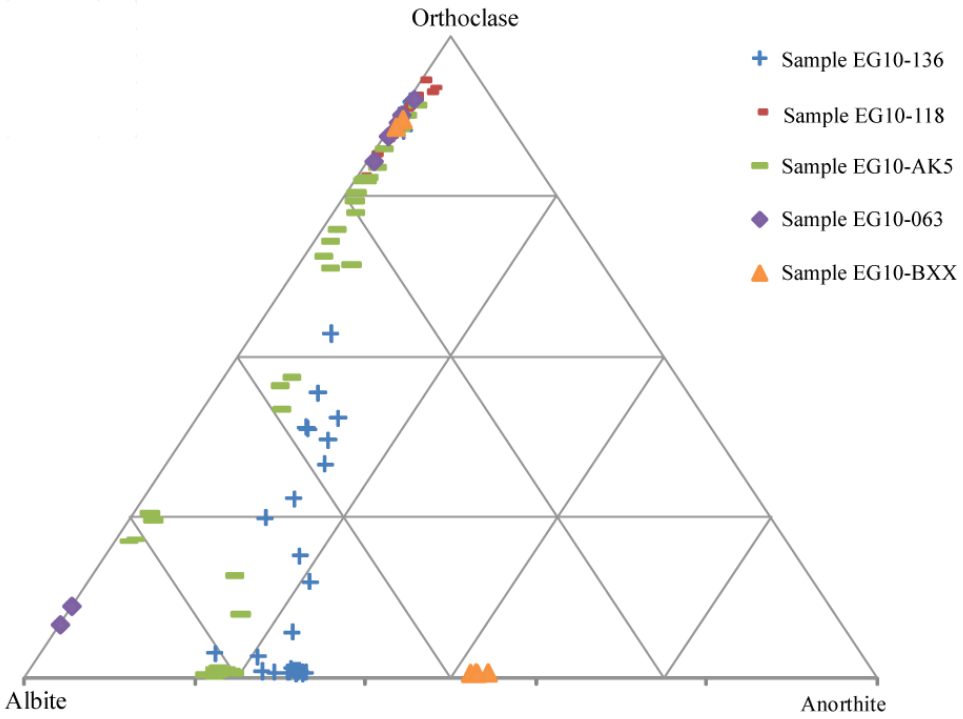

b. *Sample EG10-136*

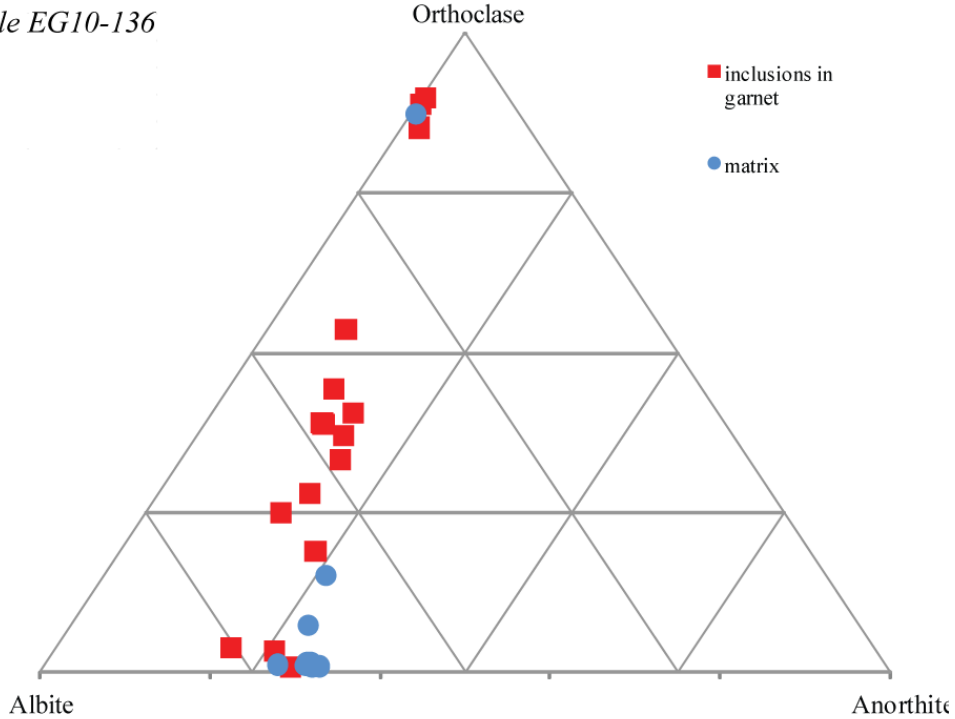

Figure 20

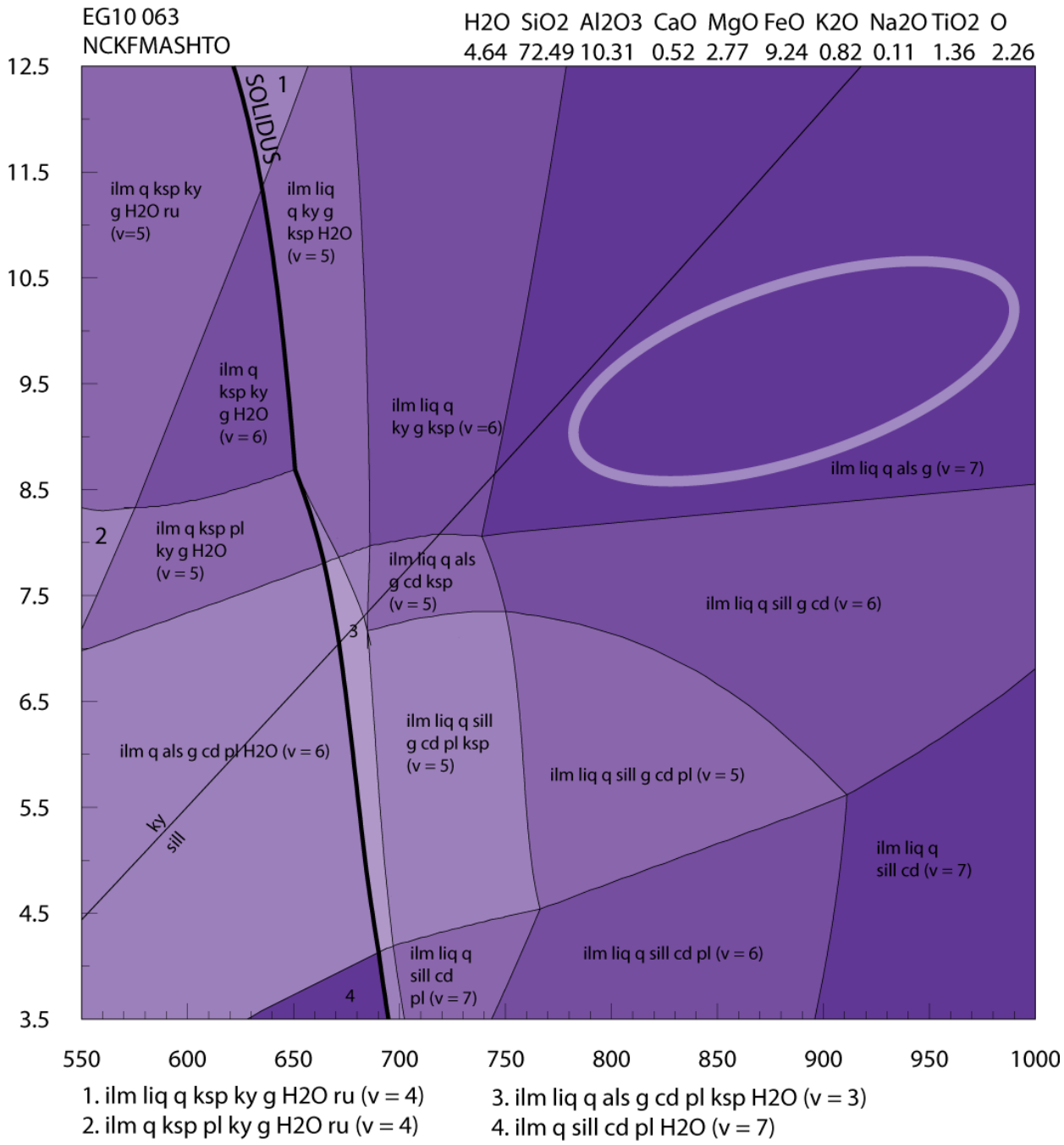
EG10 063
NCKFMASHTO
H2O SiO2 Al2O3 CaO MgO FeO K2O Na2O TiO2 O
4.64 72.49 10.31 0.52 2.77 9.24 0.82 0.11 1.36 2.26
SOLIDUS
1
2
3
4
ilm q ksp ky g H2O ru (v=5)
ilm liq q ky g ksp H2O (v = 5)
ilm q ksp ky g H2O (v = 6)
ilm liq q ky g ksp (v =6)
ilm liq q als g (v = 7)
ilm q ksp pl ky g H2O (v = 5)
ilm liq q als g cd ksp (v = 5)
ilm liq q sill g cd (v = 6)
ilm q als g cd pl H2O (v = 6)
ilm liq q sill g cd pl ksp (v = 5)
ilm liq q sill g cd pl (v = 5)
ilm liq q sill cd (v = 7)
ilm liq q sill cd pl (v = 7)
ilm liq q sill cd pl (v = 6)
ky
sill
12.5
11.5
10.5
9.5
8.5
7.5
6.5
5.5
4.5
3.5
550
600
650
700
750
800
850
900
950
1000
1. ilm liq q ksp ky g H2O ru (v = 4)
2. ilm q ksp pl ky g H2O ru (v = 4)
3. ilm liq q als g cd pl ksp H2O (v = 3)
4. ilm q sill cd pl H2O (v = 7)

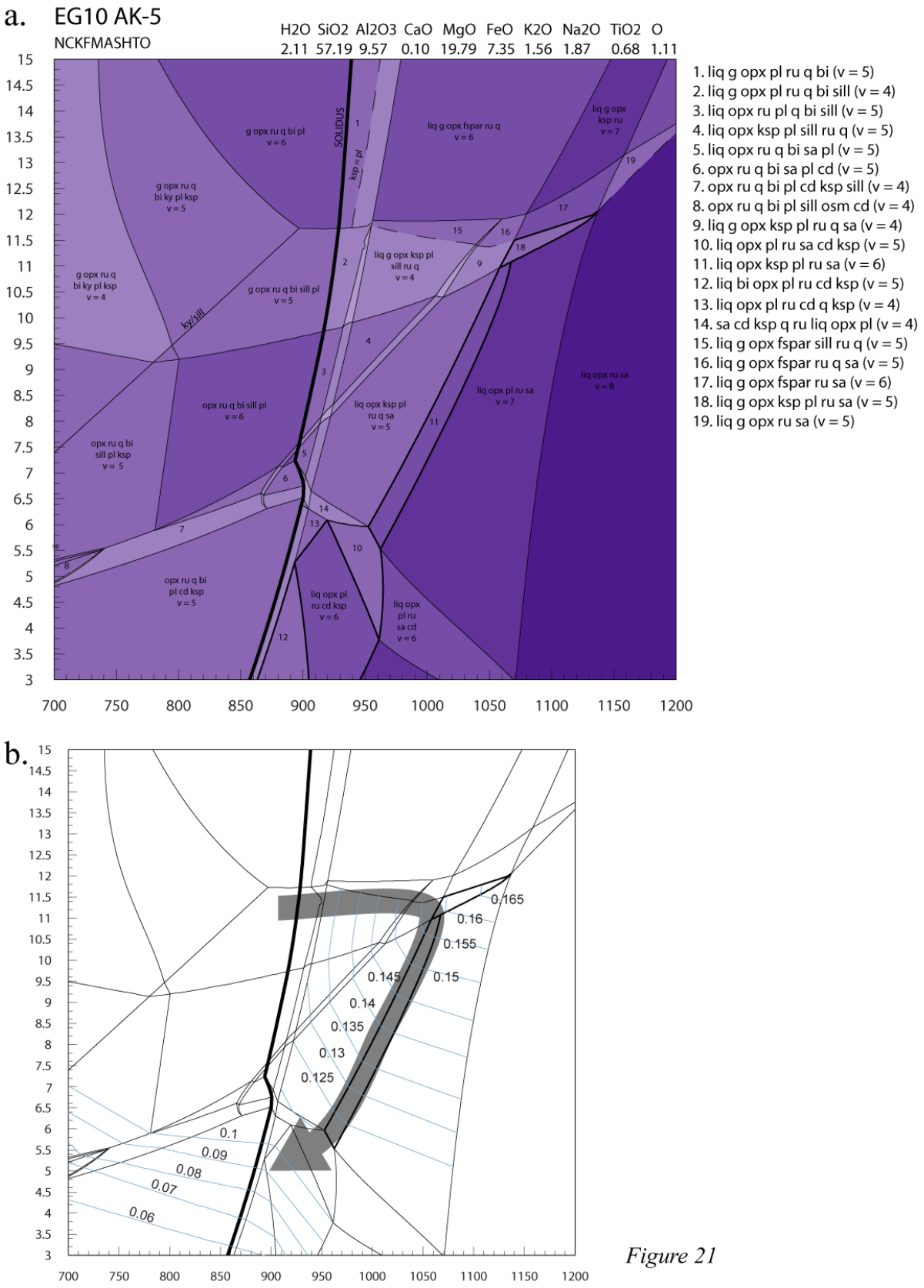

1. liq g opx pl ru q bi (v = 5)
2. liq g opx pl ru q bi sill (v = 4)
3. liq opx ru pl q bi sill (v = 5)
4. liq opx ksp pl sill ru q (v = 5)
5. liq opx ru q bi sa pl (v = 5)
6. opx ru q bi sa pl cd (v = 5)
7. opx ru q bi pl cd ksp sill (v = 4)
8. opx ru q bi pl sill osm cd (v = 4)
9. liq g opx ksp pl ru q sa (v = 4)
10. liq opx pl ru sa cd ksp (v = 5)
11. liq opx ksp pl ru sa (v = 6)
12. liq bi opx pl ru cd ksp (v = 5)
13. liq opx pl ru cd q ksp (v = 4)
14. sa cd ksp q ru liq opx pl (v = 4)
15. liq g opx fspar sill ru q (v = 5)
16. liq g opx fspar ru q sa (v = 5)
17. liq g opx fspar ru sa (v = 6)
18. liq g opx ksp pl ru sa (v = 5)
19. liq g opx ru sa (v = 5)

Figure 21

Figure 22

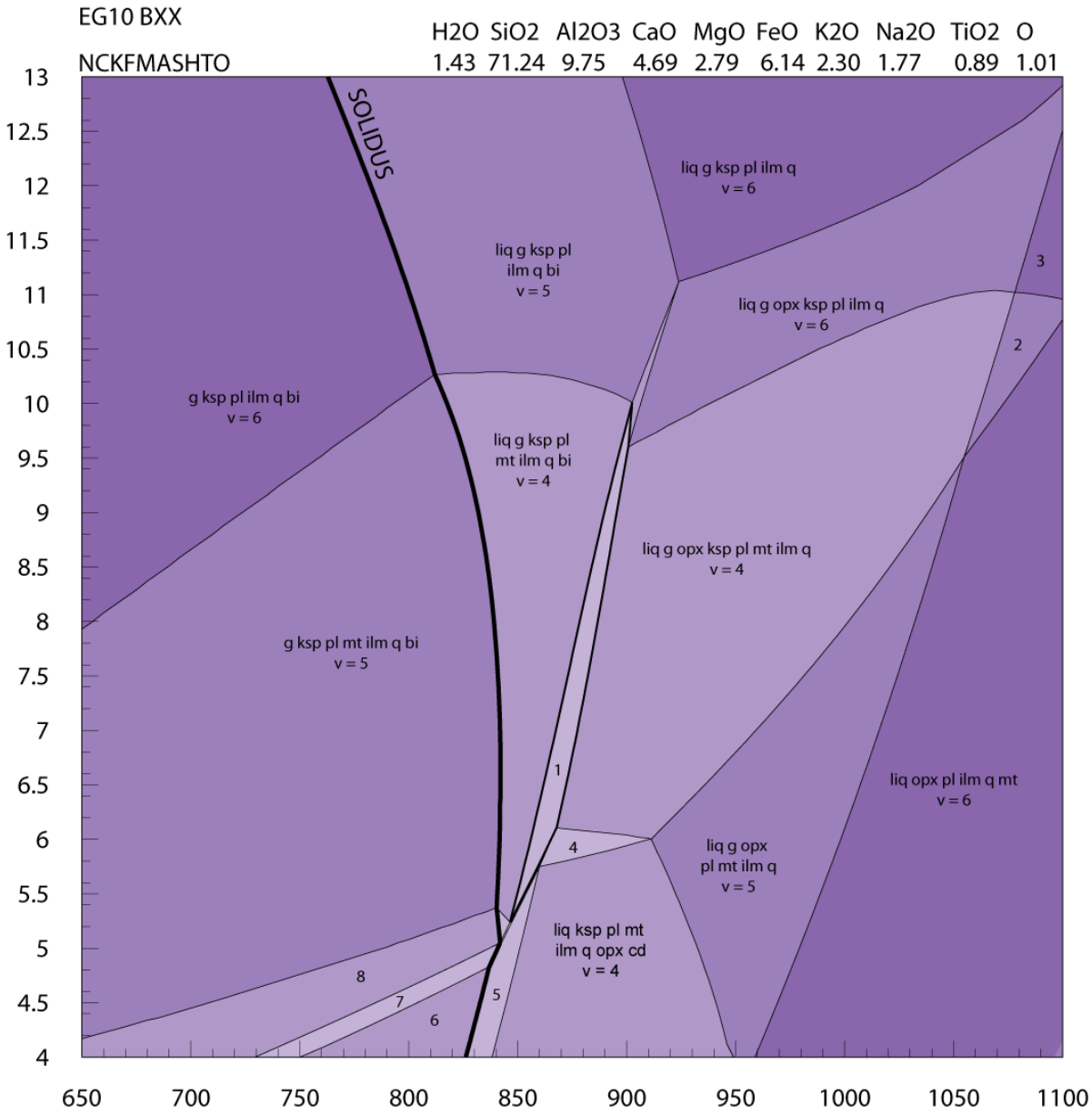

1. liq g ksp pl mt ilm q bi opx (v = 3)
2. liq g opx pl mt ilm q (v = 5)
3. liq g opx pl ilm q (v = 6)
4. liq g ksp pl mt ilm q opx cd (v = 3)
5. liq ksp pl mt ilm q opx cd bi (v = 3)
6. ksp pl mt ilm q opx cd bi (v = 4)
7. g ksp pl mt ilm q opx cd bi (v = 3)
8. g ksp pl mt ilm g bi cd (v = 4)

Figure 23
Sample EG10 BXX

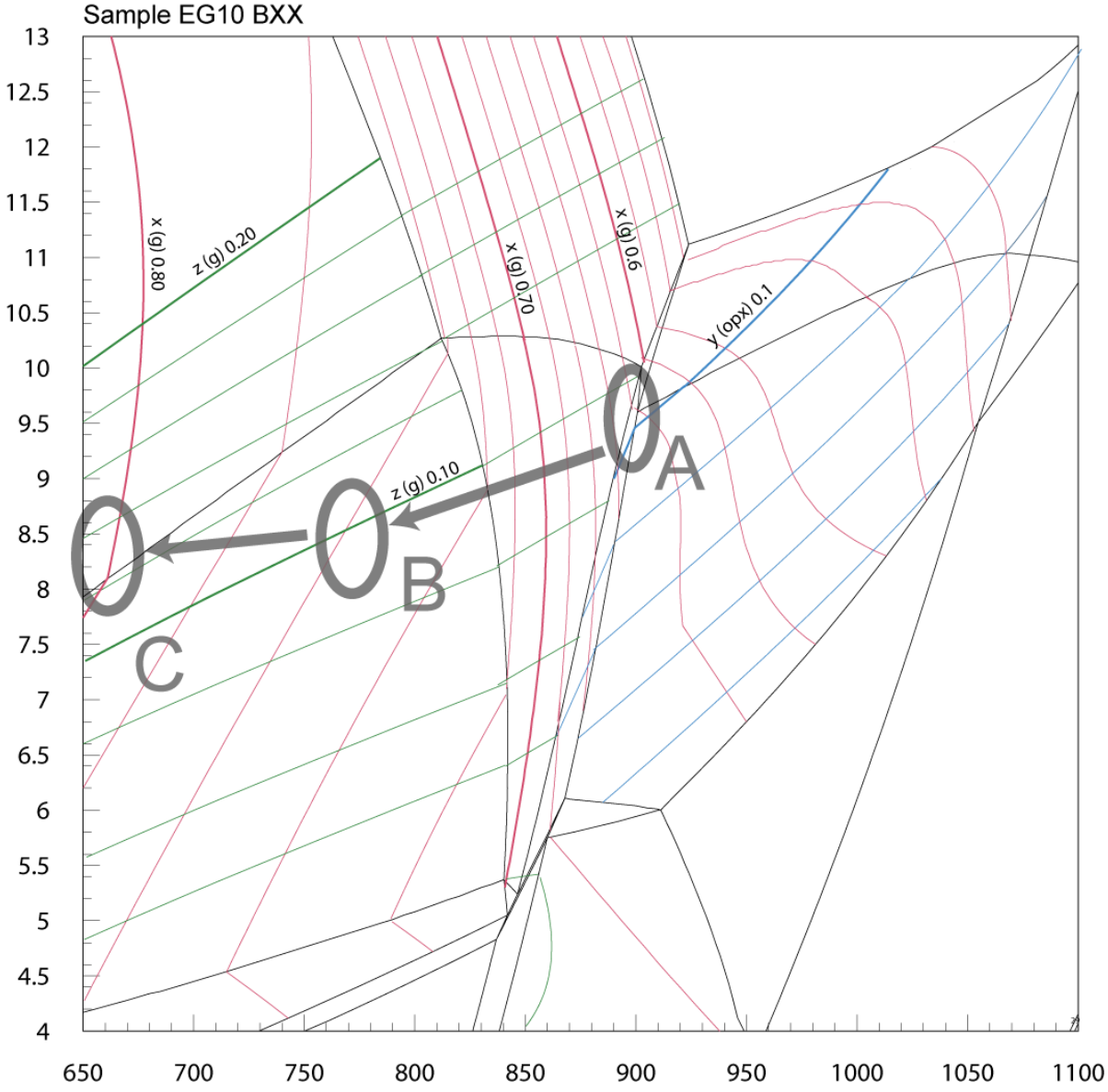

A. Peak mineral assemblage
B. Garnet core composition
C. Garnet rim composition

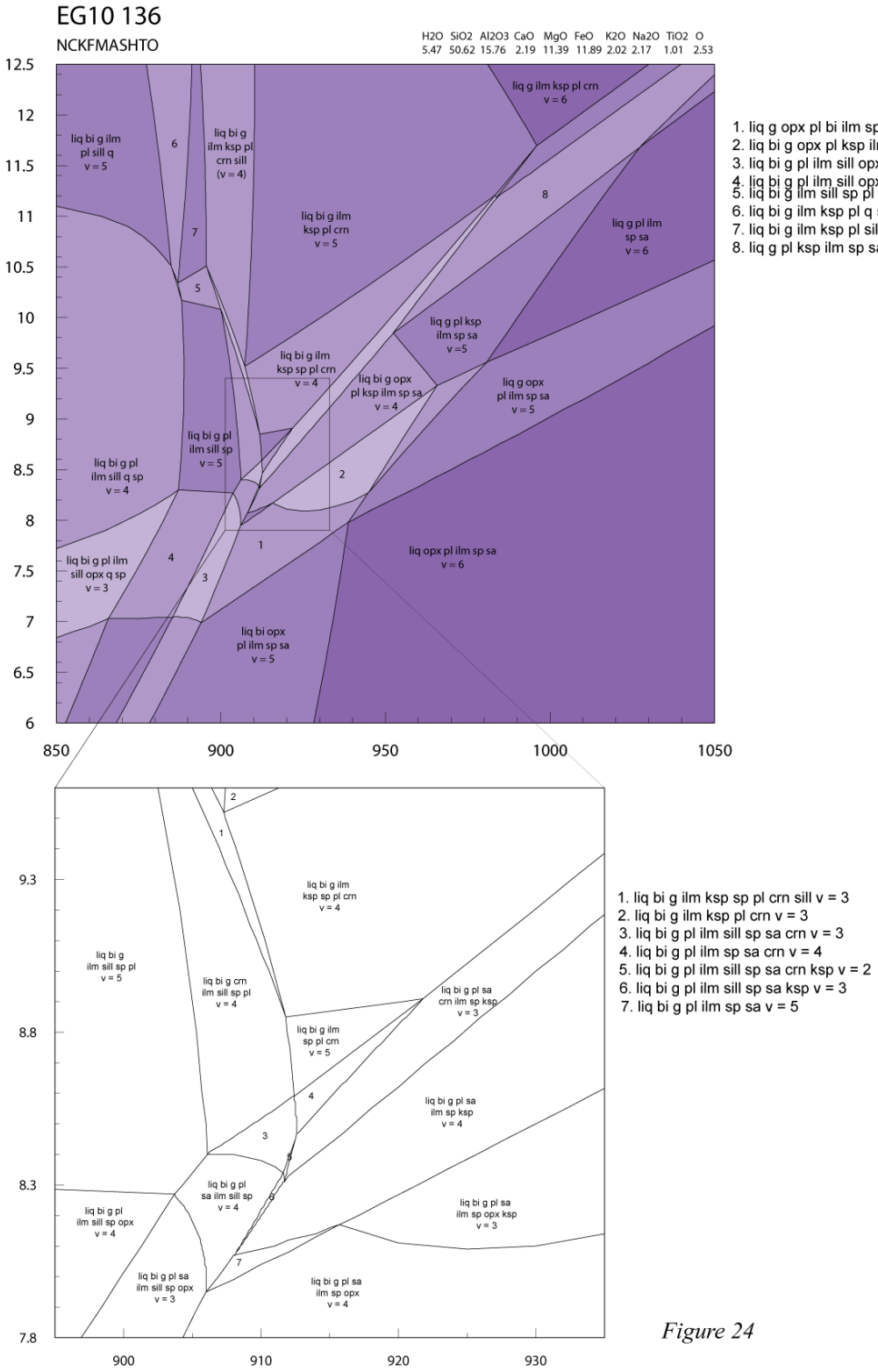
EG10 136
NCKFMASHTO
H2O SiO2 Al2O3 CaO MgO FeO K2O Na2O TiO2 O
5.47 50.62 15.76 2.19 11.39 11.89 2.02 2.17 1.01 2.53
liq g ilm ksp pl crn v = 6
liq bi g ilm pl sill q v = 5
liq bi g ilm ksp pl crn sill (v = 4)
liq bi g ilm ksp pl crn v = 5
liq g pl ilm sp sa v = 6
liq g pl ksp ilm sp sa v =5
liq bi g ilm ksp sp pl crn v = 4
liq bi g opx pl ksp ilm sp sa v = 4
liq g opx pl ilm sp sa v = 5
liq bi g pl ilm sill sp v = 5
liq bi g pl ilm sill q sp v = 4
liq bi g pl ilm sill opx q sp v = 3
liq opx pl ilm sp sa v = 6
liq bi opx pl ilm sp sa v = 5
1. liq g opx pl bi ilm sp sa (v = 4)
2. liq bi g opx pl ksp ilm sp sa (v = 3)
3. liq bi g pl ilm sill opx sa sa (v = 3)
4. liq bi g pl ilm sill opx sp (v = 4)
5. liq bi g ilm sill sp pl ksp (v = 4)
6. liq bi g ilm ksp pl q sill (v = 4)
7. liq bi g ilm ksp pl sill (v = 5)
8. liq g pl ksp ilm sp sa crn (v = 4)
liq bi g ilm ksp sp pl crn v = 4
liq bi g ilm ksp pl crn v = 3
liq bi g pl ilm sill sp sa crn v = 3
liq bi g pl ilm sp sa crn v = 4
liq bi g pl ilm sill sp sa crn ksp v = 2
liq bi g pl ilm sill sp sa ksp v = 3
liq bi g pl ilm sp sa v = 5
liq bi g ilm sill sp pl v = 5
liq bi g crn ilm sill sp pl v = 4
liq bi g pl sa crn ilm sp ksp v = 3
liq bi g ilm sp pl crn v = 5
liq bi g pl sa ilm sp ksp v = 4
liq bi g pl sa ilm sill sp v = 4
liq bi g pl ilm sill sp opx v = 4
liq bi g pl sa ilm sp opx ksp v = 3
liq bi g pl sa ilm sill sp opx v = 3
liq bi g pl sa ilm sp opx v = 4

Figure 24

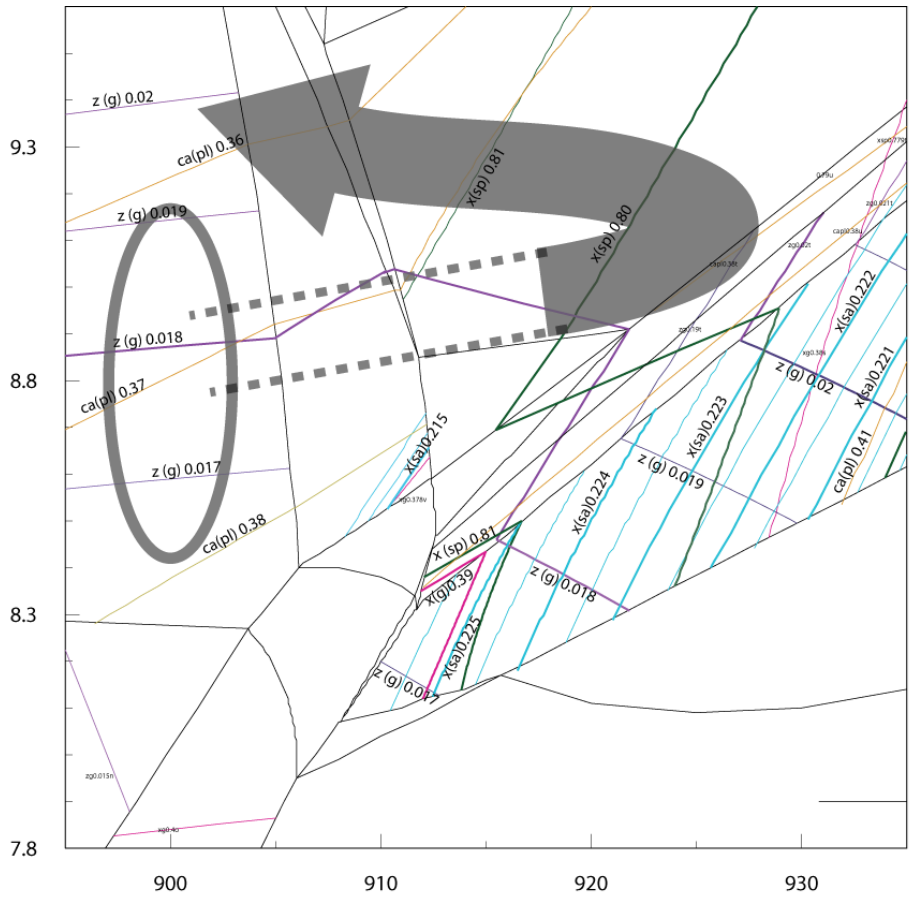
z (g) 0.02
ca(pl) 0.36
z (g) 0.019
z (g) 0.018
ca(pl) 0.37
z (g) 0.017
ca(pl) 0.38
x(sp) 0.81
x(sp) 0.80
x(sa)0.215
x (sp) 0.81
x(g)0.39
x(sa)0.225
z (g) 0.018
x(sa)0.224
x(sa)0.223
z (g) 0.019
z (g) 0.02
x(sa)0.222
x(sa)0.221
ca(pl) 0.41
9.3
8.8
8.3
7.8
900
910
920
930

a.

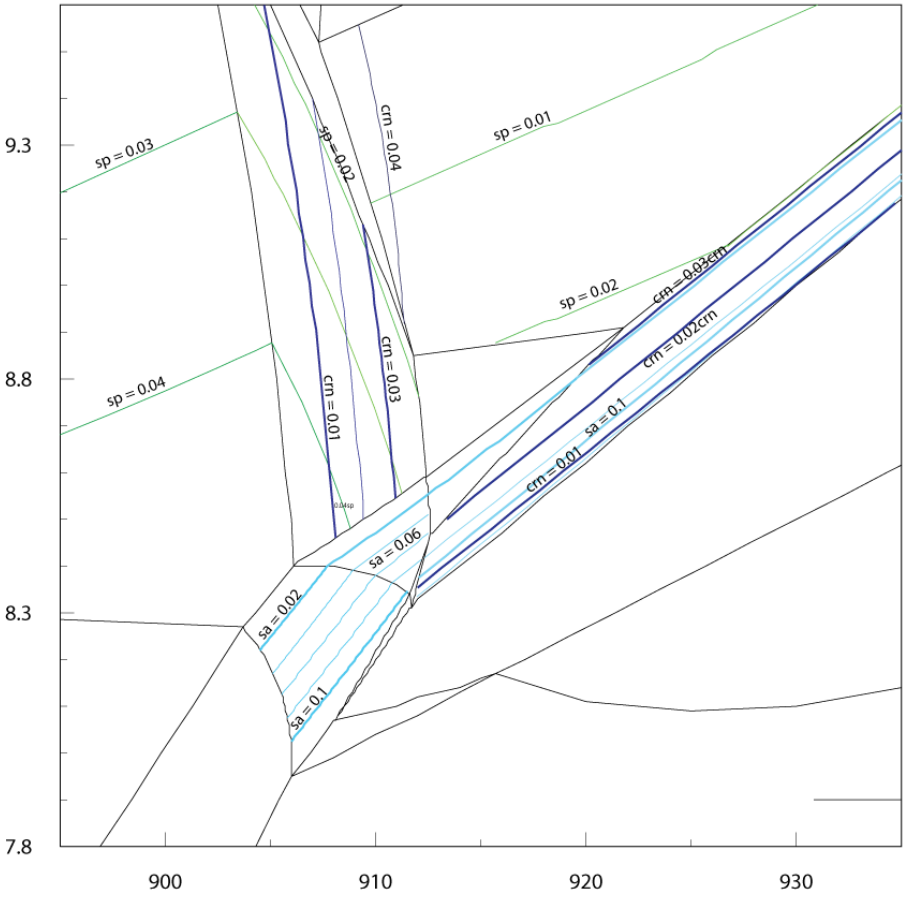
sp = 0.03
sp = 0.02
crn = 0.04
sp = 0.01
sp = 0.02
crn = 0.03crn
crn = 0.02crn
sp = 0.04
crn = 0.01
crn = 0.03
sa = 0.1
crn = 0.01
sa = 0.06
sa = 0.02
sa = 0.1
9.3
8.8
8.3
7.8
900
910
920
930

b. *Figure 25*

Figure 26 Sample EG10-063

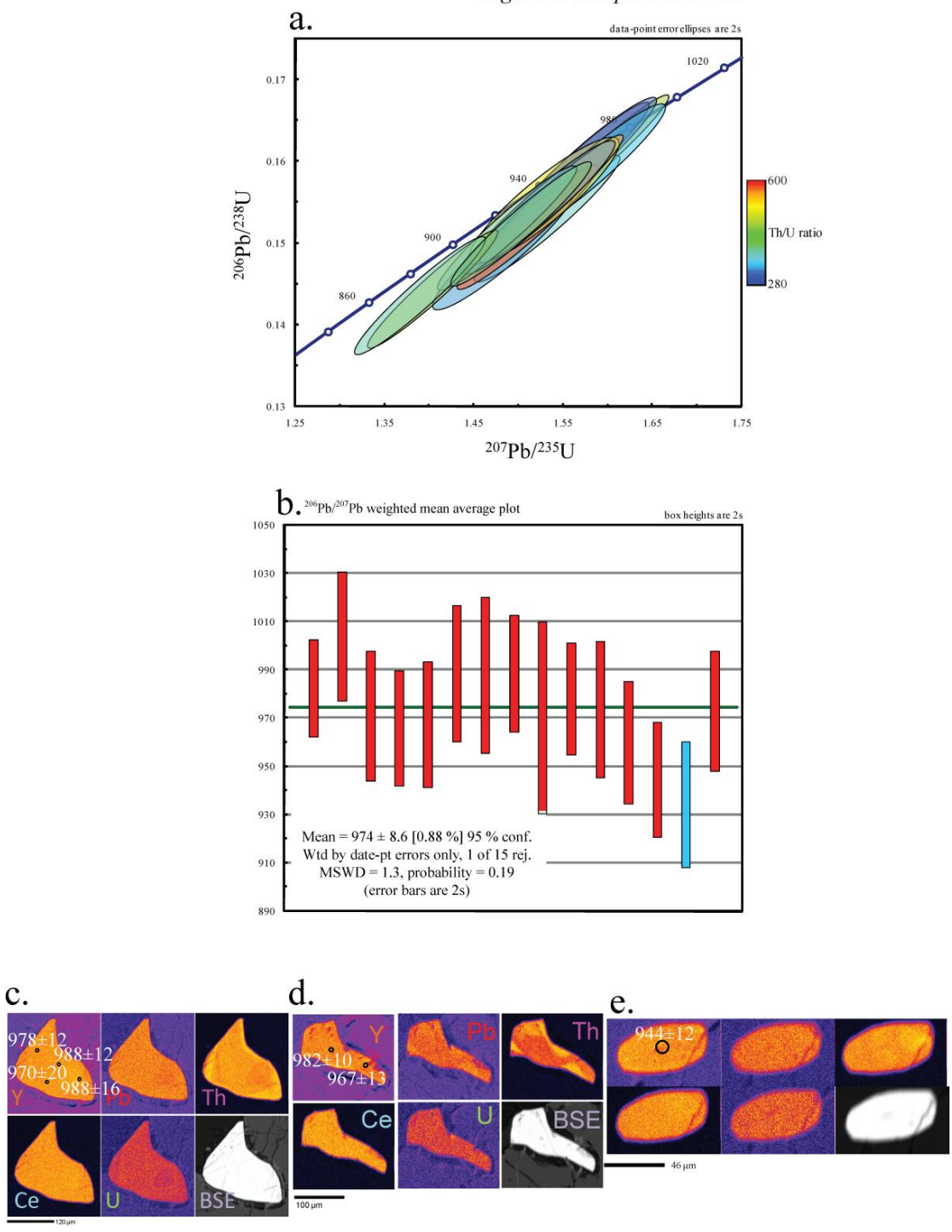

Figure 27 Sample EG10-AK3

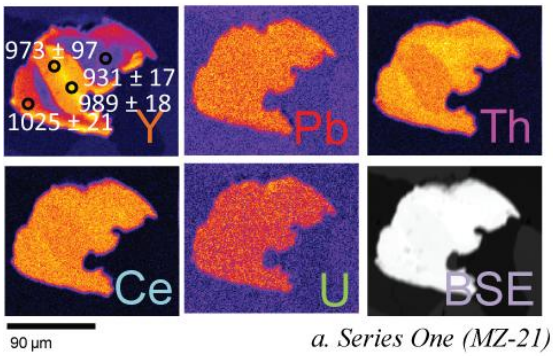

a. Series One (MZ-21)

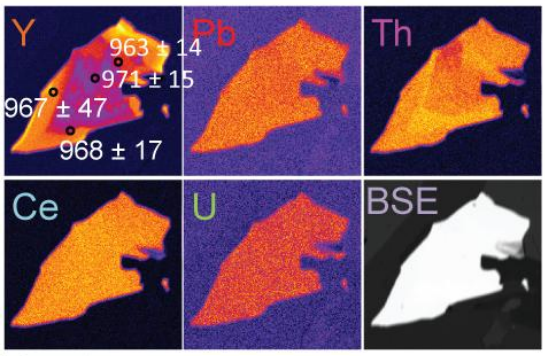

b. Series Two (MZ-5)

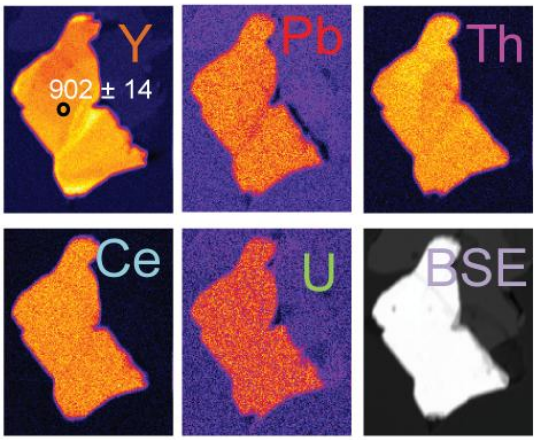

c. Series Three (MZ-6)

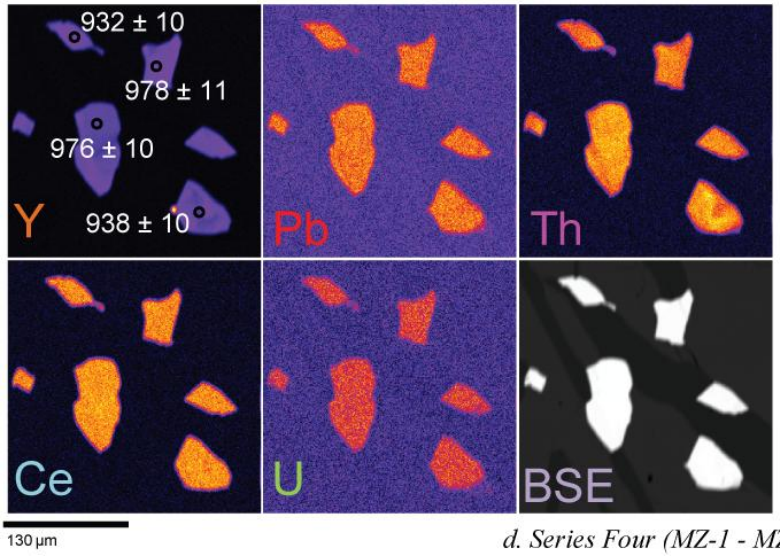

d. Series Four (MZ-1 - MZ-4)

e.

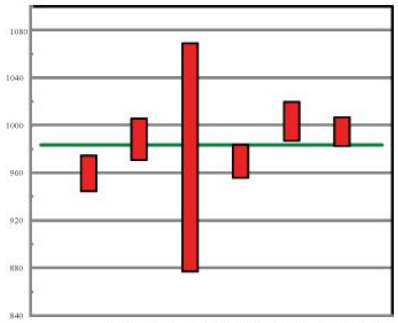

Mean = 975.9±5.7 [0.58%] 95% conf.Wtd by data-pt errs only, 1 of 8 rej.MSWD = 1.01, probability = 0.42

f.

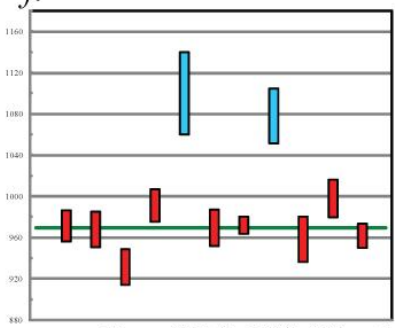

Mean = 969±12 [1.3%] 95% conf. Wtd by data-pt errs only, 2 of 11 rej. MSWD = 5.0, probability = 0.000

g.

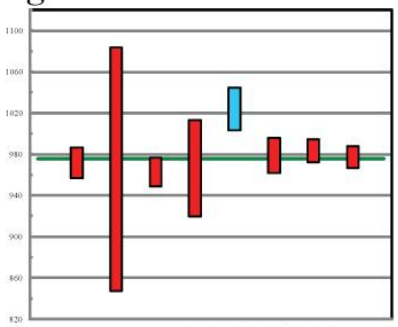

Mean = 983±18 [1.9%] 95% conf. Wtd by data-pt errs only, 0 of 6 rej. MSWD = 4.7, probability = 0.000

Figure 28 Sample EG10-AK3

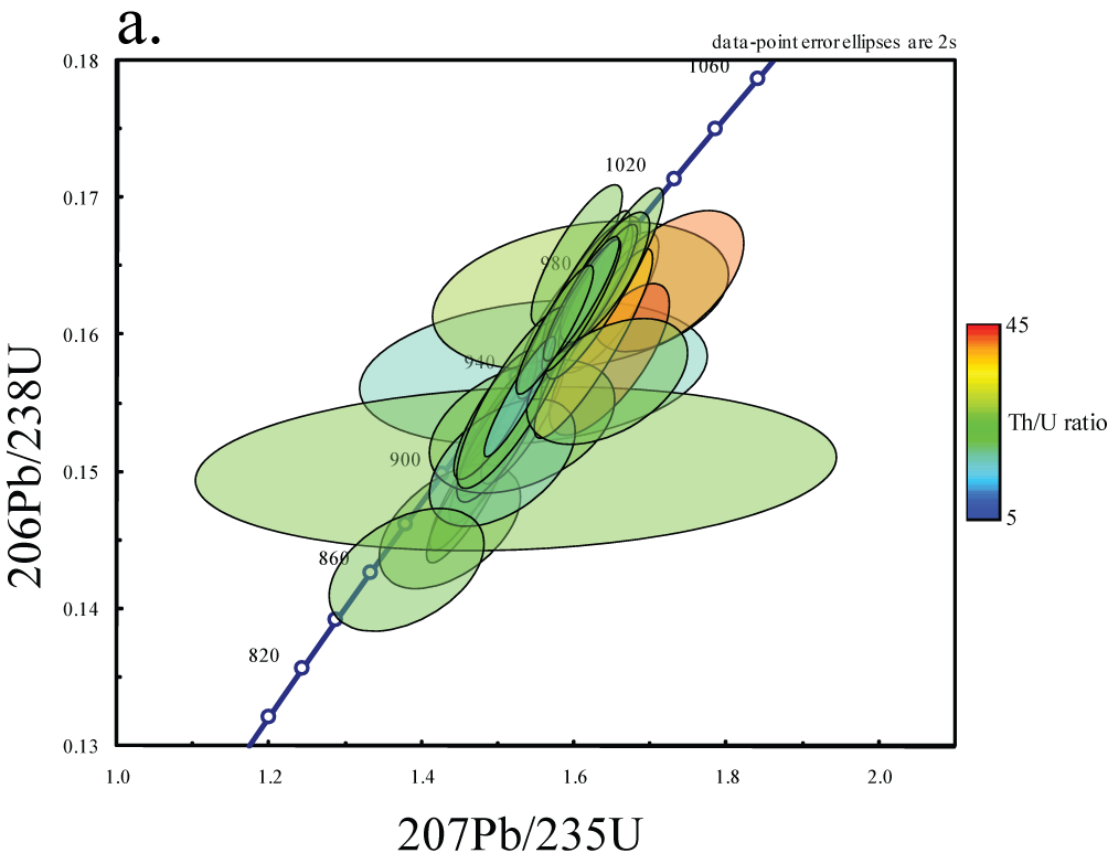

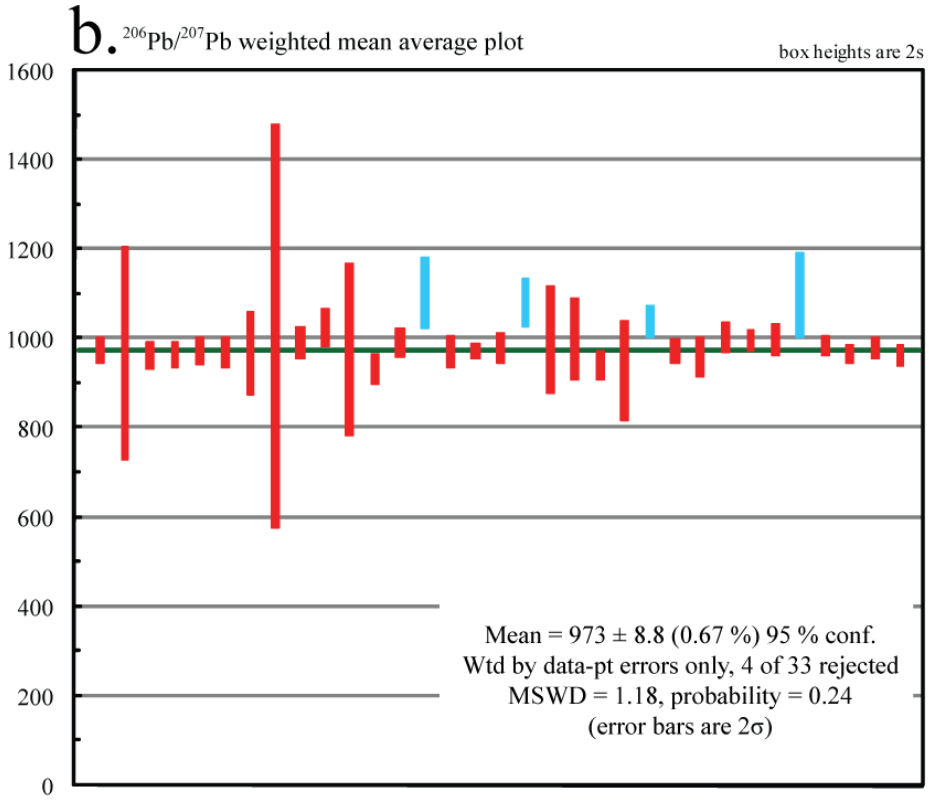

Figure 29 Sample EG10-AK5

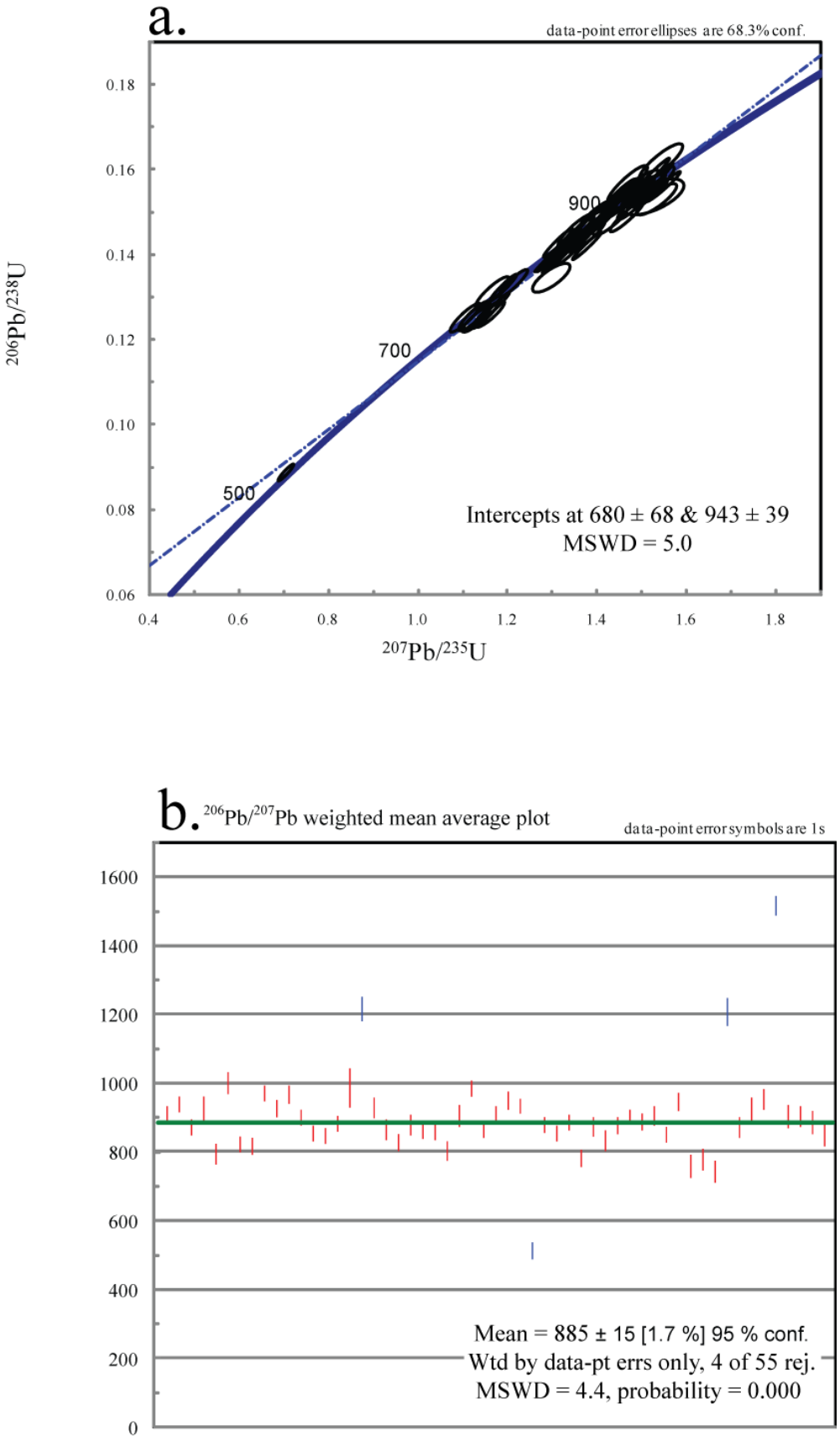

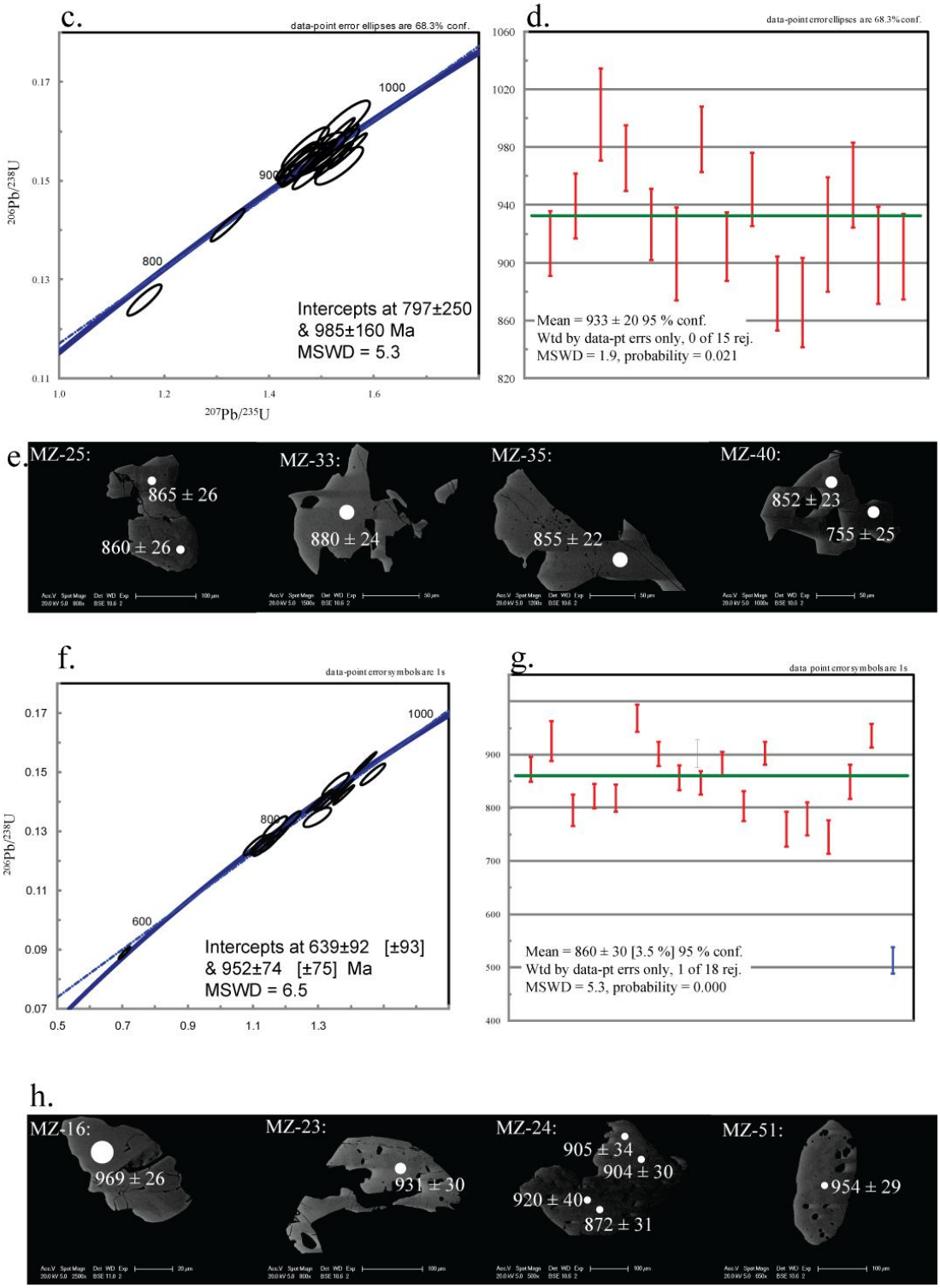
c.
data-point error ellipses are 68.3% conf.
1000
900
800
Intercepts at 797±250
& 985±160 Ma
MSWD = 5.3
$^{206}Pb/^{238}U$
$^{207}Pb/^{235}U$
d.
data-point error ellipses are 68.3% conf.
Mean = 933 ± 20 95 % conf.
Wtd by data-pt errs only, 0 of 15 rej.
MSWD = 1.9, probability = 0.021
e.
MZ-25:
865 ± 26
860 ± 26
MZ-33:
880 ± 24
MZ-35:
855 ± 22
MZ-40:
852 ± 23
755 ± 25
f.
data-point error symbols are 1s
1000
800
600
Intercepts at 639±92 [±93]
& 952±74 [±75] Ma
MSWD = 6.5
$^{206}Pb/^{238}U$
g.
data-point error symbols are 1s
Mean = 860 ± 30 [3.5 %] 95 % conf.
Wtd by data-pt errs only, 1 of 18 rej.
MSWD = 5.3, probability = 0.000
h.
MZ-16:
969 ± 26
MZ-23:
931 ± 30
MZ-24:
905 ± 34
904 ± 30
920 ± 40
872 ± 31
MZ-51:
954 ± 29

h.

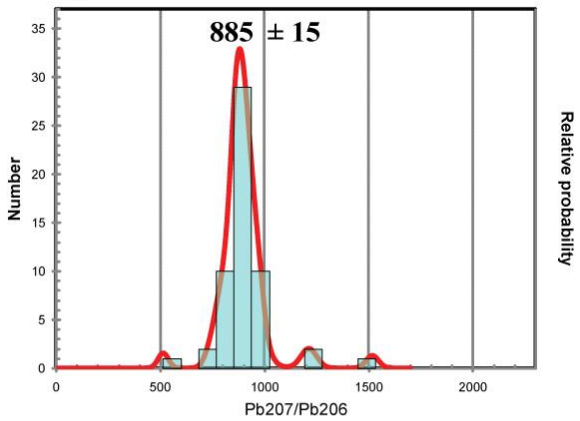
885 ± 15
Number
Relative probability
Pb207/Pb206
0
5
10
15
20
25
30
35
0
500
1000
1500
2000

i.

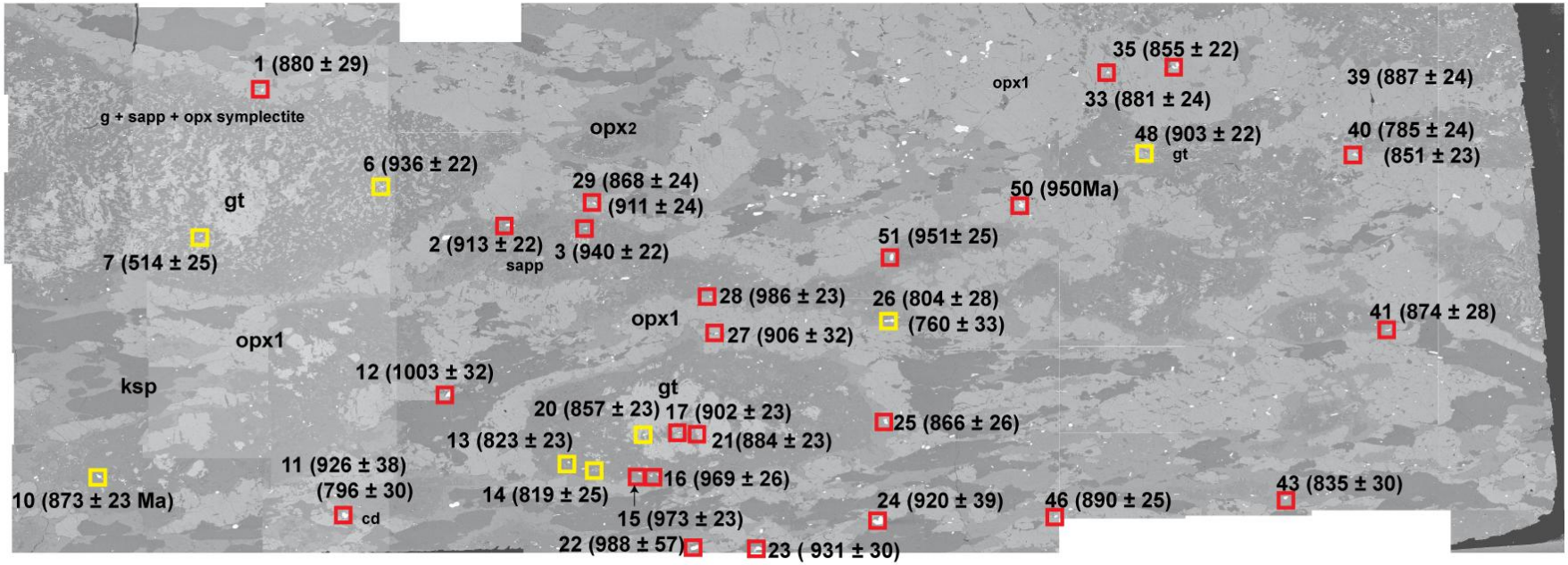
1 (880 ± 29)
g + sapp + opx symplectite
opx2
6 (936 ± 22)
gt
29 (868 ± 24)
(911 ± 24)
7 (514 ± 25)
2 (913 ± 22)
sapp
3 (940 ± 22)
opx1
35 (855 ± 22)
33 (881 ± 24)
39 (887 ± 24)
48 (903 ± 22)
gt
40 (785 ± 24)
(851 ± 23)
50 (950Ma)
51 (951± 25)
28 (986 ± 23)
opx1
26 (804 ± 28)
(760 ± 33)
27 (906 ± 32)
41 (874 ± 28)
opx1
ksp
12 (1003 ± 32)
gt
20 (857 ± 23)
17 (902 ± 23)
21(884 ± 23)
13 (823 ± 23)
25 (866 ± 26)
11 (926 ± 38)
(796 ± 30)
cd
10 (873 ± 23 Ma)
14 (819 ± 25)
16 (969 ± 26)
15 (973 ± 23)
22 (988 ± 57)
23 (931 ± 30)
24 (920 ± 39)
46 (890 ± 25)
43 (835 ± 30)

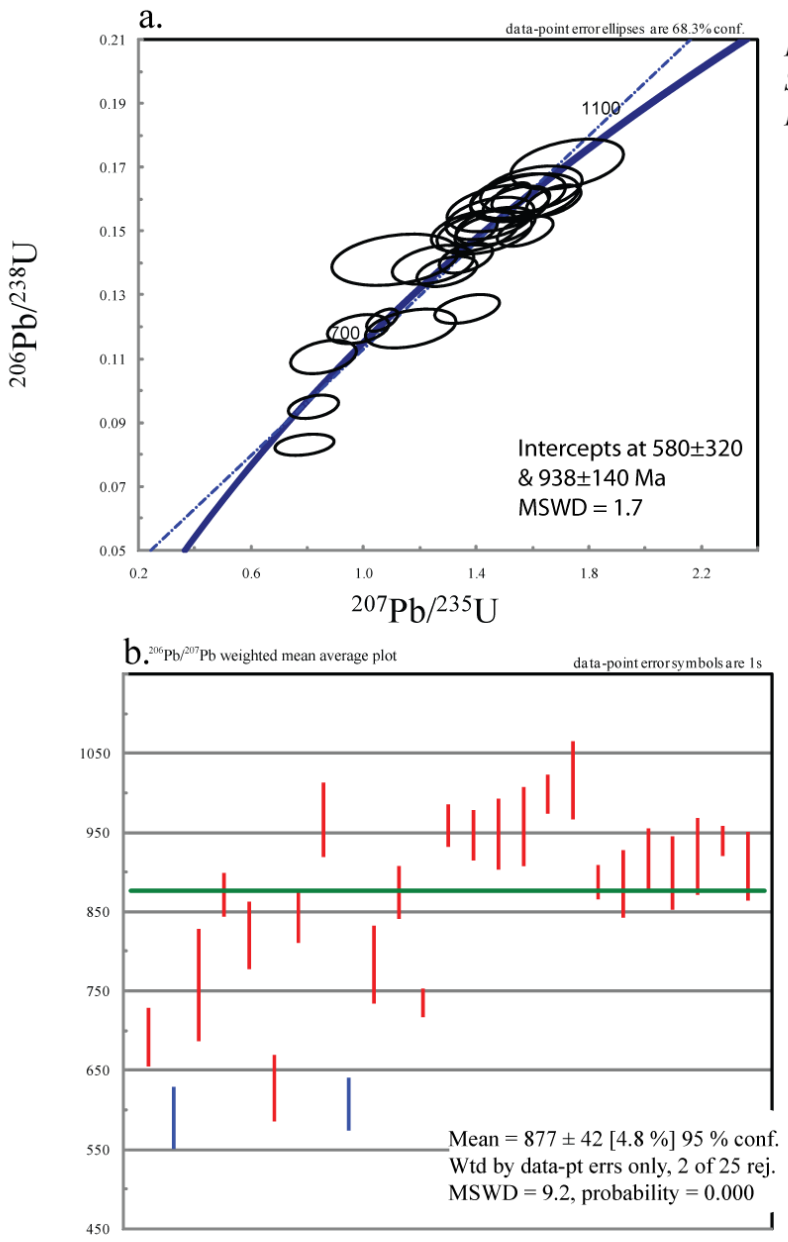

Figure 30 Sample EG10-BXX

g.Sample EG10-BXX: monazite analysis within garnet grains

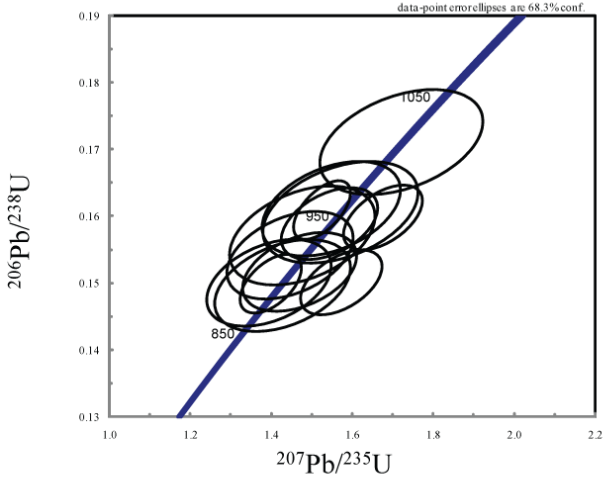

h.Sample EG10-BXX: monazite analysis within garnet grains

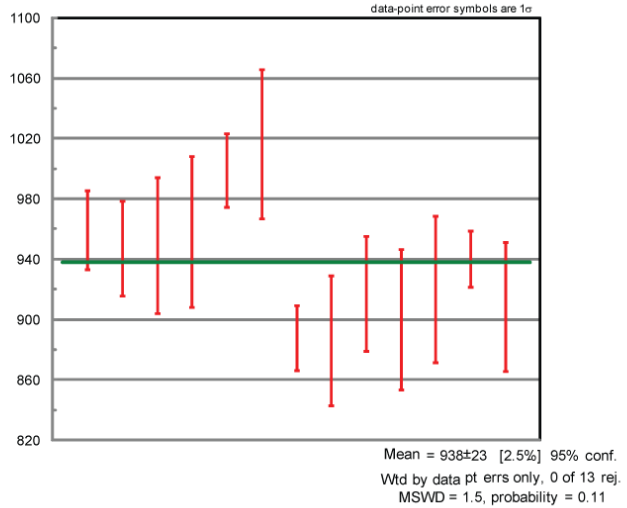

i.Sample EG10-BXX: monazite analysis within the matrix

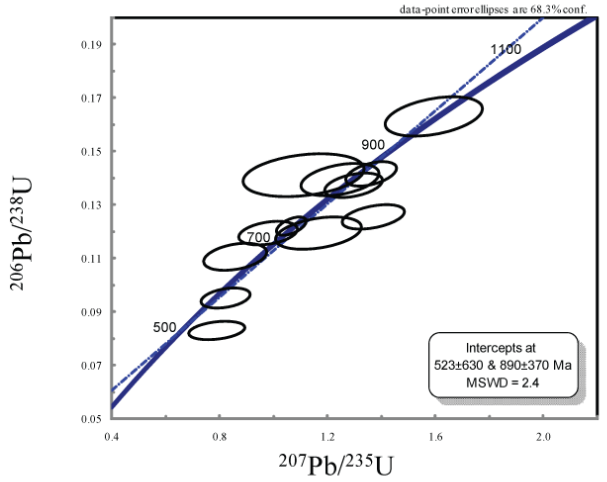

j.Sample EG10-BXX: monazite analysis within the matrix

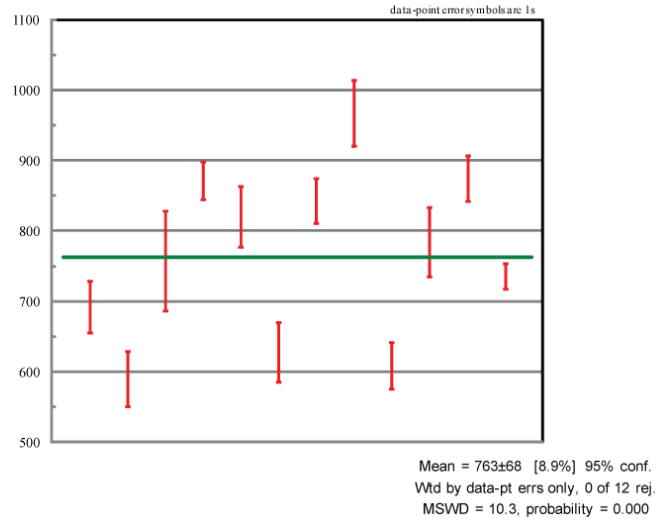

Figure 31 Sample EG10-087

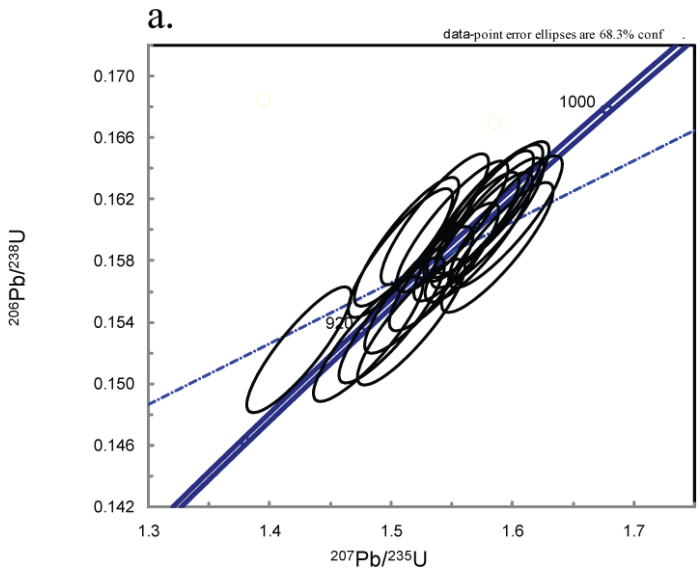

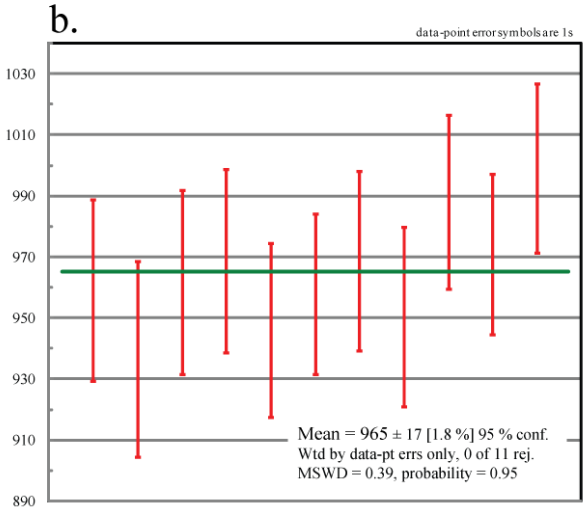

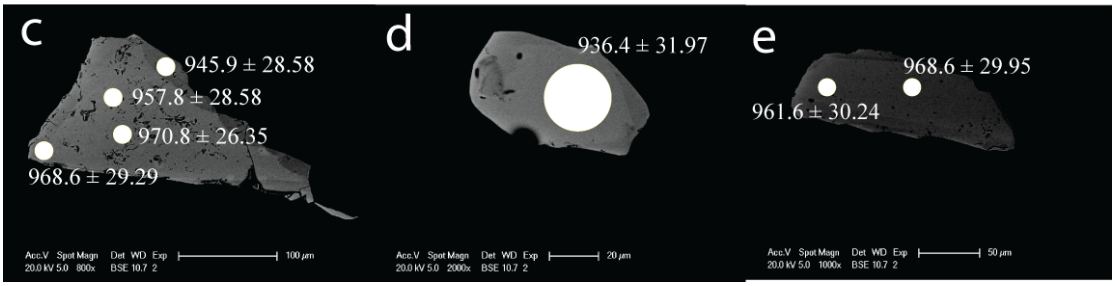

Sample EG10-118

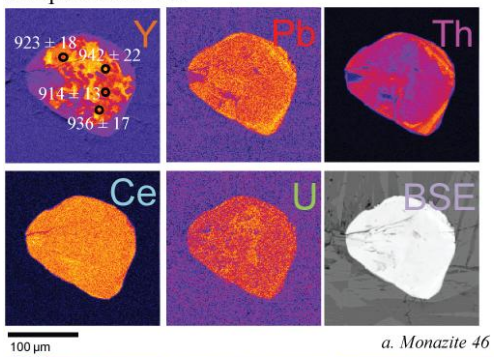

a. Monazite 46

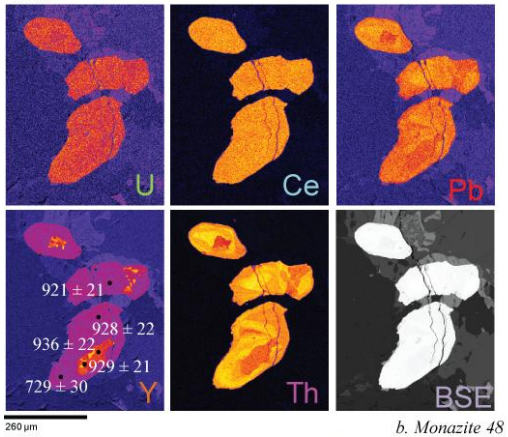

b. Monazite 48

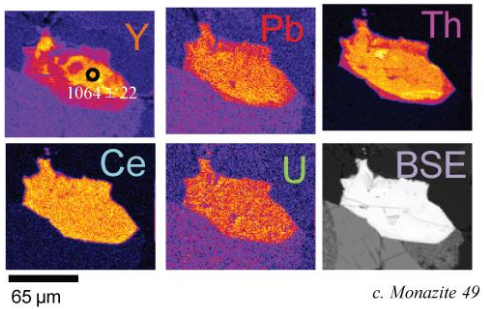

c. Monazite 49

Sample EG10-136

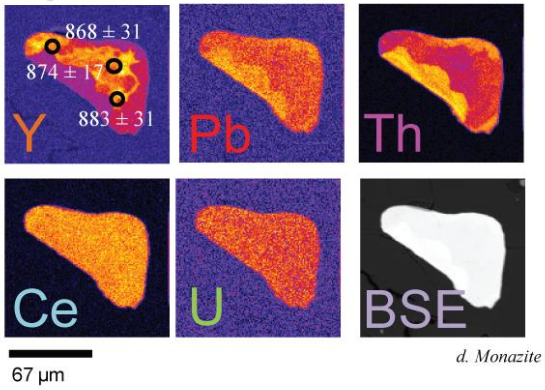

d. Monazite 54

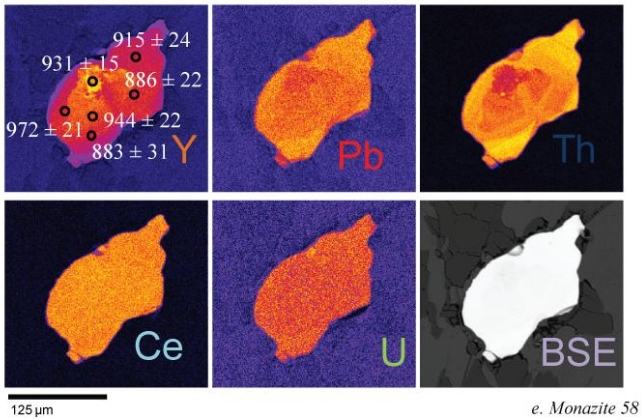

e. Monazite 58

Figure 32

Figure 33
Sample EG10-118

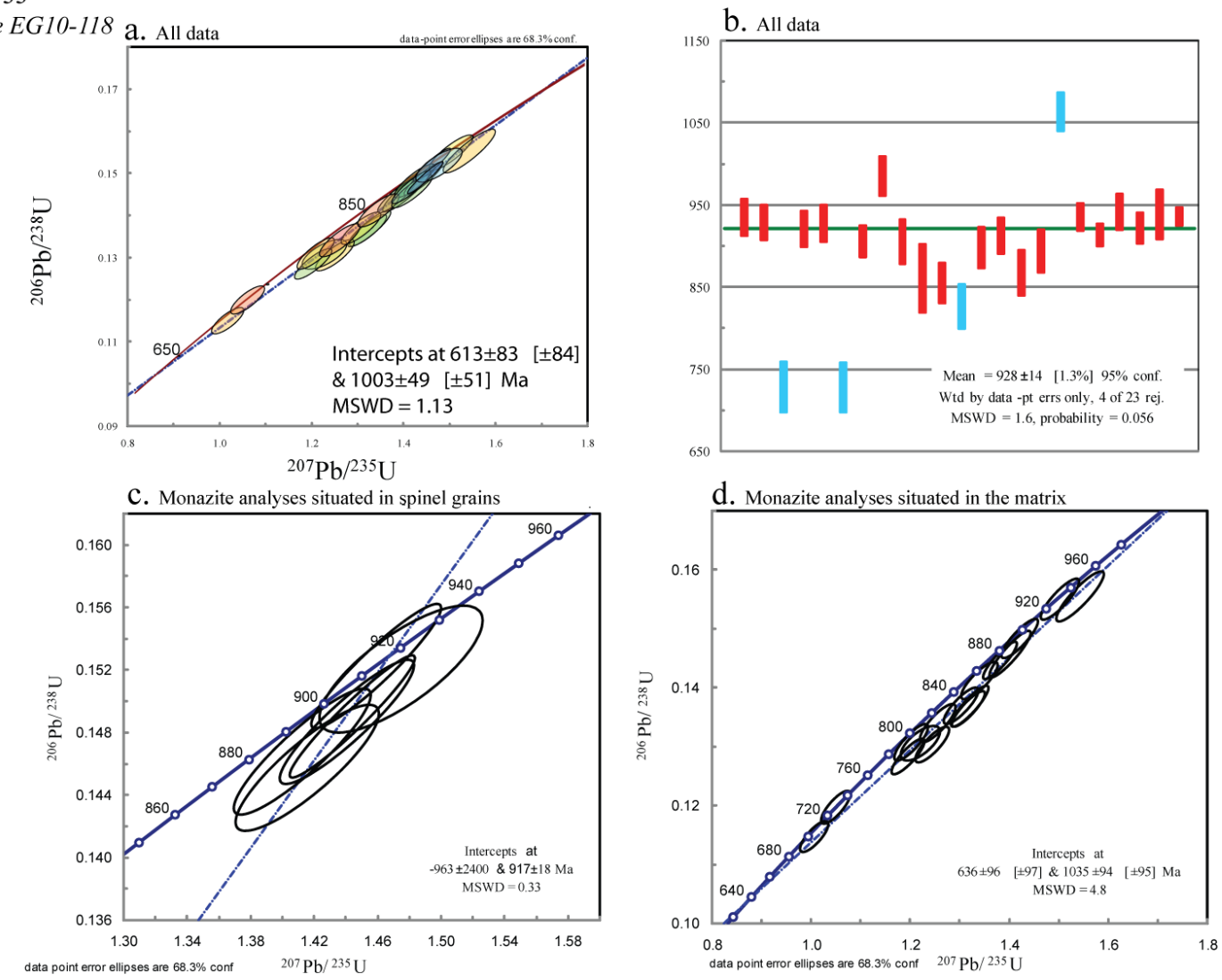

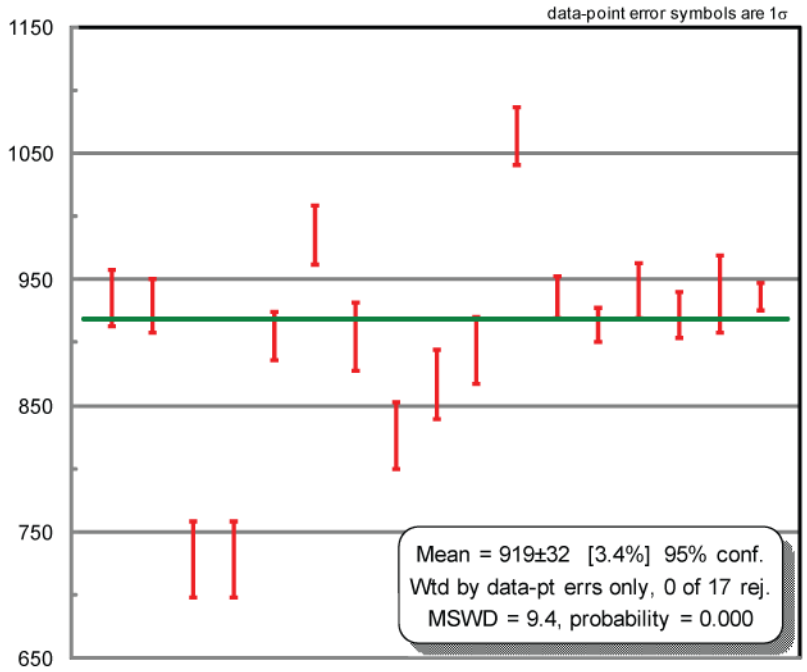

(e) Rim analyses of monazite grains

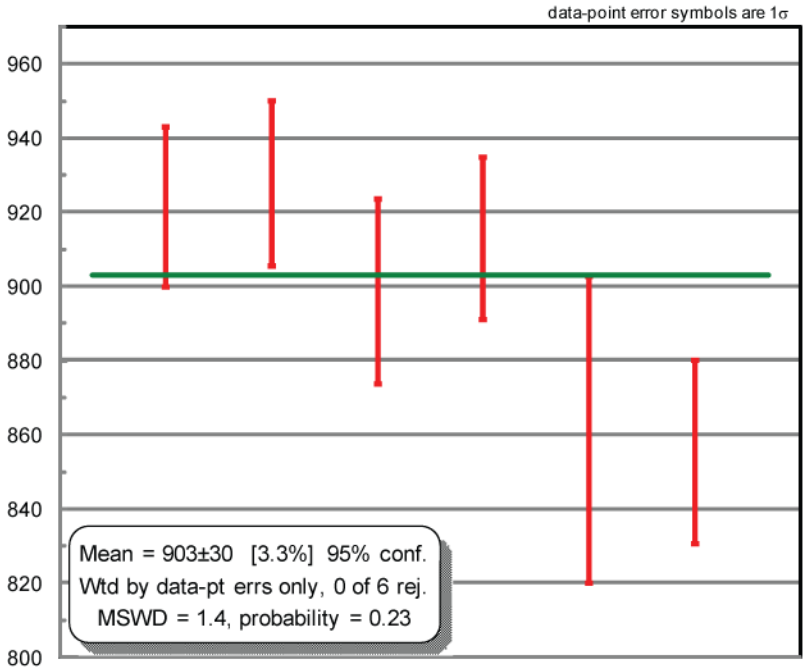

(f) Core analyses of monazite grains

Figure 34 Sample EG10-136

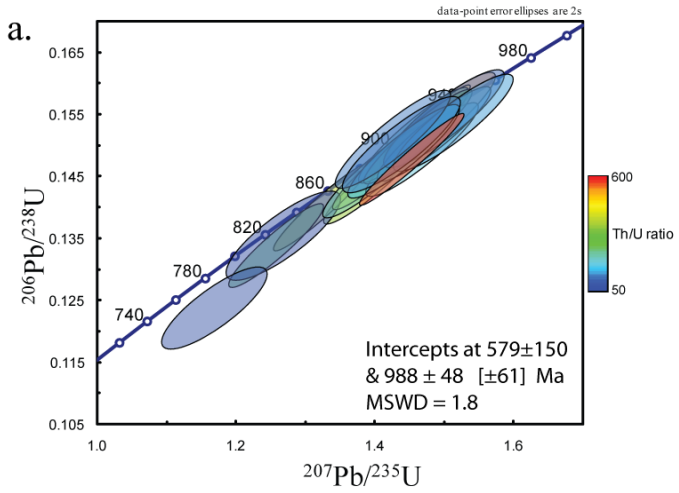

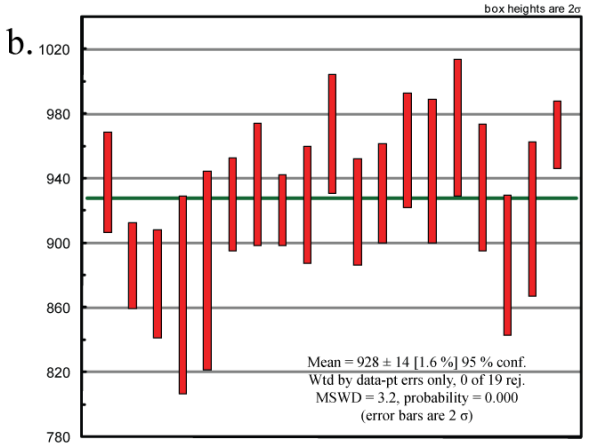

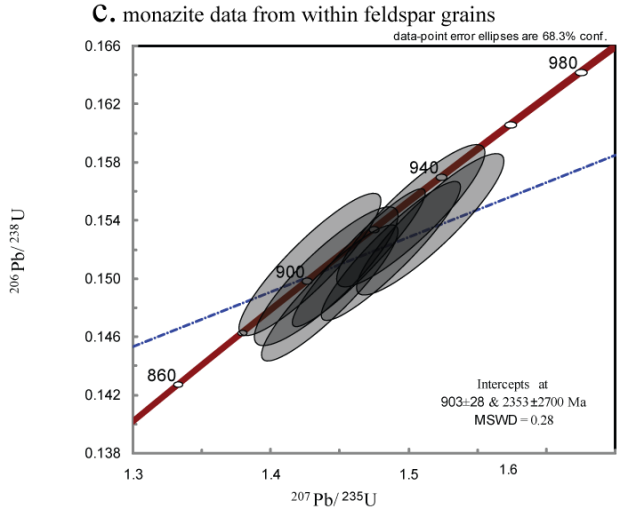

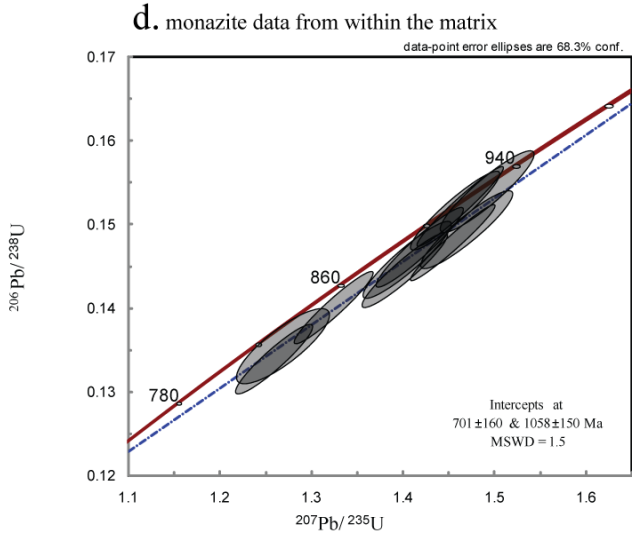

Figure 35

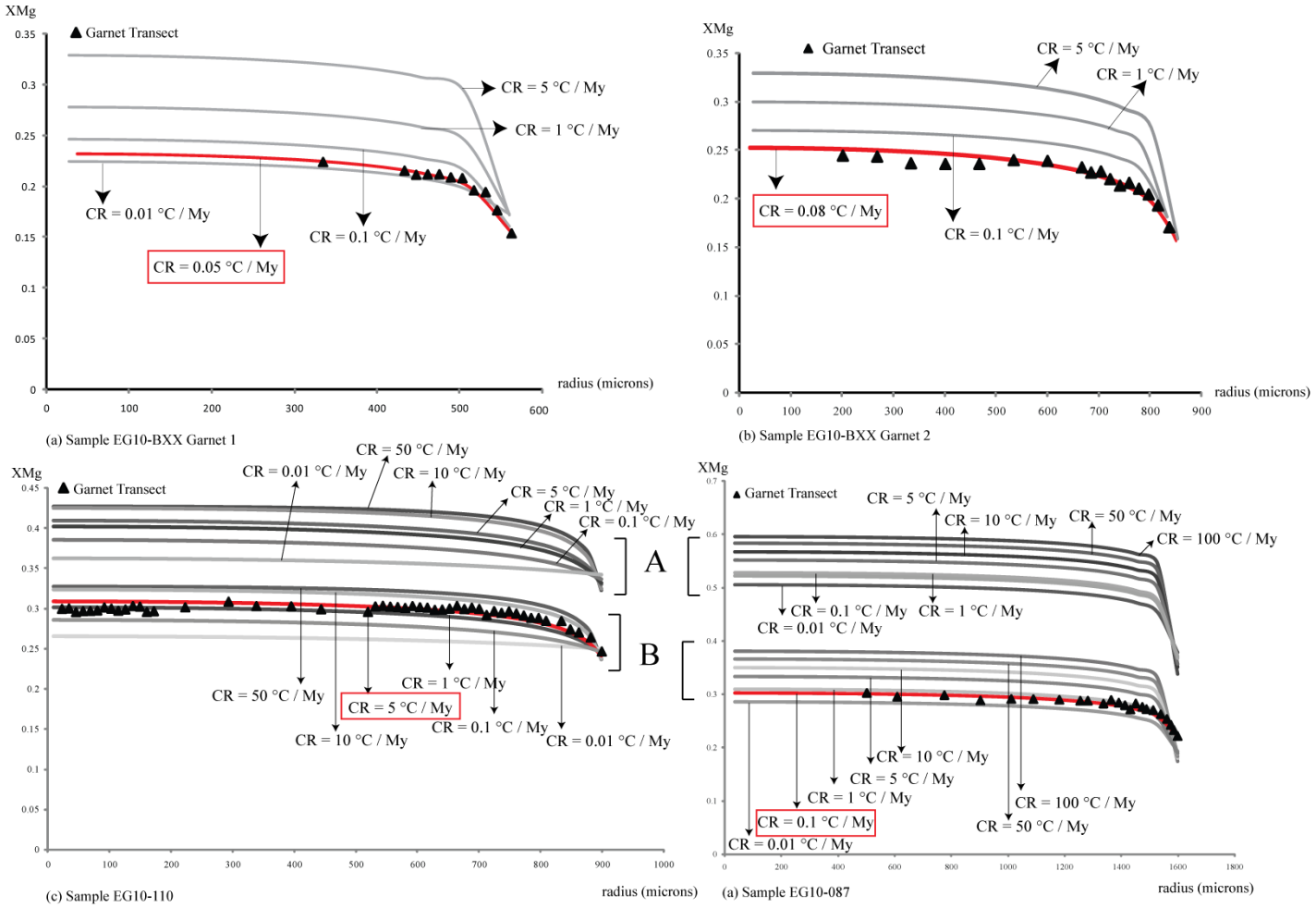
XMg
Garnet Transect
CR = 5 °C / My
CR = 1 °C / My
CR = 0.01 °C / My
CR = 0.05 °C / My
CR = 0.1 °C / My
radius (microns)
(a) Sample EG10-BXX Garnet 1
XMg
Garnet Transect
CR = 5 °C / My
CR = 1 °C / My
CR = 0.08 °C / My
CR = 0.1 °C / My
radius (microns)
(b) Sample EG10-BXX Garnet 2
XMg
Garnet Transect
CR = 50 °C / My
CR = 0.01 °C / My
CR = 10 °C / My
CR = 5 °C / My
CR = 1 °C / My
CR = 0.1 °C / My
A
B
CR = 50 °C / My
CR = 5 °C / My
CR = 1 °C / My
CR = 10 °C / My
CR = 0.1 °C / My
CR = 0.01 °C / My
radius (microns)
(c) Sample EG10-110
XMg
Garnet Transect
CR = 5 °C / My
CR = 10 °C / My
CR = 50 °C / My
CR = 100 °C / My
CR = 0.1 °C / My
CR = 1 °C / My
CR = 0.01 °C / My
CR = 10 °C / My
CR = 5 °C / My
CR = 1 °C / My
CR = 100 °C / My
CR = 0.1 °C / My
CR = 50 °C / My
CR = 0.01 °C / My
radius (microns)
(a) Sample EG10-087

Figure 36

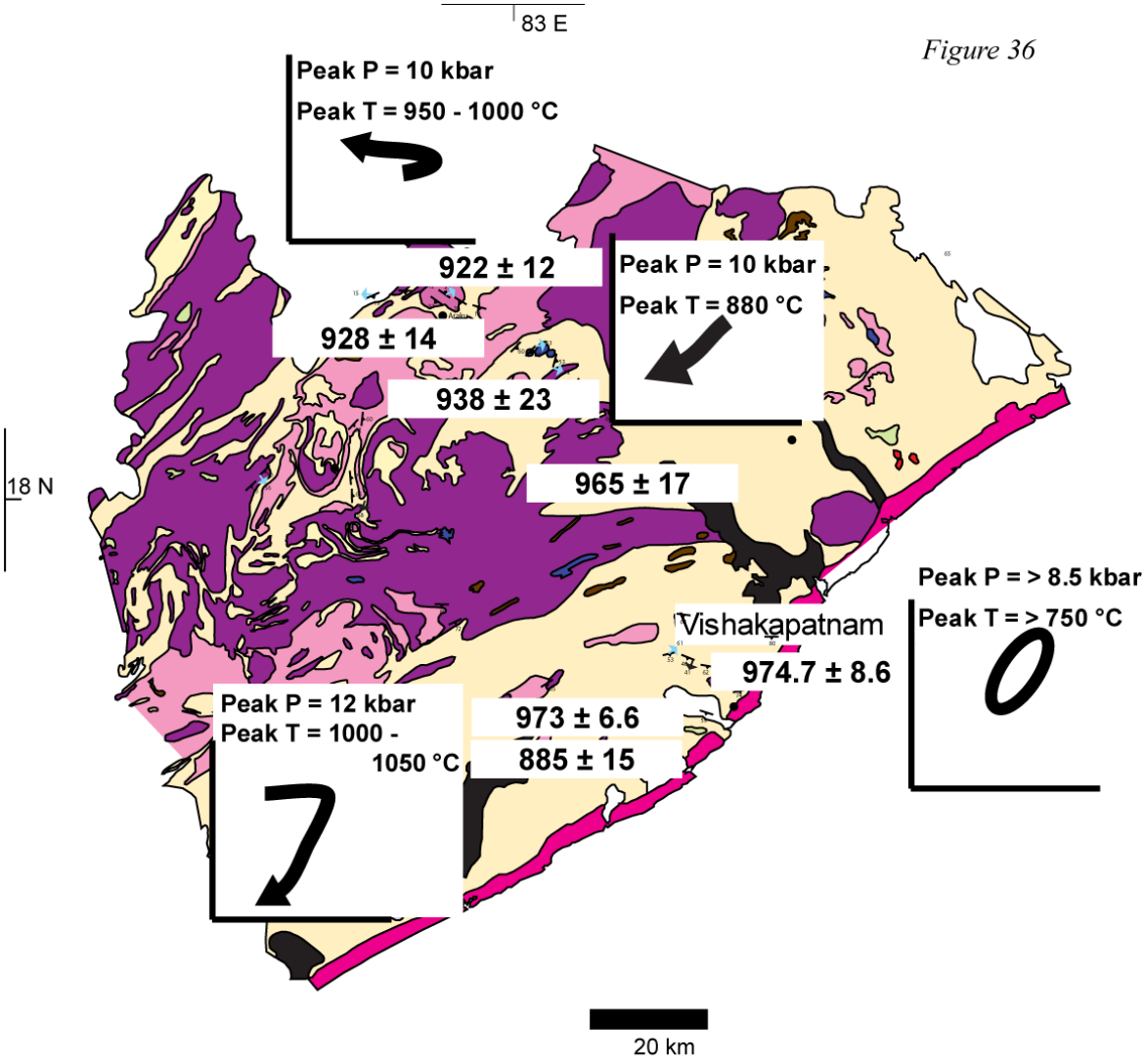

Figure 37